

Raman spectroscopy of β -carotene and CdSe-based nanocrystals

vorgelegt von
Diplom-Physiker
Norman Tschirner
aus Schleswig

Von der Fakultät II - Mathematik und Naturwissenschaften
der Technischen Universität Berlin
zur Erlangung des akademischen Grades
Doktor der Naturwissenschaften
Dr.rer.nat.

genehmigte Dissertation

Promotionsausschuss:
Vorsitzender: Prof. Dr. Michael Lehmann
Berichter: Prof. Dr. Christian Thomsen
Berichter: Prof. Dr. Alf Mews

Tag der wissenschaftlichen Aussprache: 27.10.2011

Berlin 2012

D 83

Raman spectroscopy of β -carotene and CdSe-based nanocrystals
Norman Tschirner

Eidesstattliche Versicherung

Hiermit versichere ich an Eides statt, dass ich die vorliegende Dissertation selbständig verfasst habe. Alle benutzten Quellen sind in der Dissertation aufgeführt. Teile der Dissertation wurden schon veröffentlicht.

Berlin, den 20. Juli 2011

Raman spectroscopy of β -carotene and CdSe-based nanocrystals

Norman Tschirner

Erklärung

Teile dieser Arbeit wurden bereits veröffentlicht:

Interfacial alloying in CdSe/CdS heteronanocrystals, a Raman spectroscopy analysis.

N. Tschirner, H. Lange, Andrei Schliwa, Amelie Biermann, Christian Thomsen, Karel Lambert, Raquel Gomes, and Zeger Hens.

accepted at Chem. Mater.

Raman spectroscopy of PbTe/CdTe nanocrystals.

N. Tschirner, H. Lange, K. Lambert, Z. Hens, and C. Thomsen.

phys. stat. sol (b) **248**, 2748 (2011).

Polarised Raman measurements of β -carotene encapsulated in SWNTs.

N. Tschirner, K. Brose, J. Maultzsch, K. Yanagi, H. Kataura, and C. Thomsen.

phys. stat. sol (b) **247**, 2734 (2010).

Resonance Raman spectra of β -carotene in solution and in photosystems revisited: an experimental and theoretical study.

N. Tschirner, M. Schenderlein, K. Brose, E. Schlodder, M. A. Mrogiński, C. Thomsen, and P. Hildebrandt.

Phys. Chem. Chem. Phys. **11**, 11471 (2009).

The anomaly of the ν_1 -resonance Raman band of β -carotene in solution and in photosystem I and II.

N. Tschirner, K. Brose, M. Schenderlein, A. Zouni, E. Schlodder, M. A. Mrogiński, P. Hildebrandt, and C. Thomsen.

phys. stat. sol (b) **246**, 2790 (2009).

Raman excitation profiles of β -carotene - novel insights into the nature of the ν_1 -band.

N. Tschirner, M. Schenderlein, K. Brose, E. Schlodder, M. A. Mrogiński, P. Hildebrandt, and C. Thomsen.

phys. stat. sol (b) **245**, 2225 (2008).

Die Anmeldung der Promotionsabsicht ist weder früher noch gegenwärtig bei einer anderen Hochschule erfolgt.

Raman spectroscopy of β -carotene and CdSe-based nanocrystals

Norman Tschirner

Zusammenfassung

Diese Arbeit ist in zwei Teile gegliedert und untersucht mithilfe der Ramanspektroskopie die Schwingungseigenschaften des natürlichen Farbstoffs β -Karotin in unterschiedlichen Medien sowie den Einfluß von epitaktisch gewachsenen Hüllen auf aus CdSe aufgebauten sphärische Nanokristallen.

In der ersten Hälfte dieser Dissertation wird der bei der Photosynthese beteiligte Farbstoff β -Karotin untersucht. β -Karotin ist verantwortlich für die Lichtabsorption im Bereich von 460-520 nm und schützt den photoaktiven Organismus des Weiteren vor Schäden durch Radikale bei zu hoher Lichtintensität. Das Ramanspektrum des Moleküls wird in experimenteller sowie gerechneter Form vorgestellt und die vorhandenen Moden entsprechend ihrer Molekülschwingungen charakterisiert. Die Phononenfrequenz der intensivsten Ramanbande (ν_1 -Bande) zeigt eine Abhängigkeit von der Anregungswellenlänge. Durchgeführte DFT-Rechnungen belegen, dass die ν_1 -Bande von zwei nah benachbarten Schwingungsmoden gebildet wird. Die wellenlängenabhängige Verschiebung der ν_1 -Bande kann damit auf das unterschiedliche Resonanzverhalten der sie bildenden Untermoden zurückgeführt werden. Dieser Effekt konnte auch in β -Karotinmolekülen eingebettet in photoaktive Proteinkomplexe nachgewiesen werden. Überdies hinaus wurde der Einfluß von endohedral funktionalisiertem β -Karotin auf die vibronischen und elektronischen Eigenschaften von Kohlenstoffnanoröhren untersucht. Angefertigte Ramananregungsprofile zeigen eine schwache Blauverschiebung des E_{22} -Übergang sowie eine Abhängigkeit des Grades der Funktionalisierung vom Durchmesser der Nanoröhre.

Der zweite Teil dieser Arbeit beschäftigt sich mit CdSe-basierten kolloidalen Nanokristallen sphärischer Gestalt. Für diese existieren viele mögliche Anwendungen im Bereich der Optoelektronik und der Biotechnologie. Kolloidale Nanokristalle sind in Lösung synthetisierte Nanopartikel, deren optische Eigenschaften stark von der Größe und Form der Kristalle abhängig sind. Beide Parameter sind durch Anpassung der Synthesebedingungen variierbar und auch das Überwachsen der Kristalle mit einer Hülle aus (wenigstens) einem zweiten Material ist möglich. Eine solche Hülle verbessert die optischen Eigenschaften der Nanokristalle und ermöglicht damit z.B. eine weitere Funktionalisierung der Oberfläche. Auf der anderen Seite verursachen die unterschiedlichen Gitterparameter der verwendeten Stoffe Verspannungen im Nanokristall.

In dieser Arbeit wurden die durch CdS- und ZnS-Hüllen entstehenden Verspannungen in Nanokristallen mithilfe der Ramanspektroskopie quantitativ bestimmt und ihre Abhängigkeit bezüglich Hüllendicke und -kompositionen untersucht. Der CdSe-

Kern wird durch das Hüllenmaterial kompressiv verspannt, je mehr Hüllenmaterial deponiert wird, desto größer die resultierende Verspannung im Kern. Die Hülle auf der anderen Seite wird tensil verspannt und für reine CdSe/CdS-Nanokristalle wird die Verspannung durch das Wachstum größerer Hüllen reduziert. Eine detaillierte Analyse der in den experimentellen Ramanspektren zu sehenden Schwingungsmoden legt überdies hinaus die Bildung einer aus CdSeS bestehenden kristallinen Zwischenschicht nahe.

Ebenfalls aus den Ramanmessungen ableitbar ist die Kopplung der longitudinal-optischen Phononen an Exzitonen. Diese Kopplung zeigt ebenfalls eine Größenabhängigkeit und ist im Vergleich zu Volumenmaterial im Falle der Nanokristalle deutlich abgeschwächt. Dies beruht auf dem stark verminderten Einfluß der Coulomb-Wechselwirkung im Falle der Nanokristalle. Für überwachsene Kristalle ist diese Kopplung weiter vermindert was in Bezug gesetzt werden kann zu den unterschiedlichen Einschränkungen der Wellenfunktionen von Elektron und Loch innerhalb des Kern/Hülle-Systems.

Contents

1	Introduction	1
2	Raman spectroscopy	5
2.1	Macroscopic theory of inelastic light scattering	6
2.2	The Raman Tensor	7
2.3	Resonance Raman scattering, A- and B-Term scattering	8
2.4	Experimental setup	11
I	β-Carotene	13
3	β-Carotene	15
3.1	The role of β -carotene in photosynthesis	17
3.1.1	Photosynthesis	17
3.1.2	Chemical structure of the photosystems	20
3.1.3	β -Carotene in photosynthesis	24
4	The ν_1-anomaly of β-carotene	29
4.1	The Raman spectrum of β -carotene	30
4.2	The ν_1 -band of β -carotene	34
4.3	Resonance Raman spectra of β -carotene in photosystems I and II . .	41
5	Carotene functionalized carbon nanotubes	45
II	CdSe nanocrystals	55
6	Colloidal CdSe-based nanocrystals	57
6.1	Quantum and phonon confinement	58
6.2	Colloidal nanocrystal growth	61
6.2.1	Sample synthesis	64
6.3	Structural investigation	65

6.4	Optical properties of colloidal nanocrystals	67
7	Raman spectroscopy of CdSe based nanocrystals	71
7.1	The Raman spectra of CdSe and CdSe/CdS nanocrystals	71
7.1.1	CdSe/CdS/ZnS core-shell-shell heterostructures	74
7.2	Strain within the CdSe-based nanocrystals	77
7.2.1	Strain calculations	80
7.3	Interface composition	84
7.4	Exciton-phonon coupling	87
8	Summary	93

Chapter 1

Introduction

The basis of our daily life is the presence of oxygen, which we owe organisms capable of performing photosynthesis. Since these organisms are mostly greenish, the term "green" is in general connotated positively in our society, which is e.g. utilized by the political green parties.

Plants appear green due to the large fraction of the embedded green pigment molecule chlorophyll. However, in photosynthesis also other pigments play a decisive role, the most prominent among them is β -carotene. This molecule serves different purposes in the course of photosynthesis and appears red to the eye. In the fall it gives the leaves their picturesque autumnal look and is also commonly found in vegetables and fruits.

For living our daily life, one of the most important achievements of the modern civilization is the capability to enlighten the night. While our ancestors used fire to do so, in the modern world mankind uses the force of electric power, mostly generated from non-renewable resources. However, within the last 50 years mankind has strongly exploited the resources of our planet and the world population reaches nearly seven billion humans today. To continue living on a standard comparable to ours today, substantial issues have to be mastered in the future, especially in terms of energy conservation. Combined with the undisputable evidence of the climate change an increasing environmental consciousness has arisen since the 1970s and hopefully green thinking will further flourish in the minds of this and the upcoming generations.

This thesis deals with subjects related to both issues and is with regards to the content split into two parts. The first is about the vibrational properties of β -carotene ("being green") and the second comprehends issues on colloidal nanocryst-

tals ("thinking green").

The polyene related molecule β -carotene is, as mentioned before, an intrinsic constituent of any organic system able to carry out photosynthesis. Still today, the complex mechanism of photosynthesis is not encoded completely and unraveling the many functional implications of the more and more improving structural information accessible today is still a challenging enterprise[1, 2]. For a complete understanding of this evolutionary essential process, knowledge about the intrinsic properties of the different involved constituents is indissmissible. β -Carotene has next to its pure photoactive properties additional functions in photosynthetic proteins, e.g. it is a very potent radical scavenger and, thus, increases the lifetime of the photosynthetic apparatus the pigment is embedded in[3]. In this thesis the vibrational properties of β -carotene are analyzed in different environments. An abnormal shifting of the most prominent Raman band is discovered. This shifting is of particular interest in photosynthetic research sine it was correlated in the past to the perpendicular orientation of different carotene 'pools' within the photosynthetic protein subunits. In chapter 3 of this thesis, the properties of β -carotene and its function within photosynthesis are introduced. In chapter 4 the Raman spectra of the molecule in solution and inside photosynthetic proteins are discussed. Additionally, in chapter 5, β -carotene is embedded into carbon nanotubes and the influence of the pigment on the properties of the host molecule is discussed.

In the second part of this thesis, the structural and electronic properties of colloidal inorganic nanocrystals are investigated. Nanocrystals are a fairly new class of materials and are an intermediate between bulk structure and the molecular scale. These particles can be synthesized in solution and their sizes can be tuned from a few Ångstrom in diameter up to almost μm size[4]. They can be grown cheaply in large amounts from many different inorganic materials and also in a large variety of shapes[5].

Due to the (spatial) confinement present in the size regime of the nanocrystals the electronic properties of the nanocrystals depend strongly on their size and shape, like the band gap energy and the absorbance characteristic[6, 7]. The possibility to tune the electronic properties of the nanocrystals very percisely by simply manipulating their size and shape during the growth shows the high potentials these materials posses when it comes to industrial implemenation, *e.g.* nanocrystals are utilized to develop new types of LEDs[8] or to improve solar cell systems[9, 10]

Nanocrystals can be either grown out of one or several different components. The amount of deposited material is scalable down to a monolayer in thickness. A common way to produce nanocrystals is the growth of an initial core and a subsequent coating of the core with a shell out of at least one second material.

The surface of the grown shell layers can further be functionalized, e.g. allowing the solubility in water or any other solvent including biological tissue[11]. This

shows the possible implementation of nanocrystals into applications in the field of biotechnology. With specific receptors functionalized nanocrystals can be used as a fluorescent probe for imaging cancer cells[12, 13]. The bioconjugated nanocrystal possess binding sites for tumor cells and can attach to the cell. If loaded with additional antigens this approach results in a neutralization of the cancer cell by the production of antibodies by the immune systems.

Regarding the electronic energy levels, the growth of an additional shell leads to either a type-I or type-II band alignment. In type-I nanocrystals (which are considered in this work) the coating is primarily used to passivate the danglind bonds at the surface of the core and thus to improves the electronic properties of the whole core/shell structure. If the shell material is chosen appropriate the nanocrystals are also more stable in air or under UV radiation. However, due to different lattice mismatches, the growth of an additional shell leads to strain in the investigated system. Furthermore, the exciton wave function of the core is not only restricted to the core, but can propagate into the shell material.

Using Raman spectroscopy signals stemming from either the core or the shell region can be distinguished unambiguously. Changes in the core or shell areas can be monitored by observing the evolution of the corresponding Raman signal. This is used in this thesis to discuss the role of strain in CdSe-based nanocrystals as well as the issue of exciton-phonon coupling. Additionally, distinct feature in the Raman spectra give rise to the formation of a $\text{CdSe}_{1-x}\text{S}_x$ alloy layer at the interface between core and shell.

While chapter 6 introduces the synthesis of colloidal nanocrystals as well as their structural and optical characterization, chapter 7 deals with the properties accessible via Raman spectroscopy.

Chapter 2

Raman spectroscopy

The interaction of photons with matter is of high importance on every kind of length scale ranging from a nanometer (photonics) to an astronomic scale (e.g. x-ray astronomy). Despite this relevance, photons have only three different possibilities to interact with matter. Firstly, a photon can generate a pair of elementary particles if its energy exceeds a certain value (pair production). Secondly, photons can be absorbed by matter and excite electrons and/or ionize material. And thirdly, photons can interact with matter *via* scattering. Since this work is based on Raman spectroscopy, this third point is going to be discussed in more detail in this chapter. In the visible regime the most common way for photons to be scattered at matter is *via* elastic scattering. This process is the so-called Rayleigh scattering. However, a small fraction of visible light is scattered inelastically and therefore changes its frequency during the scattering process. The corresponding difference in energy excites vibrations inside the scattered medium. The inelastic scattering of visible light by molecular vibrations was named after Sir Chandrasekhara V. Raman, who was first in reporting it (Nobel price in 1930) [14, 15].

Since Raman spectroscopy is a versatile and non-destructive method it is in today's world a common tool used in a manifold of scientific as well as industrial fields. Due to the measurable vibrational response of the observed material, Raman spectroscopy allows a fast investigation of the vibrational properties, but also allows conclusions about the electronic properties as well as about chemical stoichiometry of the sample.

This chapter introduces the macroscopic as well as the microscopic theory of Raman scattering. The concept of A- and B-term scattering is introduced as well as the experimental setup primarily used in this work.

2.1 Macroscopic theory of inelastic light scattering

For an isotropic medium having the electric susceptibility χ the polarization $\vec{P}(\vec{r}, t)$ induced by a sinusoidal electromagnetic field $\vec{E}(\vec{r}, t)$ is given by

$$\vec{P}(\vec{r}, t) = \chi(\vec{k}_i, \omega_i) \vec{E}_i(\vec{k}_i, \omega_i) \cos(\vec{k}_i \cdot \vec{r} - \omega_i t). \quad (2.1)$$

The susceptibility $\chi(\vec{k}_i, \omega_i)$ is not a constant in time since it depends on the position of the atoms which are slightly altered by (induced) atomic vibrations. Atomic vibrations in a solid state are quantized into phonons which are present at ambient conditions. The displacement \vec{Q} of the atoms induced by a given phonon can be described as plane waves:

$$\vec{Q}(\vec{r}, t) = \vec{Q}(\vec{q}, \omega_0) \cos(\vec{q} \cdot \vec{r} - \omega_0 t) \quad (2.2)$$

with \vec{q} and ω_0 being the wavevector and the frequency of the phonon, respectively. Since the displacements will slightly modify the susceptibility in the medium we assume χ to be a function of \vec{Q} (adiabatic approximation). At room temperature, the amplitudes of displacements are small in comparison with the lattice constant and χ can be expanded in a Taylor series in $\vec{Q}(\vec{r}, t)$.

Inserting the 0th and 1st order of this Taylor series into equation 2.1 leads to the following expression for the polarization of the medium:

$$\vec{P}(\vec{r}, t, \vec{Q}) = \vec{P}_0(\vec{r}, t) + P_{ind}^{\vec{r}}(\vec{r}, t, \vec{Q}) \quad (2.3)$$

with

$$\vec{P}_0(\vec{r}, t) = \chi_0(\vec{k}_i, \omega_i) \vec{E}_i(\vec{k}_i, \omega_i) \cos(\vec{k}_i \cdot \vec{r} - \omega_i t) \quad (2.4)$$

and

$$P_{ind}^{\vec{r}}(\vec{r}, t) = \left(\frac{\partial \chi}{\partial \vec{Q}} \right)_0 \vec{Q}(\vec{r}, t) \vec{E}_i(\vec{k}_i, \omega_i) \cos(\vec{k}_i \cdot \vec{r} - \omega_i t). \quad (2.5)$$

In equation 2.4 $\chi_0(\vec{k}_i, \omega_i)$ denotes the electric susceptibility for an unpertubated state with no fluctuations inside the medium, while $\vec{P}_0(\vec{r}, t)$ describes a vibration in phase

with the incident light. This process is the elastic Rayleigh scattering which is in the visible regime about 10^6 times more dominant than the second term (equation 2.5).

Rewriting equation 2.5 using harmonic expressions leads to

$$\vec{P}_{ind}(\vec{r}, t, \vec{Q}) = \frac{1}{2} \left(\frac{\partial \chi}{\partial \vec{Q}} \right)_0 \vec{Q}(\vec{q}, \omega_0) \vec{E}_i(\vec{k}_i, \omega_i t) \cdot \left\{ \cos \left[(\vec{k}_i + \vec{q}) \cdot \vec{r} - (\omega_i + \omega_0)t \right] + \cos \left[(\vec{k}_i - \vec{q}) \cdot \vec{r} - (\omega_i + \omega_0)t \right] \right\}, \quad (2.6)$$

Equation 2.6 is an expression consisting of two sinusoidal waves. With respect to the incident electromagnetic wave one of these two waves is shifted with wavevector $\vec{k}_{AS} = (\vec{k}_i + \vec{q})$ and frequency $\omega_{AS} = \omega_i + \omega_0$ (anti-Stokes) while the other one is shifted with wavevector $\vec{k}_S = (\vec{k}_i - \vec{q})$ and frequency $\omega_S = (\omega_i - \omega_0)$ (Stokes). The difference of ω_S and ω_{AS} with respect to ω_i is called Stokes and anti-Stokes shift, respectively or just simply Raman shift.

2.2 The Raman Tensor

The information given in the last section showed that the measurable Raman intensity is correlated with the change in susceptibility along a certain atomic displacement. This fact was expressed mathematically with the first order Taylor series leading to the expression

$$\left(\frac{\partial \chi_{ij}}{\partial Q_m} \right)_0 Q_m, \quad (2.7)$$

with the indices i and j being the three dimensions and the indice m describing the the number of possible vibrational modes. The term $\left(\frac{\partial \chi_{ij}}{\partial Q_m} \right)_0$ is a third rank tensor which can be transferred into a second rank tensor by focusing on a specific mode m and by introducing the unit vector $\hat{Q} = \vec{Q}/|\vec{Q}|$. This tensor is called the Raman Tensor:

$$\underline{\underline{R}} = \left(\frac{\partial \chi}{\partial \vec{Q}} \right)_0 \hat{Q} \quad (2.8)$$

The Raman tensor displays the symmetry of a given lattice structure and can be calculated with the help of symmetry considerations and group theory.

The measurable intensity of the scattered light has also to depend on the polarization of the scattered radiation, $\underline{\vec{e}}_s$, as $|\underline{\vec{R}} \cdot \underline{\vec{e}}_s|^2$. With $\underline{\vec{e}}_i$ being the polarization of the incident radiation the scattered intensity I_S is proportional to

$$I_S \propto |\underline{\vec{e}}_i \cdot \underline{\vec{R}} \cdot \underline{\vec{e}}_s|^2. \quad (2.9)$$

2.3 Resonance Raman scattering, A- and B-Term scattering

The intensity of Raman signals can be enhanced by several orders of magnitude if the wavelength of the incident laser fits with an optical allowed transition of the probed sample. Since in such case not virtual, but optical states are involved the probability of a scattering process is for obvious reason amplified. The theory of the resonant Raman effect distinguishes two intensity enhancement mechanisms: the so-called Franck-Condon and Herzberg-Teller scattering. The former involves the displacement of the potential minima of the ground and excited electronic states along a vibrational normal coordinate Q_k , while the latter involves a transfer of the transition momentum between two excited states having similar transition energies[16].

For a given scattering process involving a molecular transition from an initial state $|g\rangle$ into a state $\langle f|$ induced by a phonon of frequency ν_0 , the scattering probability in form of the polarizability transition moment $[\alpha]$ for a transition k is given by the Kramers-Heisenberg dispersion equation:

$$[\alpha_{ij}]_k = \frac{1}{\hbar} \sum_r \left(\frac{\langle f | M_i | t \rangle \langle t | M_j | g \rangle}{\nu_t - \nu_g - \nu_0 + i\Gamma_t} + \frac{\langle f | M_j | t \rangle \langle t | M_i | g \rangle}{\nu_t - \nu_g + \nu_0 + i\Gamma_t} \right) \quad (2.10)$$

where i and j (=x,y,z) are representing the polarization of the incident and scattered light, respectively. The summation is over all possible intermediate states $|t\rangle$. M is the electron position operator, the integrals $\langle f | M_j | t \rangle$ and $\langle t | M_i | g \rangle$ are the electric dipole transition moments. To prevent the denominator to become zero in the case of resonance a damping factor Γ_r is included, which represents the sharpness and finite lifetime of the intermediate state $|t\rangle$.

Following Albrecht[17], in resonance ($\nu_r - \nu_g \approx \nu_0$) the second term of Equation

2.10 can be neglected because the first term will become dominant for a certain electronic state $|e\rangle$. Applying the adiabatic Born-Oppenheimer approximation of separability of electronic and vibrational wave functions due to the faster movement of the electrons with respect to the core leads to

$$[\alpha_{ij}]_k = \frac{1}{\hbar} \sum_{\eta} \left(\frac{\langle j | (\mu_i)_e | \eta \rangle \langle \eta | (\mu_j)_e | i \rangle}{\nu_{\eta i} - \nu_0 + i\Gamma_{\eta}} \right), \quad (2.11)$$

with $(\mu_i)_e$ and $(\mu_j)_e$ denoting the electronic transition elements $\langle g | (\mu_i)_e | e \rangle$ and $\langle e | (\mu_j)_e | g \rangle$ for the resonant excited state e , respectively. $|i\rangle$, $|j\rangle$ and $|\eta\rangle$ are wave functions of the vibrational states and depend on the normal coordinates Q_k . η is a defined vibrational level of the excited state having the bandwidth Γ_{η} , $\nu_{\eta i}$ is the transition frequency from the ground vibrational level i to the level η . Since the Born-Oppenheimer approximation is valid and the dependence of μ_e with respect to Q_k is small, μ_e can be expanded as a Taylor series:

$$\mu_e = \mu_e^0 + \sum_k \frac{\partial \mu_e}{\partial Q_{k0}} Q_k + \dots \quad (2.12)$$

Substitution of 2.12 into 2.11 results in an expression which can be written as a sum of two terms

$$[\alpha_k] = A + B + \dots \quad (2.13)$$

where

$$A = (\mu_e^0)^2 \hbar^{-1} \sum_{\eta} F_{\eta} (\nu_{\eta i} - \nu_0 + i\Gamma_{\eta})^{-1}; \quad F_{\eta} = \langle j | \eta \rangle \langle \eta | i \rangle \quad (2.14)$$

and

$$B = \mu_e^0 \frac{\partial \mu_e}{\partial Q_{k0}} \hbar^{-1} \sum_{\eta} F_{\eta} (\nu_{\eta i} - \nu_0 + i\Gamma_{\eta})^{-1}; \quad (2.15)$$

$$F_{\eta} = \langle j | m Q_k | \eta \rangle \langle \eta | i \rangle + \langle j | \eta \rangle \langle \eta | m Q_k | i \rangle.$$

The A-term is the leading resonance Raman scattering mechanism and contains the so called Franck-Condon overlap integrals $\langle j | \eta \rangle$ and $\langle \eta | i \rangle$. These integrals become

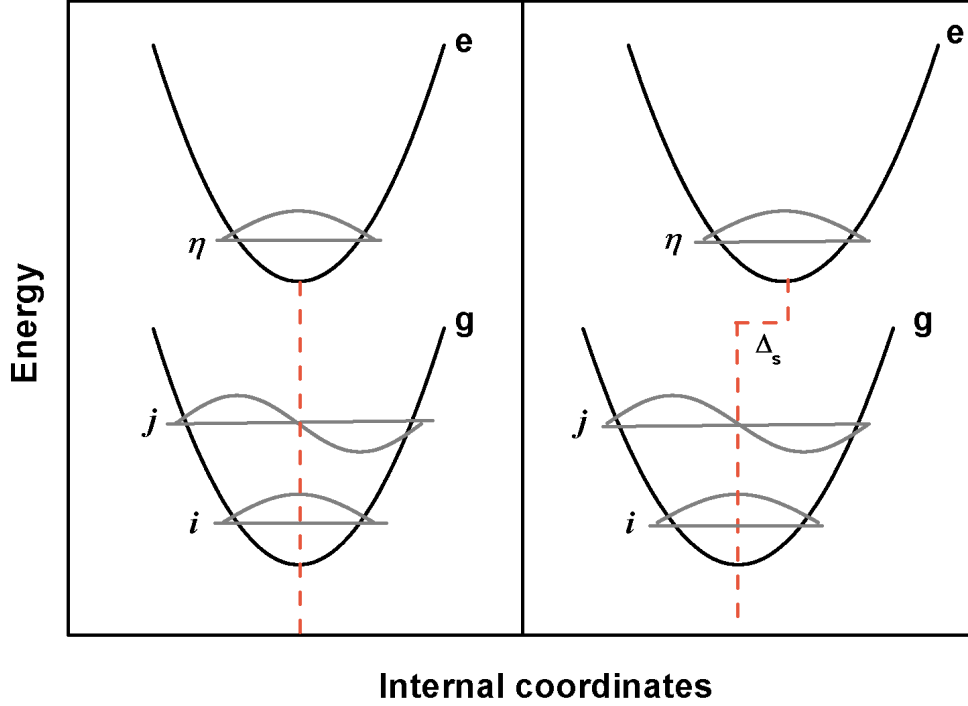


Figure 2.1: Ground- and excited-state potential for $\Delta_s = 0$ (left hand side) and $\Delta_s \neq 0$ (right hand side). In the latter case the intensity of the transition $\langle j|\eta\rangle \langle \eta|i\rangle$ becomes nonzero because the convolution integral $\langle j|\eta\rangle$ does not vanish.

nonzero if there is a difference in the involved vibrational frequencies of ground and excited state exists or/and if there is a shift of the excited state potential with respect to the ground state potential along the vibrational coordinate, Δ_s (see Fig. 2.1). If Δ_s is large and $\nu_i \neq \nu_j$ this vibrations will appear strongly in the resonance Raman spectra, because both convolution integrals are nonzero. In general, totally symmetric modes exhibit considerable displacements, while non-totally symmetric modes do not [18].

The B-Term scattering arises from the interaction of the excited state $|e\rangle$ with an additional excited state of appropriate symmetry $|s\rangle$. The electronic transition moment in the case of vibronic coupling can be expressed as

$$\left(\frac{\partial \mu_e}{\partial Q_k}\right)_0 = \frac{\mu_s^0 \langle s | (\partial H_e / \partial Q_k)_0 | e \rangle}{\nu_s - \nu_e} \quad (2.16)$$

with H_e being the Hamiltonian for the total energy and $(\partial H_e / \partial Q_k)_0$ being the

vibronic coupling operator between the two excitable states $|e\rangle$ and $|s\rangle$. μ_s^0 and ν_s are the transition dipole moment and the frequency of the mixing state. Equation 2.16 describes the vibronic mixing of the two involved states along the coordinate Q_k ; the excited state $|e\rangle$ gains absorption strength by vibronic coupling. The closer the two excited states are neighbored in energy and the more pronounced the transition to the state $|s\rangle$ is, the larger $(\frac{\partial\mu_e}{\partial Q_k})_0$ will be. The B-term scattering (also called Herzberg-Teller scattering) is a prime cause of resonance Raman activity for non-totally symmetric modes [18].

2.4 Experimental setup

Since the Raman signal of a given sample is rather low in contrast to the exciting laser system it is essential for an experimental Raman setup to suppress the amount of elastically scattered light. To achieve this, a triple gate monochromator setup was used in the course of this work. In this setup the first two (pre-)monochromators are operating in subtractive configuration and act like a bandpass filter for the exciting light as well as for stray light. The dispersion of the light is done by the third monochromator; its degree of dispersion is tunable by using gratings having different grooves per millimeter; the most common used gratings had 1800 and 2400 grooves/mm.

Since the drives of the monochromators are not adjustable with the affordable precision each spectrum was calibrated with respect to neon and argon lines. For the final detection of the scattered light a nitrogen cooled silicon based charge coupled device was used. The setup provided an accuracy of the Raman shift of $\pm 0.4 \text{ cm}^{-1}$. The used setup is shown in Fig. 2.2 and could be run using two different modes: either macro or micro mode. The latter provides a smaller focus spot and higher power densities and is therefore useful for the observation of single objects or small areas. The data of the carbon nanotubes with and without incorporated β -carotene as well as the measurements of the two photosystems were recorded using the micro mode.

The macro configuration is mainly used for wider areas as well as for dissolved samples. Because of the larger focus spot local heating and possible vaporization of the solvent is prevented. All spectra stemming from β -carotene and the CdSe nanocrystals were recorded using the macro mode.

For excitation, different laser sources were used. An Ar-ion laser setup (Coherent) provided twelve lines in the region from 457 - 647 nm, a HeCd-laser (Omnichrome) was used to excite samples at 442 nm and a dye laser (Radiant Dyes) running on Rhodamin 6G was delivering tunable excitation energy in the region from 570 - 615 nm. In all cases a pre-monochromator was used to suppress plasma lines originating

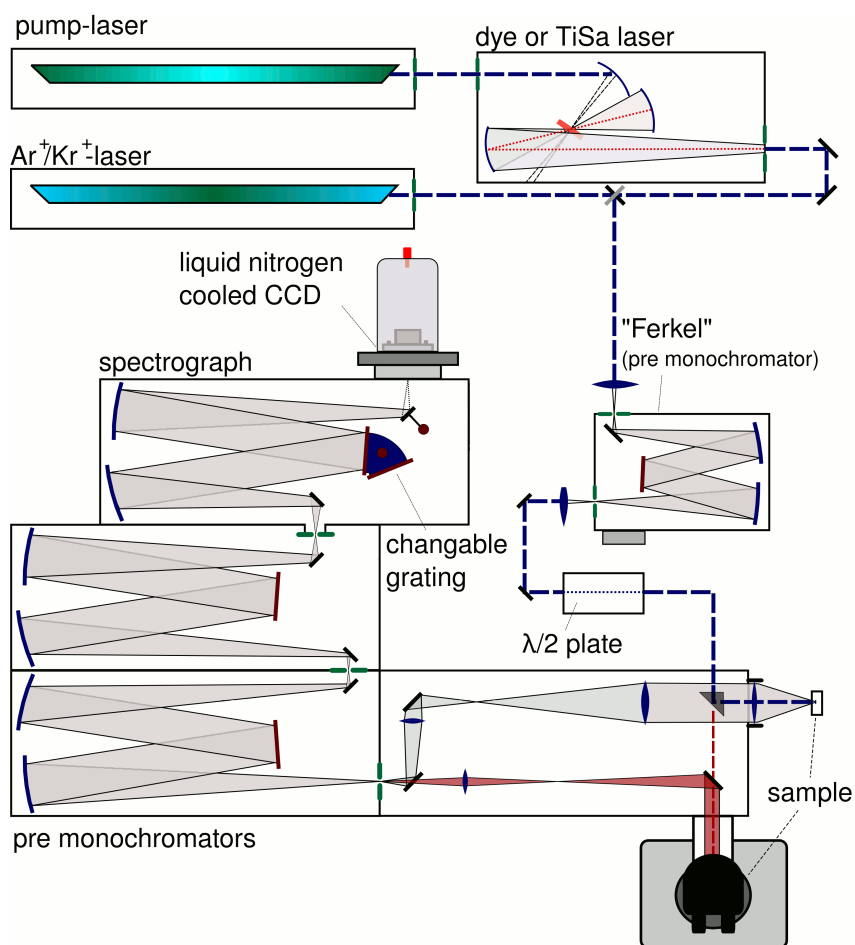


Figure 2.2: Experimental Raman setup. The blue dashed line corresponds to the optical path of the macro setup. The red dashed line is the micro pathway. The picture was taken from [19].

from the laser tube. The laser power on the sample was kept below 10 mW to avoid laser heating[20].

For low temperature experiments an Oxford microcryostat was used for Helium temperatures while a Linkam THMS600 stage was used for nitrogen temperatures. The temperature accuracy was ± 5 K for both cryostats.

Part I

β -Carotene

Chapter 3

β -Carotene

This chapter introduces the basic properties of β -carotene. Since this thesis also involves measurements on β -carotene-containing photoactive proteins, an introduction to the complex process of photosynthesis is given and the impact of the β -carotene molecules on the course of photosynthesis is presented.

The molecule β -carotene is probably the most famous molecule belonging to the chemical class of the carotenoids, which is one of the most widespread families of naturally occurring pigment molecules. The family is named after the carrot, whose color is due to the incorporation of β -carotene. Several other plants also contain carotenoids in higher amounts, e.g. lycopene is responsible for the color of the tomato and the yellow/reddish color of leaves in fall is mainly due to the carotenoid fraction inside the leaf, which is enriched due to the degradation of chlorophyll.

More than 600 different carotenoids are known these days and the family of carotenoids is commonly divided into two chemical classes: the xanthophylls and the carotenes. The two classes differ in the chemical composition: while all molecules in the carotene class solely consist of carbon and hydrogen atoms, xanthophyll molecules also contain oxygen.

Chemically, carotenes are terpenoids consisting of eight isoprene units (C_5H_8) with the chemical formula $C_{40}H_{56}$. The two most common carotene isomers are α - and β -carotene. The structure of β -carotene is shown in Fig 3.1 and was at first deduced by Karrer et al.[21]. The central pattern, which is repeated in all carotenoids, is a backbone consisting of alternating single and double carbon bonds forming a conjugated π -electron system. This π -system is responsible for most of the spectroscopic properties of the carotenoids. In case of β -carotene the molecule is terminated at both ends by a ring-structure referred to as beta-ionone rings. Comparing α - and β -carotene, both molecules are very similar in their chemical structure, the only

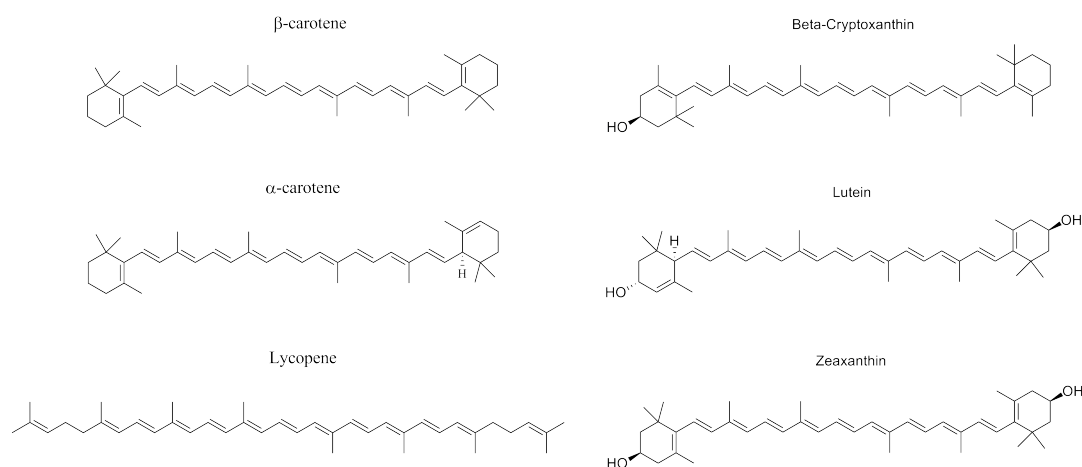


Figure 3.1: Chemical structure of the six most important carotenoids for the health care of the human body.

difference is the position of a double bond in one of the terminating cyclic groups. β -Carotene absorbs strongly in the blue-green regime and therefore appears red. This is a general trend for carotenenes, which all have a reddish color due to the same number of conjugated double-bonds, which defines the absorption range of a dye molecule.

For the protection of the human body six carotenoids are of special interest: β -carotene, α -carotene, Lycopene, β -Cryptoxanthin, Lutein and Zeaxanthin (see Fig. 3.1 for their chemical structure). These molecules mainly serve as antioxidants and prevent free radical damage to DNA, proteins and lipids. Due to mutations these unintentional oxidations could otherwise cause illnesses like cancer, arteriosclerosis, rheumatism, Parkinson's disease or simply the aging of the skin.

The carotenoids α -carotene, β -carotene, γ -carotene and beta-cryptoxanthin are of special interest for herbivore and omnivore, because they serve as a vitamer for retinol. Retinol is one of the many forms of vitamin A and its aldehyde is retinal, which is of high importance for the visual system. In its 11-cis-isomere, retinal is bound to the protein opsin and builds rhodopsin. Rhodopsin is embedded in the retina and responsible for the first events in the perception of light. Exposed to light, the 11-cis-retinol is isomerized to the all-trans form and can dissociate from the protein. This process is accompanied by the induction of a nervous signal, which is analyzed by the visual center of the brain and finally leads to a visual impression.

In nature, plants and fungi are the only organic systems able to synthesize β -carotene, humans though have to cover their daily needs by diet, mainly vegetables and fruits. The Wittig-reaction is used to synthesize β -carotene on an industrial

scale[22]. The Wittig reaction is a regioselective chemical reaction between ketons and phosphonium ylides and leads to the formation of alkenes and phosphine oxides. Due to the regioselectivity and the availability of appropriate chemical building blocks, β -carotene was actually the first molecule to be synthesized *via* Wittig-reaction by the Baden Aniline and Soda Factory (BASF).

3.1 The role of β -carotene in photosynthesis

Since β -carotene is a pigment molecule, its existence and use in photosynthetic active species is not peculiar. This section gives a brief overview of photosynthesis. A detailed description of the carotene-containing photosystems I and II and the functions of the molecule within these proteins is discussed in the next sections.

3.1.1 Photosynthesis

Photosynthesis is one of the most complex processes in nature and many details are still not totally understood today. Photosynthesis occurs in all plants and some types of bacteria and is simply the transformation of light energy into chemical energy. For eukaryotes photosynthesis takes place within the chloroplasts, which are subunits of plant cells being located at the bottom side of a leaf. The chloroplasts contain a liquid called stroma and membrane-bound structures exhibiting a disk-like shape, the thylakoids. The interior of the thylakoids is filled with a liquid called the lumen. The thylakoids swim in the stroma and they can form stacks consisting of several thylacoid discs; these formations are referred to as grana. The actual photosynthesis occurs within the membrane of the thylakoids, where all proteins, relevant for photosynthesis, are embedded[23, 24]. Essential for the photosynthesis in eukaryotes are four different proteins: the photosystems I and II (PS I and II), the cytochrome b_6f complex and the ATP-synthase (see Fig. 3.2)[25]. Only the former two are able to use sunlight to form an excited electron. The cytochrome b_6f complex plays two different roles: firstly, it acts as an electron agent transporting electrons from the PS II to the PS I. Secondly, it drives the transport of H^+ -ions from the stroma into the lumen. This leads to an H^+ gradient between stroma and lumen and makes the lumen acidic down to pH values of 4. The proton gradient is used chemiosmotically by the protein ATP synthase, which performs the transformation of adenosine diphosphate (ADP) to the energy-richer adenosine triphosphate (ATP) [26].

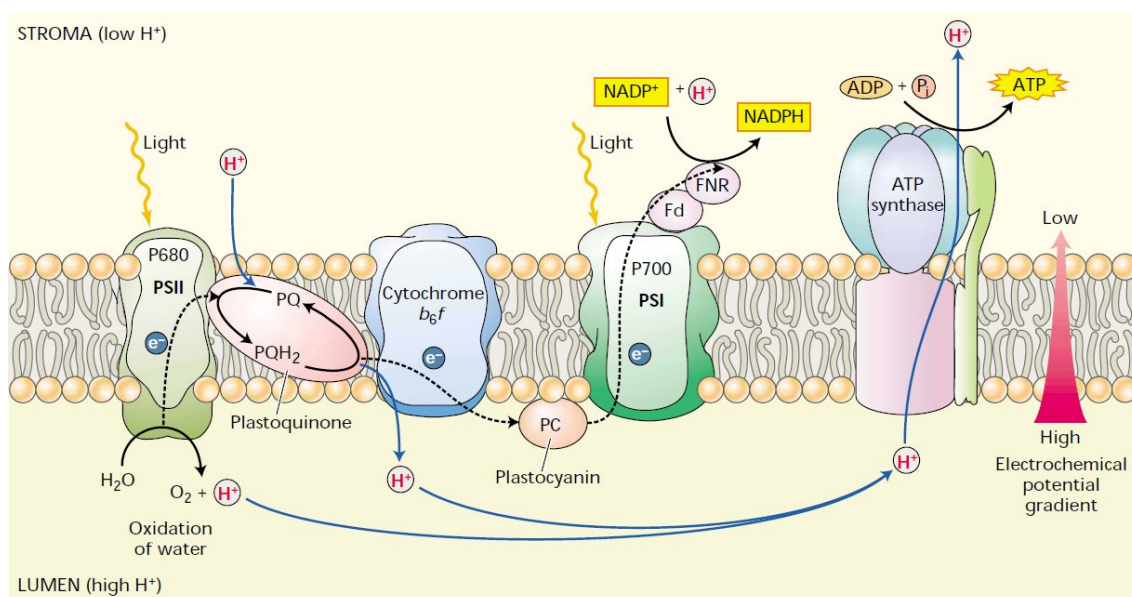


Figure 3.2: Sketch of the thylakoid membrane and its embedded proteins. The sketch is taken from [23]

The basic processes of photosynthesis are shown in Figure 3.2 and 3.3. As shown in Fig. 3.2 all four proteins are working in series, although the location of each protein within the thylakoid membrane is not as coincidental as Fig. 3.2 might suggest; this membrane composition is just a guide to the eye. The driving force of photosynthesis is the flow of electrons through the proteins. This flow is called the electron transport chain and its visualization is referred to as the Z-scheme, which is depicted in Fig. 3.3. To trace the electron transport chain, let us assume the process of photosynthesis is started by the absorption of a photon by the PS II. Although this approach does not reflect the non-linear course of photosynthesis, it is the most apparent one. The photon is absorbed by a pigment (e.g. a chlorophyll or a carotene) located within the PS II and the energy of this photon is transferred efficiently to the reaction center (RC) of the PS II by dipole-dipole resonance transfer. Within the RC the photon energy causes a charge separation realized by a special pair of two closely neighbored chlorophylls (Chls) called P_{680} . The number 680 refers to the absorption maximum of the protein; so in case of PS II this is 680 nm. To disjoin electron and hole from each other spatially, the excited electron is in a first step rapidly (≈ 300 ps [1]) transported to a plastoquinone (Q_A) also located within the RC of the PS II. In a second, slower step (200 - 800 μs) the electron is transferred to a second plastoquinone (Q_B) which, after its double reduction, leaves the PS II and diffuses into the lipid matrix of the thylakoid membrane as a plastoquinol. The reoxidation of the PS II reaction center occurs by the dissociation of water.

This process is performed by the so-called oxygen-evolving-complex (OEC), which catalyzes the reaction $2\text{H}_2\text{O} \rightarrow 4\text{H}^+ + 4\text{e}^- + \text{O}_2$. Due to the location of the OEC at the interior of the thylakoid membrane the four formed protons dissociate into the lumen.

Please note, that water is a very stable molecule and the oxidation of water therefore requires a high redox potential. The OEC of the PS II is the only known biological system which is capable of carrying out this reaction. It should also be mentioned that the produced O_2 is a waste product and responsible for almost all oxygen in the atmosphere of this planet[27].

Leaving the PS II, the plastoquinol is diffusion driven transferred to the cytochrome b_6f complex, the second protein involved in the electron transport chain (see Fig. 3.2). Entering the cytochrome b_6f complex, the plastoquinol is reoxidized into plastoquinone and the occurring electrons are used to reduce the protein plastocyanin. Plastocyanin is a monomeric copper-containing protein[28]. It is located inside the lumen and is used as an electron carrier protein. Besides the reduction of plastocyanin, the oxidation of plastoquinol inside the cytochrome b_6f -complex also shovels protons from the stroma into the lumen and drives the ATP synthesis just as the OEC does.

Plastocyanin in its reduced state has a binding site for oxidized PS I. The PS I is, as well as PS II, capable of light absorption. The special pair of PS I is referred to as the P_{700} , since the absorption maximum of PS I is 700 nm. If excited, the

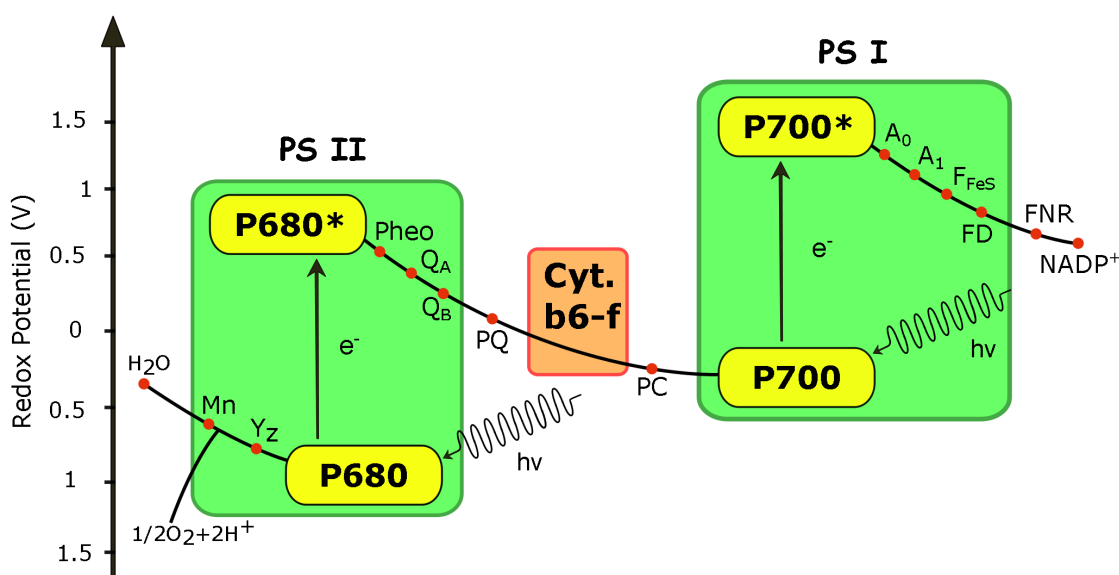


Figure 3.3: Z-scheme of the photosynthesis.

electron is replaced in the RC by the docked plastocyanin which supplies the PS I with its carried electron originally stemming from PS II. In contrast to PS II, the energy of the photon can be directly used to save chemical energy since the electron is rapidly transferred *via* three 4Fe-4S clusters to an iron-sulfur protein called ferredoxin. The ferredoxin mediates the electron to either a protein called ferredoxinNADP⁺-reductase or back to the cytochrome *b₆f*-complex. The former pathway drives the formation of the energy-rich molecule NADPH by the reaction $NADP^+ + e^- \rightarrow NADPH$, while the latter pathway increases the H^+ -gradient between stroma and lumen, which is vital for the formation of ATP. Overall, the photosynthesis yields in a total energy gain of 2880.3 kJ/mol_{C₆H₁₂O₆} for superior plants and cyanobacteria[29].

3.1.2 Chemical structure of the photosystems

As mentioned before, the only two protein units capable of performing light harvesting are the photosystems I and II. The two systems are labeled I and II simply because PS I was discovered before PS II. Today, the chemical structure of both systems have been obtained by means of X-ray diffraction with resolutions of 2.5 Å and 2.9 Å for PS I and PS II, respectively[30, 31]. The data was not acquired from plants, but from the thermophilic cyanobacteria *Synechococcus elongatus* and *Thermosynechococcus elongatus*. There are slight differences in the number of integrated protein subunits between the photosystems of cyanobacteria compared to eukaryots and prokaryots. One major structural difference between plant and bacterial PS I is the binding site for PC, which is, in case of the plant, more pronounced and is in terms of efficiency also two orders of magnitude faster than in cyanobacteria [32, 33]. The main function of the two photosystems, however, is unaffected by these deviations. For a summary on the specific number and arrangements of the subunits please see ref. [34].

Figure 3.4 and 3.5 show the structural models of the two photosystems obtained from the X-ray data. For a more distinct perception only the α -helices of the different (color-coded) protein subunits and the pigments building the RC are shown. The pigment molecules responsible for the collecting and transport of the photon energy into the RC are also located within the α -helices, but not shown.

The X-ray data reveal, that the PS I consists of 12 protein subunits and additional 127 cofactors. 96 of these cofactors are chlorophylls and further 22 carotenes, 16 of those *all-trans*- β -carotene. Nine of the twelve subunits features transmembrane α -helices, the three stromal subunits exhibit a β -sheet structure (red colored structure at the upper side of the side view in Fig. 3.4). The two largest protein subunits are called PsaA and PsaB and are colored in yellow and green in Fig. 3.4. Both subunits are related by a pseudo- C_2 -axis located at the center of the monomer. The cofactors

of the RC are arranged within these subunits. The RC is formed by six chlorophylls, two phylloquinones and three Fe_4S_4 clusters. The former two are arranged in two branches A and B which are orientated along the C_2 -axis of the PsaA/B. In contrast to PS II there are no carotene molecules directly integrated into the RC.

One wonders whether both branches are active in the cause of charge separation. Electron-nuclear double resonance studies of PS I mutations show that most of the electronic spin density of the excited P700^+ is located on the PsaB side of the RC[35]. Most of the 127 cofactors are primarily bound to the PsaA/B-units. All other membrane subunits contribute mainly to the coordination of the antenna cofactors. The arrangement of the 22 carotene molecules shows a substructure in terms of a division into six sub-clusters. All carotenes are in van-der-Waals contact ($<3.6 \text{ \AA}$) to a total of 60 chlorophyll molecules. This close distance facilitates an efficient energy transfer between the molecules as well as quenching of chlorophyll triplet states *via* Dexter transfer[30].

The subunit composition of PS II is slightly more complex than of PS I. The PS II is built out of a total number of 20 protein subunits and 73 cofactors (among them 35 chlorophylls and 12 carotenes). Similar to PS I the RC is embedded within two polypeptide subunits. In the case of PS II these are referred to as D1 and D2. The

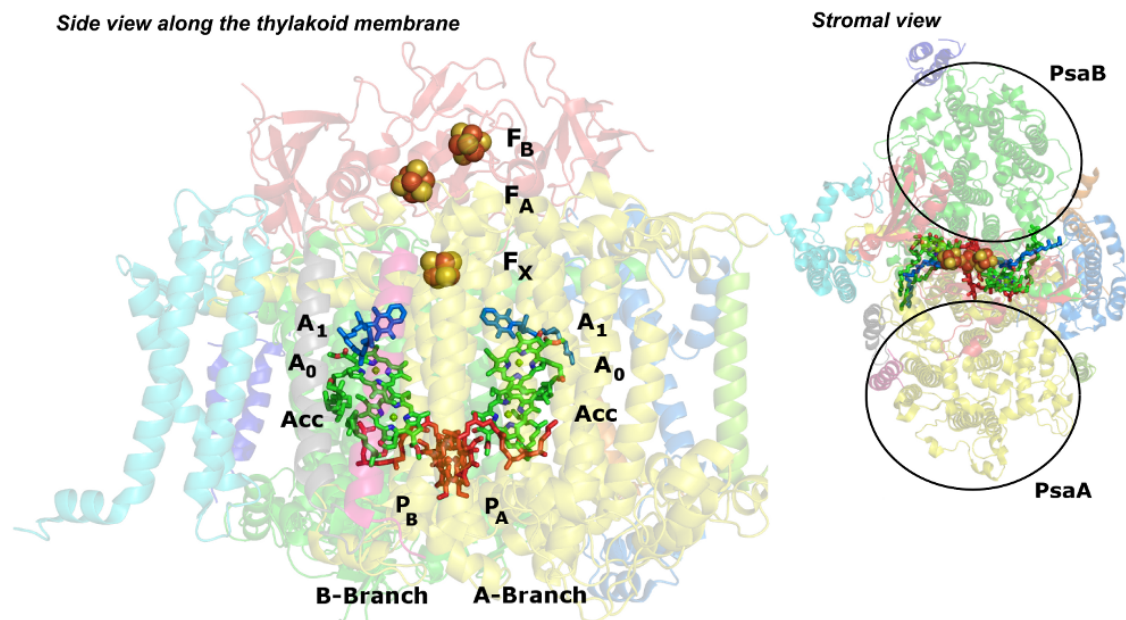


Figure 3.4: Side- and stromal view of the PS I. The RC is highlighted and its constituents are labeled. The protein backbone is shown transparent. The PSI structural data stems from [30].

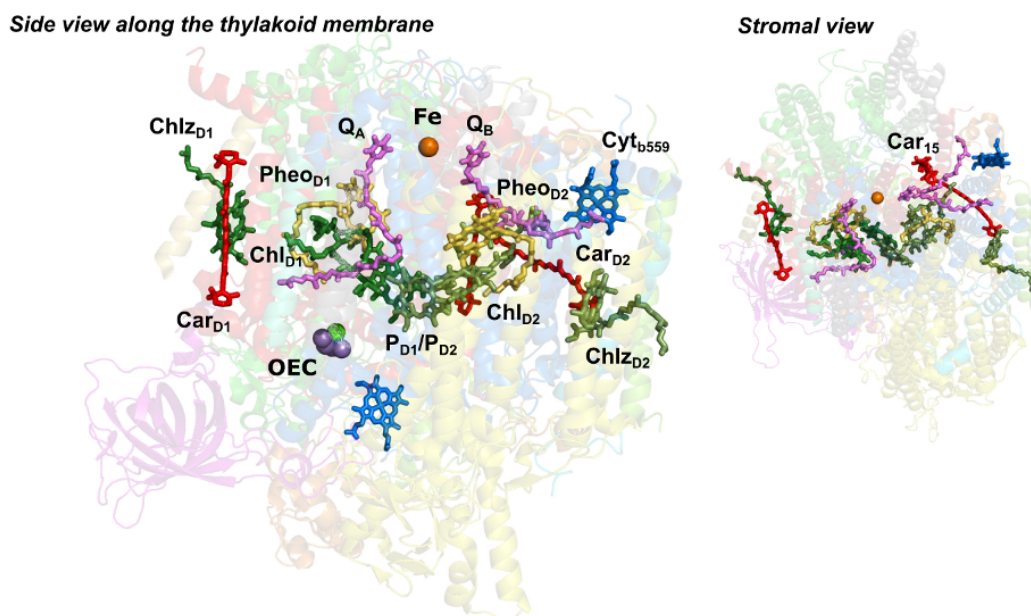


Figure 3.5: Side- and stromal view of the PS II. The RC is highlighted while the protein backbone is shown transparent. The constituents of the reaction center are labeled. The PS II structure is taken from [31].

RC itself is built by six chlorophylls, two pheophytin, two plastoquinone and three β -carotene in *all-trans*-configuration (see Fig 3.5)[31, 36]. The arrangement of the involved pigments shows a symmetric branch-like structure also similar to the RC of PS I.

In contrast to PS I, the RC of PS II is surrounded by 11 lipids separating it from the antenna and smaller subunits. The functions of these lipids is unclear, but their appearance provide a structural flexibility to the photosystem which might be required for local mobility of the subunits in case of damage replacement[36]. Analysis of the crystal structure indicates that the four closely spaced chlorophyll molecules labeled P_{D1} , P_{D2} , Chl_{D1} and Chl_{D2} are the primary electron donor of the P_{680} . In case of P_{680}^* the excited electron is delocalized over all four Chls before it is donated to the pheophytin a ($Pheo_{D1}$), which serves as the primary electron acceptor. The light-driven charge separation occurs solely by the left D_1 branch, while the D_2 -branch stays inactive. Nevertheless, there are, besides the primary electron transfer, alternative reactions occurring with a low quantum yield, which possibly function as protection against light-induced stress[3, 37]. These electron transfer pathways can be monitored at low temperature (below 180 K) when the light-induced electron transfer in PSII leads to the formation of $P_{680}^+Q_A^-$ and subsequent charge recom-

bination since electron transfer from Q_A^- to Q_B and from Y_Z to P_{680}^+ is inhibited. Upon repetitive excitation by flashes or continuous illumination, the amplitude indicating the formation of $P_{680}^+Q_A^-$ decreases to about 20 % [38]. This finding is explained by the oxidation of secondary electron donors (Cyt *b559*, Car, Chl_Z) by P_{680}^+ that occurs with low quantum yield in competition with the charge recombination of $P_{680}^+Q_A^-$.

Considering the pigment molecules, 29 chlorophylls and 8 carotenes are arranged for an efficient energy transfer in two subunits neighboring the D1/D2 units; these are called CP43 and CP47. As in the PS I, most of the carotene molecules are located in van-der-Waals distance to chlorophyll molecules, allowing transfer of excitation energy as well as photoprotection. There are, in contrast to the PS I, three β -carotene molecules present in the RC of PS II. These molecules are not bound within the van-der-Waals distance to chlorophyll or other neighboring constituents, according to the Moser-Dutton rule their distance to the next molecule is more than 18 Å [39]. The purpose of these carotenes lies in the photoprotection of the RC and is discussed in the next section.

A unique feature of the photosystem II is its capability to split water via hydrolysis. The water splitting within the OEC is catalyzed by a manganese-containing cofactor located at the interior of the thylakoid membrane. Four manganese atoms and an additional magnesium can adopt different conformations within the complex and are able to store the four electrons, which are generated *via* photolysis. The detailed arrangement of the atoms and the functional mechanism of the complex are not yet completely understood due to the impreciseness of the given X-ray diffraction data,

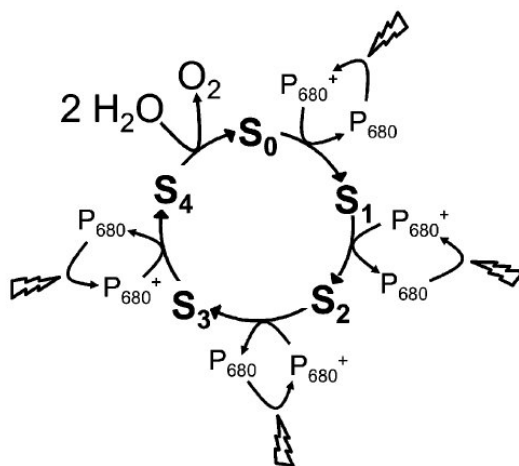


Figure 3.6: Sketch of the catalytic cycle of the OEC (Kok-cycle). All transitions except the $S_4 \rightarrow S_0$ transition are used to reoxidize P_{680}^+ to P_{680} . The $S_4 \rightarrow S_0$ is independent of light and releases O_2 . The picture is taken from Ref. [27]

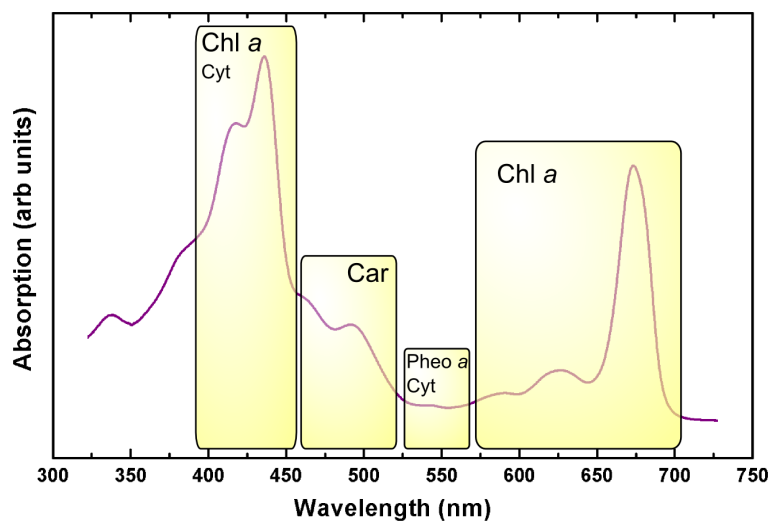


Figure 3.7: Absorption spectrum of photosystem II. The wavelength dependent impact of the intrinsic pigment molecules is shown.

but at least five different conformation states are known. These states are referred to as S-states and their photon absorption driven progression during photosynthesis is referred to as the Kok-cycle (see Fig. 3.6)[40]. The states differ in their redox potential, which is in the S_4 arrangement high enough to split water via hydrolysis. The H^+ ions produced by the photolysis are released into the lumen increasing the H^+ -gradient between stroma and lumen, which drives the ATP synthesis *via* the ATP synthase protein[41]. The efficiency of the hydrolysis is 20 % taking into account that light is absorbed across the whole visible regime [42].

To summarize, comparing the monomer forms of the two photosystems involved in photosynthesis reveal several similarities. Both are membrane-bound proteins with high quantum yields, in the case of PS I it is close to one[43]. Both exhibit reaction centers with a two-branch like structure and a pseudo- C_2 symmetry embedded within mainly two protein subunits. The alignment and distribution of antenna chlorophyll molecules bound to proteins are similar and in both photosystems carotene molecules are located in van-der-Waals distance to chlorophyll molecules, although in a smaller extend for PS II.

3.1.3 β -Carotene in photosynthesis

β -Carotene serves different purposes within the two photosystems. The most obvious is of course its capability to harvest light *via* its $S_0 \rightarrow S_2$ optical transition in

the blue-green spectral range, a regime where chlorophyll is not very photosensitive (see Fig. 3.7). Besides that, the molecule serves other vital functions within the PSs. The most important one is the quality of carotene to act as an antioxidant and to protect the plant against light stress.

The mentioned functions are of course strongly related to the electronic structure of the involved pigments. The electronic structure of carotenoids is similar to the electronic structure of related polyenes which can be described by a simple three-level model as depicted in the left hand side of Fig. 3.8. Transitions to higher energy singlet states are possible, but play no decisive role for the photochemistry of carotenoids described in this work and are therefore neglected (e.g. the $1^1A_g \rightarrow 2^1B_u$ transition of β -carotene is located at around 260 nm and visible in the absorption spectrum shown in Fig. 3.8(b)).

The ground state of β -carotene is denoted S_0 while the next two electronic levels are labeled S_1 and S_2 . The terms A_g^- and B_u^+ are the symmetry representations of the states in the idealized C_{2h} point group. Transitions between two states having the same symmetry are forbidden, which means that the $S_0 \rightarrow S_1$ transition is symmetry forbidden. The allowed $S_0 \rightarrow S_2$ transition is responsible for the light absorption of the molecule in the blue-green regime as shown in Fig. 3.8(b) [44, 45].

Next to the electronic states of β -carotene Fig. 3.8 also shows the states of chlorophyll (Chl). β -Carotene possesses excited singlet states higher in energy than the corresponding Chl states. This enables the light harvesting function of carotene since the

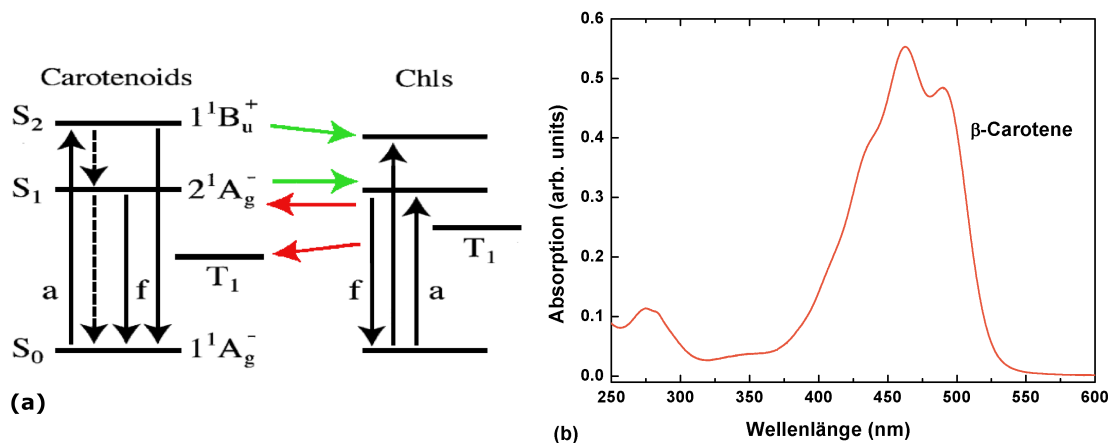


Figure 3.8: (a) Low-lying energy states of carotenoids and chlorophyll (Chls) and the various photochemical processes that can occur between them. The dashed lines represent nonradiative processes; a and f represent the absorption and the fluorescence, respectively. B_u and A_g are the symmetry representations of the electronic states of carotenoids in the idealized C_{2h} point group. The picture is adapted from Ref. [37].

(b) Absorption spectrum of β -carotene.

arrangement of the states allows excitation energy transfer from the carotene to the chlorophyll molecules. The triplet state of β -carotene is lower in energy with respect to chlorophyll which favors triplet-triplet energy transfer from excited chlorophyll to the carotene. This mechanism is most important with respect to photoprotection (see text below).[37].

Each photosystem contains nearly 100 pigments which absorb sunlight and transport its energy to the RCs of the two photosystem, where the charge separation takes place. Responsible for the initiation of the photosynthesis by absorption of photons are the main antenna pigments, which are primarily chlorophyll and β -carotene (see the absorption spectrum Fig. 3.7). In the course of time nature has developed a fast and efficient transfer of the absorbed photon energy between the different pigment molecules and finally to the RCs, which act as an energetic sink. Therefore, the absorption does not have to occur in close vicinity to the RC, because the plant is able to guide the energy within the protein complex. To be efficient, this pathways have to occur faster than the natural lifetime of the excited states. In the PSs this process is mediated by several intermediate carriers and two highly different energy transport mechanisms: the Förster-resonance transfer and the Dexter-transfer (see Fig. 3.9). While the latter operates only in close distances (1.5 nm), the former has a range of up to 10 nm. According to Förster, energy transfer between two pigments is mediated by nonradiative dipole-dipole interaction. This process is enabled by the high transition dipole moment of the involved chromophores due to the extensive nature of their conjugated double-bond systems. The transfer rate of the Förster, energy transfer shows the following distance dependence:

$$k_{Forster} \propto \frac{\kappa^2}{r^6 n^4} \frac{\Phi_D}{\tau_D} \int_0^\infty \lambda^4 \epsilon_A(\lambda) F_D(\lambda) d\lambda = k_{rad} R_0^6 \frac{1}{r^6} \quad (3.1)$$

In equation 3.1 λ denotes the wavelength, r the distance of the involved electronic states and κ^2 is a geometry parameter, which reflects their orientation relative to each other. n is the refractive index of the surrounding medium, Φ_D denotes the fluorescence quantum yield of the donor, τ_D is the fluorescence-lifetime, ϵ_A is the extinction coefficient of the acceptor and F_D and k_{rad} are the normalized radiant intensity and the emission rate of the donor, respectively. The integral represents the convolution of the fluorescence spectrum of the donor and the absorption spectrum of the acceptor. The larger the integral the larger the transfer rate. The integral and the constants are summarized in R_0 (Försterradius), which is the distance with a 50 % probability for an energy transfer. For an assumed huge overlap R_0 can have values up to 100 Å, usual distances between pigments molecules like chlorophyll a in the photosystems are well within this area (8-16 Å). Simulations of the kinetics of

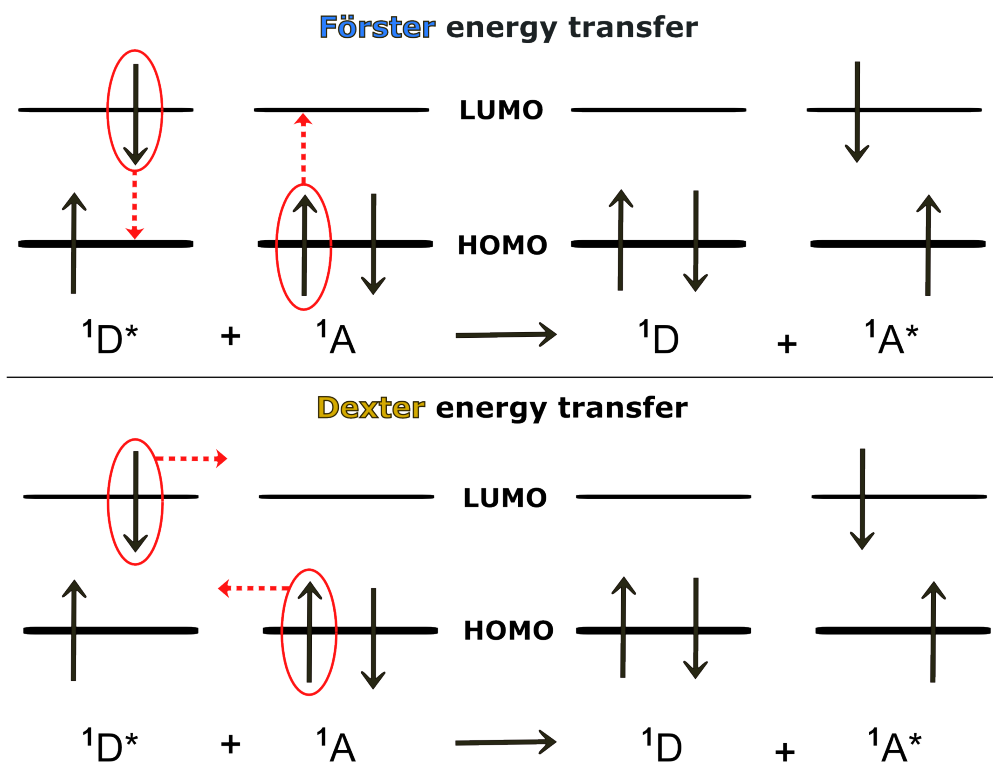
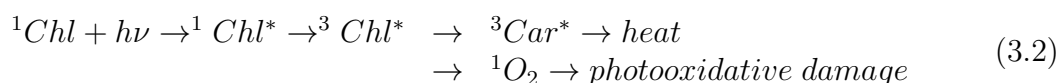


Figure 3.9: Schematic diagrams of the Förster and Dexter energy transfer. HOMO and LUMO denotes the highest occupied molecular orbital and the lowest unoccupied molecular orbital, respectively.

PS I and related antenna complexes reveal, that a multi-step Förster energy transfer chain describes the global kinetics of these photoactive system very well[46].

An exception is the energy transfer from carotenoids to chlorophylls, which is not suited for the Förster transfer because the S_1 -state lifetime of carotenes is just 10 ps (the usual lifetime of an excited chlorophyll is between 2-4 ns). This process, which has a protective component within the photosynthetic organism, is better described by the Dexter-transfer. The Dexter-transfer is based on the direct overlap and interaction of the wave functions from donor and acceptor. It is therefore highly sensitive to the distance of the partners and works typically in the distances of <2 nm. The transfer rate $k_{Dexter} \propto e^{-\alpha r}$ decreases exponentially with the distance r , α is referred to as the Dextercoefficient and reflects the resonance condition between donor and acceptor. Dextertransfer occurs very fast, down to a few fs, and it includes, in contrast to the Förstertransfer, electron transfer between the pigments. The Dextertransfer is the dominating process for triplet quenching, which is also reflected in the small distance most carotene molecules posses with respect to chlorophyll.

If a plant receives too much light it obviously cannot respond by hiding. It has though some biochemical possibilities to deal with excess light [47–50], but undiminished high light intensities will lead to a over-reduction of the primary electron acceptors in the photosystems and free radicals and reactive oxygen species like singlet oxygen are built. This radicals and reactive species can be efficiently and rapidly quenched by β -carotene molecules in the proteins *via* Dexter-transfer from the excited chlorophyll to a neighbored β -carotene. If not quenched by carotenes, the excess energy would be quenched by oxygen, which would lead to the formation of highly reactive and toxic singlet oxygen (1O_2)[50, 51]:



This process is called valve-reaction and requires the involved molecules to be in near van-der-Waals distance (3.6 Å) to each other[51, 52]. This is the case for all carotene molecules in the PSs despite the three molecules found in the RC of the PS II. They show, due to the large distance to their next neighbor, a low-efficiency singlet-singlet energy transfer (20-25 %) and also no 3Chl quenching [53, 54]. If bound more closely to the P680, the carotenes would be rapidly oxidised (ns-timescale) by the light-induced production of $P680^+$ due to the high potential of $\geq 1.1V$ of the $P680^+/P680$ [55]. This oxidization would out-compete the designated electron transfer from the manganese complex to the $P680^+$. This problem is unique for the PS2 RC because the redox potentials of other primary electron donors are less oxidizing[37]. Although these three carotene molecules are not able to quench the chlorophyll triplet states directly they can quench the formed singlet oxygen itself[56]. Due to the distance of the carotenes to the P680, this process occurs on a ms-timescale. It can only afford partial protection and decrease the extent of damage from this species, which is in line with the observed higher light-stress sensitivity of the PS II with respect to PS I[57].

Chapter 4

The ν_1 -anomaly of β -carotene

Raman measurements on β -carotene date back to 1958, the first detailed vibrational study of the molecule, however, stems from Inagaki and co-workers in 1974[58]. They excited the molecule with several laser lines in the absorption regime of the molecule. Raman excitation profiles (REPs) of the most intense Raman bands were presented and their behavior was explained solely by A-term enhancement. Nine years later Saito et al. assigned all detectable Raman bands in between 40 and 5800 cm^{-1} on the basis of the results of a normal-coordinate analysis. The authors also showed that the cis-isomer of β -carotene can be easily distinguished by the appearance of distinct modes for the certain isomer[59]. Koyama et al. generalized this approach for a bigger number of carotene isomers[60]. The first analysis of the vibrational spectroscopic characteristics of β -carotene by means of DFT calculations stems from Schlücker et al.[61].

In this chapter, experimental and calculated Raman spectra of β -carotene are presented and compared. In particular, the behavior of the ν_1 -band is analyzed supported by density functional theory (DFT) calculations.

This band is of particular interest in photosynthetic research since it shows small vibrational frequency shifts upon varying the excitation line for the RC of the PS II[62]. These shifts could reflect the perpendicular arrangement of the carotene molecules in the RC of the photosystem and their slightly different $S_0 \rightarrow S_2$ transition energies due to subtle changes in the protein-chromophore interactions[63].

This chapter is divided into three sections. In the first section the Raman spectrum of β -carotene is introduced while in the second the ν_1 -anomaly is discussed. In the third section the results of the previous sections are compared to the situation within the photoactive proteins PS I and II.

4.1 The Raman spectrum of β -carotene

A typical Raman spectrum of β -carotene is shown in Fig 4.1. To obtain the spectrum all-trans β -carotene (purity $\leq 97\%$) was purchased from Fluka and used without further purification. The β -carotene was dissolved in dichloromethane (DCM) and had a concentration of $73 \mu\text{M}$. The three most prominent bands in the Raman spectra are named ν_1, ν_2 and ν_3 and are located at around $1524, 1157$ and 1005 cm^{-1} , respectively. These bands were attributed in the past to vibrations originating from a double bond C=C stretching mode (1524 cm^{-1}), a C-C single bond stretching mode (1157 cm^{-1}), and a C-H in-plane bending mode (1008 cm^{-1})[58].

To attribute all detectable modes to their originating vibrational pattern DFT calculations were performed by Matthias Schenderlein¹. The calculations were performed with the program packages GAUSSIAN03 and TURBOMOLE[64, 65].

For the geometry optimization of the ground-state structure of β -carotene, the coor-

¹Present affiliation: Max Planck Institute of Colloids and Interfaces, Potsdam

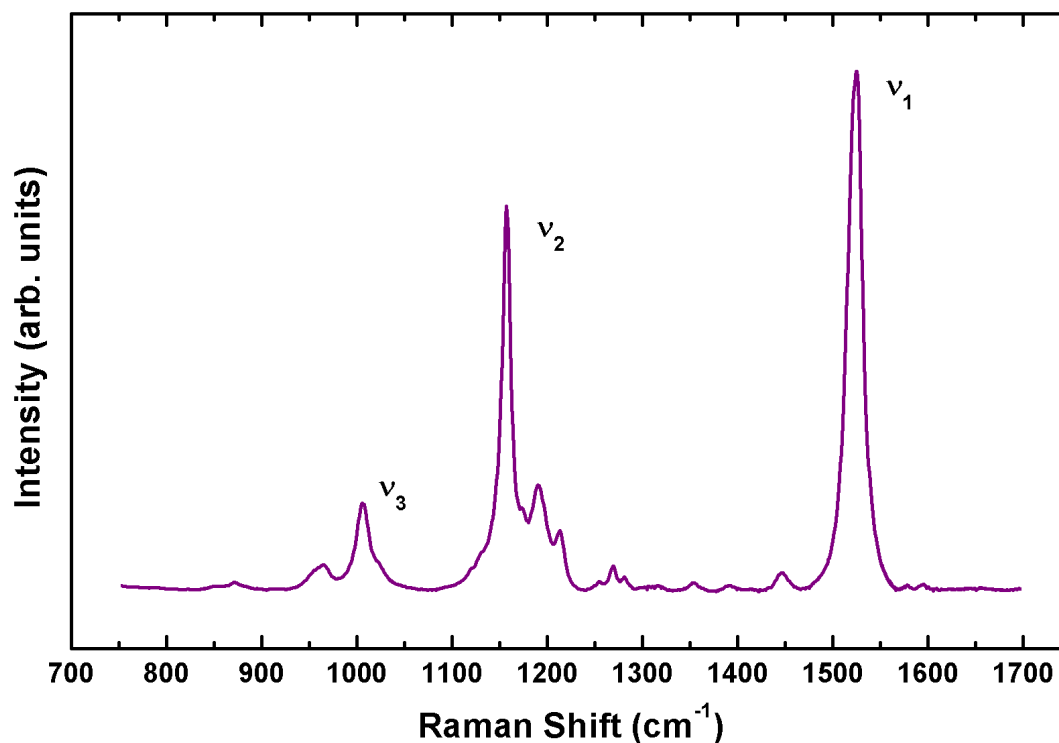


Figure 4.1: Raman spectrum of β -carotene obtained at 442 nm. The three most prominent vibrational bands are indicated.

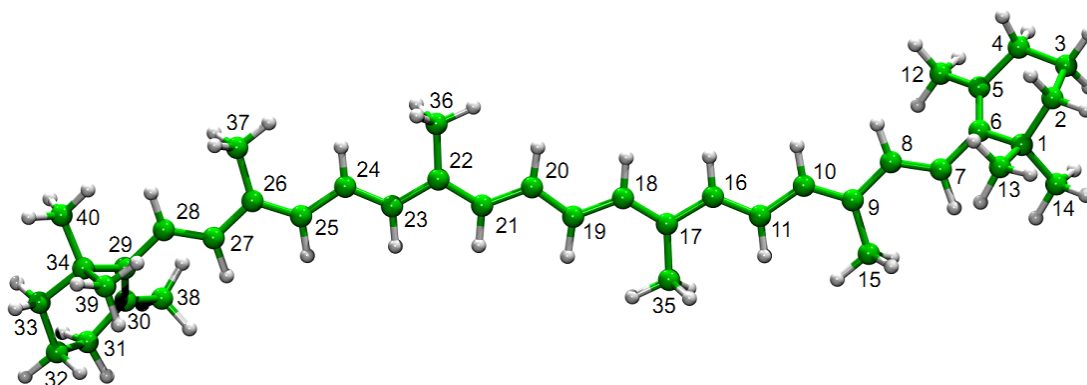


Figure 4.2: Optimized chemical structure of β -carotene in the ground state derived from DFT calculations. The carbon atoms are numbered. The picture is courtesy of Matthias Schenderlein.

dinates of the chromophore in the *all-trans* configuration extracted from the crystal structure of PS II served as a starting point[31]. The geometries and force fields were determined by DFT using the 6-31G* basis set and the three-parameter hybrid exchange functional B3LYP[66, 67].² To minimize systematic errors and to improve the accuracy of the calculations, the force constants were scaled with a set of global scaling factors optimized for certain types of vibrations[68, 69]. The resulting minimum-energy structure of the molecule is seen in Fig. 4.2. It shows no symmetry, albeit if one only considers the backbone without the beta-ionone rings it exhibits in good approximation a C_{2h} symmetry.

The root-mean-square (rms) deviations of the calculated bond lengths and bond angles with respect to experimental data stemming from X-ray diffraction data are 0.012 Å and 0.9°, respectively[70]. These deviations are slightly smaller than those from Requena *et al.*[71], who employed the same functional and basis set.

The Raman intensities were calculated numerically by means of the finite electric field method. To increase the accuracy of the intensity calculations, the derivatives of polarizability with respect to the normal modes were computed using a 4th order differentiation algorithm that effectively minimizes the errors associated with numerical differentiation[68].

It should be noted, that in a second approach full C_{2h} symmetry was imposed on

²The notation 6-31G* of the basis set denotes, that the inner atom orbitals are represented by a linear combination of six Gaussian functions, while the valence bands are described with two sets of basic functions, the first using three and the second using one Gaussian functions. The asterisk denotes the usage of additional six d-type Gaussian polarization basic functions to reflect the strong polar behavior of the molecule. The B3LYP functional includes the correlation energy of the electrons to the resulting electron density.

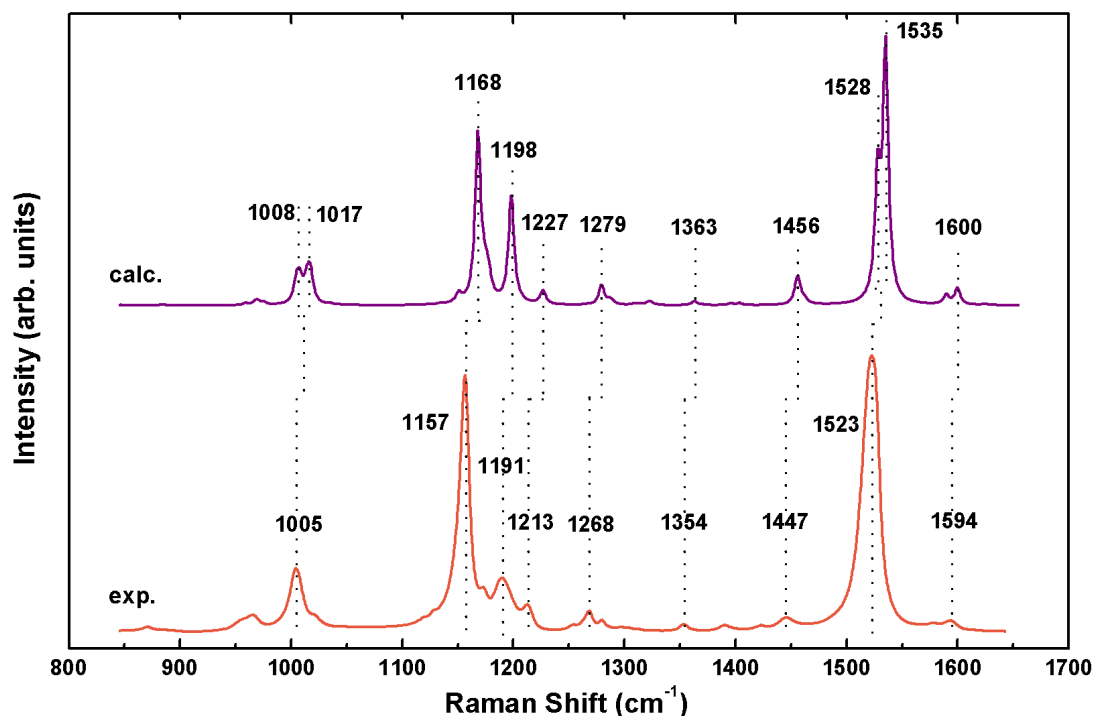


Figure 4.3: Experimental and calculated Raman spectra of β -carotene. For the former the β -carotene was dissolved in DCM and excited at 590 nm. The calculated spectrum is for the non-resonant case. The assignment of the strongest modes are indicated. The peaks in the calculated spectrum are upshifted with respect to the experimental peaks up to 14 cm^{-1} .

the β -carotene molecule. To do so, the rings had to be forced into a planar configuration in order to achieve full C_{2h} symmetry. The resulting structure possesses a *ca.* 139 kJmol^{-1} higher potential minimum energy and leads finally to a worse description of the experimental spectrum.

The calculations result in 282 vibrational frequencies of the molecule, 43 of them with reasonable Raman intensity (see Table 4.1). Although there is no strict rule of mutual exclusion due to the low symmetry of the molecule, most of the modes display according to the calculations either Raman or IR activity, implying that the underlying geometry is close to C_i . Figure 4.3 shows both, a calculated and an experimental Raman spectrum of β -carotene. The calculated Raman spectrum is quite simple, it agrees very well with the experimental spectrum that is obtained with 590 nm excitation and thus relatively far away from the first allowed electronic transition at *ca.* 490 nm. Most of the bands are reproduced by calculations with

4.1 The Raman spectrum of β -carotene

an average deviation of *ca.* ± 10 cm^{-1} . Similarly, the calculated Raman intensities agree well with the experimental values except for an overestimation of the mode at 1198 cm^{-1} (calc.) as compared to the experimental band at 1191 cm^{-1} . Even the shoulders and partly asymmetric band shapes of individual peaks in the experimental Raman spectrum such as at 1005 and 1157 cm^{-1} can be rationalized taking into account overlapping contributions of closely spaced Raman-active modes.

In the region between 1650 and 750 cm^{-1} the Raman active modes can be grossly classified in five groups according to frequency and normal compositions (Table 4.1). Between 1500 and 1650 cm^{-1} , the C=C stretchings of the polyene chain provide the main contributions to the modes, among them the mode ν_{66} , which exhibits the

Calculation		Experiment			
Mode No.	PED	ν/cm^{-1}	I_{Ra}	ν/cm^{-1}	I_{Ra}
ν_{59}	C=C str (6, 5) <i>11.2</i>	1625	0.5	1615	0.1
ν_{62}	C=C str (8, 7) <i>13.8</i> ; (28,27) <i>14.2</i>	1600	6.9	1594	9.3
ν_{63}	C=C str (10, 9) <i>18.8</i> ; (26,25) <i>18.4</i>	1589	3.9	1579	7.5
ν_{66}	C=C str (16,11) <i>11.6</i> ; (20,19) <i>20.3</i> ; (24,23) <i>11.7</i>	1535	100	1526	100
ν_{67}	C=C str (18,17) <i>22.4</i> ; (22,21) <i>22.9</i>	1527	47.3	1519	25.8
ν_{79}	Asym methyl def. (37) <i>55.9</i>	1462	1.4		
ν_{84}	Asym methyl def. (35) <i>29.7</i> ; (36) <i>29.2</i>	1456	9.3		9.6
ν_{86}	Asym methyl def. (38) <i>78.7</i>	1455	1.0	1447	
ν_{87}	Asym methyl def. (12) <i>85.9</i>	1454	1.0		
ν_{95}	C-H rock (25) <i>11.4</i>	1403	0.9	1392	2.4
ν_{97}	Sym methyl def. (36) <i>17.2</i> ; (37) <i>15.4</i>	1395	0.7		
ν_{109}	C-H rock (21) <i>10.6</i> ; sym methyl def. (35) <i>15.1</i> ; (36) <i>16.5</i>	1363	1.5	1354	2.6
ν_{116}	C=C str (28,27) <i>12.8</i> ; C-H rock (28) <i>41.4</i>	1323	1.2	1301	3.2
ν_{117}	C-H rock (7) <i>40.1</i>	1321	0.8		
ν_{119}	C=C str (20,19) <i>11.6</i>	1314	0.5		
ν_{120}	C=C str (24,23) <i>8.9</i> ; C-H rock (27) <i>9.7</i>	1308	0.5		
ν_{122}	ring methylene twist (31) <i>17.7</i> ; (33) <i>32.5</i>	1288	1.7	1281	2.1
ν_{123}	ring methylene twist (2) <i>31.2</i> ; (4) <i>19.4</i>	1286	0.5		
ν_{124}	C-H rock (11) <i>17.6</i> ; (24) <i>18.1</i>	1279	8.1	1268	6.7
ν_{127}	C-H rock (7) <i>13.5</i> ; (8) <i>11.2</i>	1265	0.1	1254	1.5
ν_{128}	C-C str (17,16) <i>6.5</i> ; C=C str (20,19) <i>8.7</i>	1227	5.6	1213	7.2
ν_{135}	C-C str (27,26) <i>8.4</i>	1198	42.7	1191	44.7
ν_{137}	C-C str (31,30) <i>14.0</i> ; (38,30) <i>18.4</i>	1180	0.3		2.8
ν_{139}	Methyl rock (39) <i>11.0</i>	1177	9.3	1174	
ν_{140}	Methyl rock (14) <i>12.6</i>	1173	7.7		
ν_{141}	C-C str (11,10) <i>12.2</i> ; (19,18) <i>13.9</i> ; (21,20) <i>13.9</i> ; (25,24) <i>11.3</i>	1168	66.7	1157	86.8
ν_{143}	C-C str (21,20) <i>8.5</i>	1151	3.7	1150	32
ν_{144}	Ring methylene twist (4) <i>13.7</i>	1135	0.2	1136	5
ν_{145}	Ring methylene twist (31) <i>14.8</i>	1134	0.1		
ν_{156}	Methyl rock (15) <i>25.8</i> ; (35) <i>16.3</i> ; (37) <i>10.4</i>	1035	0.35	1022	3.6
ν_{158}	Methyl rock (12) <i>15.3</i> ; (13) <i>10.0</i> ; (35) <i>16.1</i>	1018	3.9		3.4
ν_{159}	Methyl rock (39) <i>11.9</i> ; C-C str (38,30) <i>10.9</i>	1018	3.6		
ν_{160}	Methyl rock (36) <i>17.2</i> ; (38) <i>13.6</i> ; (39) <i>11.1</i> ; (40) <i>18.7</i>	1017	5.4		
ν_{161}	Methyl rock (12) <i>14.1</i> ; (13) <i>13.3</i> ; (35) <i>14.1</i>	1014	7.0	1005	
ν_{162}	Methyl rock (36) <i>15.1</i> ; (37) <i>14.9</i>	1008	7.2		
ν_{163}	Methyl rock (15) <i>11.8</i>	1007	6.7		
ν_{164}	C-H out-of-plane (8) <i>16.5</i> ; torsion (8-7) <i>10.8</i>	1001	3.7		
ν_{167}	Methyl rock (14) <i>11.9</i>	992	1.0		
ν_{170}	C-H out-of-plane (23) <i>10.5</i> ; torsion (24-23) <i>12.0</i>	982	0.6		
ν_{171}	C-C str (33,32) <i>10.4</i> ; ring methylene rock (32) <i>12.7</i> ; methyl rock (38) <i>14.7</i>	974	0.4	967	5.9
ν_{172}	Ring methylene rock (3) <i>18.3</i> ; methyl rock (12) <i>15.0</i>	968	0.3	957	3.3

Table 4.1: Experimental and calculated frequencies and intensities of the Raman active modes of β -carotene.

Abbreviations: asym, asymmetric; def, deformation; I_{Ra} , relative Raman intensity with respect to the strongest Raman mode (ν_{66}); PED, potential energy distribution, values (in %) are given in italics (C atoms involved are indicated in parentheses); rock, rocking; str, stretching; sym, symmetric; twist, twisting. See Fig. 4.2 for atom numbering.

strongest Raman intensity of all modes. This mode, combined with the ν_{67} , gives rise to the ν_1 -band in the experimental spectra. Between 1500 and 1400 cm^{-1} , the modes mainly involve methyl deformations and only a few of them exhibit appreciable Raman intensity, leading to a composite peak at 1456 cm^{-1} (mainly ν_{84}). The C-H rocking is the internal coordinate that dominates the modes between 1400 and 1250 cm^{-1} leading to an asymmetric peak at 1279 cm^{-1} (ν_{124}). Below this region (1250-1150 cm^{-1}), the modes mainly involve C-C stretching coordinates with the most prominent modes ν_{135} (1198 cm^{-1}) and ν_{141} (1168 cm^{-1}), from which the latter is the main contribution of the experimental ν_2 -band. Finally, the methyl rocking prevails between 1050 and 990 cm^{-1} . Below 800 cm^{-1} , no Raman-active modes are predicted with intensities more than 1.5% as compared to ν_{66} , which is in very good agreement with the experimental spectrum.

4.2 The ν_1 -band of β -carotene

In general, resonance Raman spectra of β -carotene obtained in solution with excitation lines around the first allowed electronic transition (450 - 530 nm; see Fig. 3.8(b))

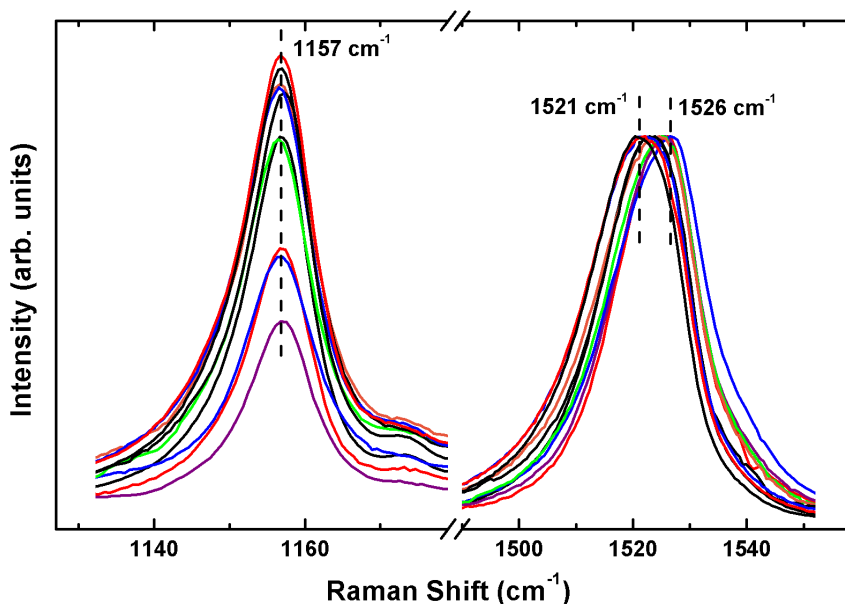


Figure 4.4: Raman spectra of the ν_1 - and ν_2 -region of β -carotene normalized to the ν_1 -band intensity excited at various excitation wavelengths. While the ν_2 -band position is independent of the laser energy, the ν_1 -band position does show a dependency.

on page 25) show vibrational bands identical to Raman spectra obtained under non-resonant conditions (590 nm; Fig. 4.3). All bands that are observed in the Raman spectrum are also enhanced under resonant excitation conditions. A closer inspection of the prominent band at 1525 cm^{-1} , however, reveals small but clearly detectable shifts of the peak maximum with the excitation wavelengths.

Figure 4.4 shows the ν_1 - and ν_2 -region of dissolved all-trans β -carotene excited at different wavelengths ranging from 442 nm to 647 nm. The intensities are normalized to the ν_1 -band. The band position shows a reproducible dependence on the excitation wavelength varying for example from 1521 cm^{-1} at 514 nm excitation to 1526 cm^{-1} at 476 nm excitation (see Fig. 4.5 A). Conformational heterogeneity can be ruled out as a possible explanation for this shift, since no other peaks in the experimental spectrum provide any indication for conjugate bands that are not attributable to modes of the fully relaxed β -carotene structure[60].

Next to the shifting of the ν_1 -mode the relative intensities between the two modes ν_1 and ν_2 also show a curious excitation dependent variation. Fig. 4.5 B shows the intensity ratios of the ν_2 -band with respect to the ν_1 and the ν_3 mode. The choice of ν_3 is arbitrary and was done due to its relatively high intensity. Choosing a reference band other than the ν_2 leads to similar results. The ν_3/ν_2 -ratio shows only a

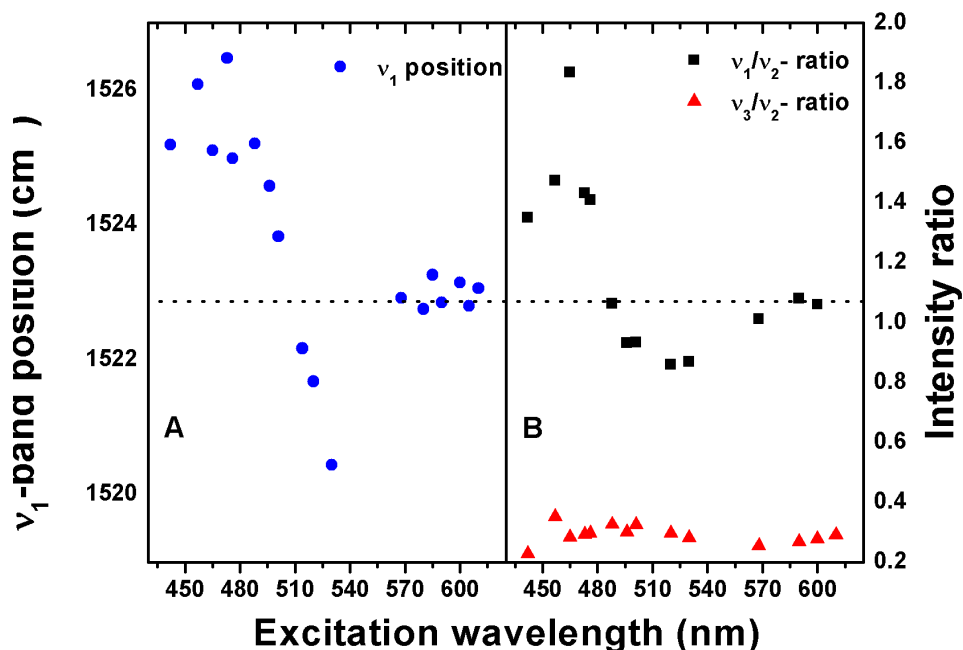


Figure 4.5: (A) Excitation dependent band position of the ν_1 -band and (B) the intensity ratios ν_1/ν_2 and ν_3/ν_2 . The nonresonant ratio is indicated by the dashed horizontal line.

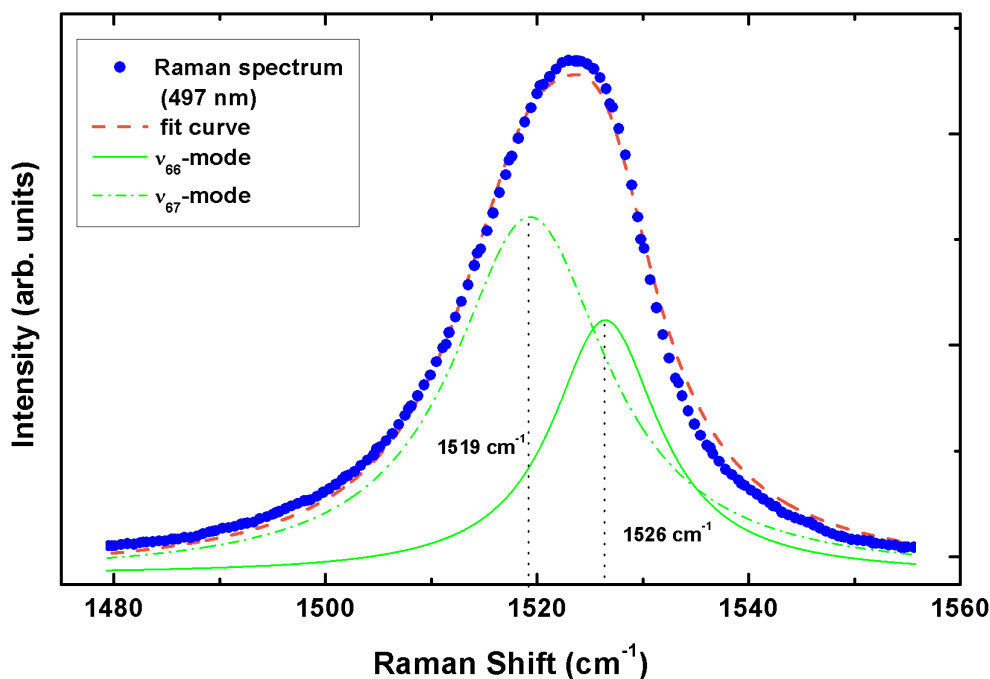


Figure 4.6: Experimental and fitted spectra shown for 497 nm excitation. The position of the underlying ν_{66} - and ν_{67} -mode are shown.

weak energy dependence throughout the wavelength region studied, below 500 nm it tends to decrease. The ν_1/ν_2 ratio on the other hand exhibits a clear energy dependence. In the region between 480 nm and 520 nm the ν_2 -band is larger than the ν_1 -band in contrast to the non-resonant case (excitation wavelength ≥ 550 nm) with a ratio of approximately 1.15. For excitation below 475 nm the curve shows a strong gain with a maximum of 1.65 at 465 nm.

Since the DFT calculations of the Raman spectrum of β -carotene predict two closely spaced modes in the region of the ν_1 -band at 1528 and 1535 cm^{-1} (ν_{66} and ν_{67} , respectively) it seems reasonable to assume that these submodes are involved in the ongoing processes. The ν_{66} -mode at 1535 cm^{-1} exhibits twice the intensity of the ν_{67} -mode at 1528 cm^{-1} . Both modes originate from double bond C=C stretching of the polyene chain, although different C=C stretching coordinates are involved (see Table 4.1). A global analysis to the experimental peak at around 1524 cm^{-1} for all excitation wavelengths was applied to yield the experimental positions of the two modes. The band was fitted using two Lorentzian functions and their position and bandwidth were iteratively adjusted to yield an optimum agreement with the experimental data. Figure 4.6 shows an example fit for an excitation at 497 nm.

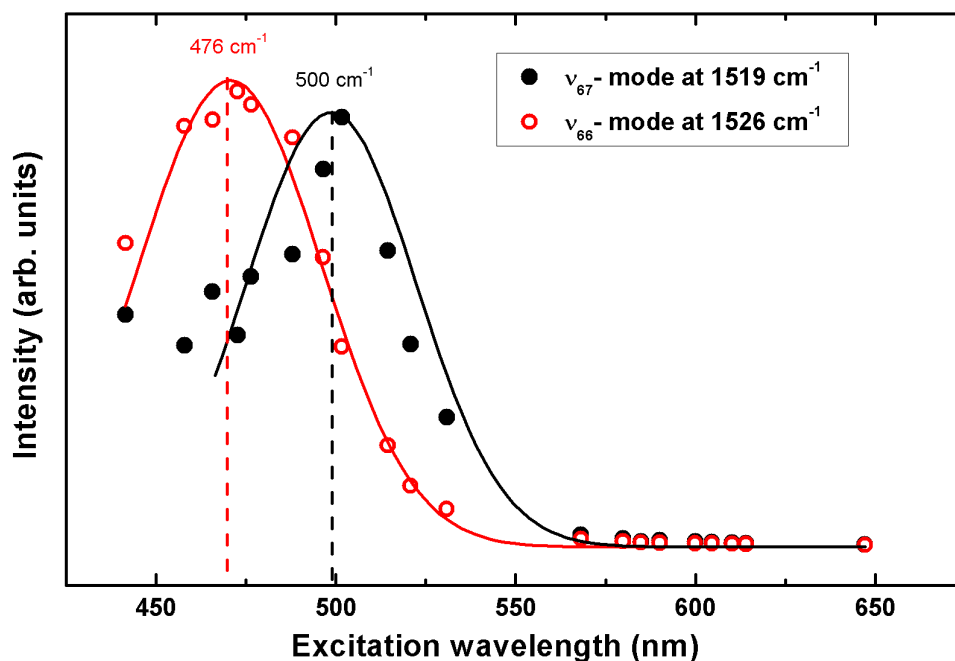


Figure 4.7: Raman excitation profiles (REP) of the ν_{66} - and ν_{67} -mode.

The analysis results in overall experimental peak positions at 1519 cm^{-1} and at 1525 cm^{-1} for the underlying modes ν_{67} and ν_{66} . These findings are in good agreement with the predicted calculated spectra.

In the next step, the Raman excitation profiles (REPs) of the submodes were created to examine their resonance wavelength. Raman excitation profiles are constructed by normalizing all measured Raman spectra to a distinct feature in the spectra which does not originate from the sample itself and which is not in resonance in the measured excitation regime. This is necessary to avoid misadjustments in the intensity and was achieved with marker bands originating from the used solvent. For dissolved β -carotene, the 1423 cm^{-1} of dichloromethane was used as internal standard. The Raman excitation profile is finally done by plotting the measured intensity against the excitation energy. Fig. 4.7 shows the REPs for both submodes, the lines are just guide to the eyes: the profile of the ν_{67} -mode at 1519 cm^{-1} shows a clear intensity gain from 525 to 500 nm compared to the ν_{66} -band excitation profile, which exhibits a maximum at around 475 nm. Due to the stronger contribution of the ν_{67} -mode between 525 and 500 nm the ν_1 -band seems to shift to lower wavenumbers, whereas in the region around 488 nm excitation the apparent upshift is readily attributable to the stronger contribution of the ν_{66} -band. The analysis does not reveal the reason for the odd ν_1/ν_2 -intensity ratio, but comparing Fig. 4.5 and 4.7 shows that this

effect has to be related solely to the ν_{66} -mode.

Like in the non-resonant case calculations were run to enlighten possible origins of the nonconform behavior of the two submodes. To calculate these resonant-Raman spectra, knowledge about the structure of the molecule in the excited state is necessary. The geometry of the electronically excited state has been optimized using time-dependent DFT calculations (TDDFT) within the TURBOMOLE package. The same functional and basis set as for the ground state calculations were used. For the calculation of the resonance Raman intensities the approach developed by Rush and Peticolas was used[72, 73], which originally was developed by Hizhnyakov and Tehver[74]. The underlying approximations of this approach include the assumption of A-term scattering only and harmonic surface potentials of the ground- and excited state. Frequency shifts upon excitation as well as non-Condon effects like the Dushinsky rotation have been neglected. Following these assumptions and considering only vibrational transitions from the ground state, the resonance Raman intensity I_k of the k th vibrational mode Ω_k by an excitation with the frequency ω is in the used framework given by

$$I_k(\omega) = \frac{\Delta_s^2 K M_{GR}^4}{2} |(\Phi(\omega) - \Phi(\omega - \Omega_k))|^2 \quad (4.1)$$

where M_{GR} denotes the electronic transition moment and K is an frequency dependent factor:

$$K = \omega(\omega - \Omega_k)^3 \left(\frac{\sqrt{\Omega_k}}{5.8065}\right)^2. \quad (4.2)$$

The quantity $|(\Phi(\omega) - \Phi(\omega - \Omega_k))|^2$ can be calculated by using an experimental obtained UV/VIS-absorption spectrum and its corresponding Kramers-Kronig transform

[74]. Δ_s is the excited state displacement and reflects the differences of the equilibrium values of the internal coordinates in ground and excited state:

$$\Delta_s = \sum_i^{3N-6} L_{ki}^{-1} \Delta R_i \quad (4.3)$$

ΔR_i are the differences of the i th internal coordinates between the two states and L_{ki}^{-1} represents the inverse of the transformation matrix between internal and normal coordinates. In the absence of any symmetry-based selection rules, as in case of the fully relaxed β -carotene geometry, the relative enhancement of individual modes is solely controlled by the excited state displacements Δ_s [72].

The largest calculated Δ_s values are noted for the C=C and C-C stretching coordinates which, upon transition to the electronically excited state, reveal slight elongations and contractions of the C=C and C-C bonds, respectively. Upon transition

from the S_0 to the S_2 state, the double bond length of these coordinates increases by about 0.025 Å to an average value of 1.401 Å. Concomitantly, the lengths of the adjacent single bonds decrease by about the same amount leading to nearly the same average bond length (1.411 Å) such that single and double bonds of the polyene chain become very similar.

The calculated resonance Raman spectra reproduce the observations that the Raman-active modes are in general enhanced upon excitation in resonance with the $S_0 \rightarrow S_2$ transition. The calculations qualitatively also confirm the increase of the intensity ratio of the modes ν_{66} and ν_{141} from non-resonant to rigorous resonance conditions as shown in Fig. 4.8. Please note that the ν_{141} is the calculated equivalent of the ν_2 mode which was used as a reference band for the experimental data in Fig. 4.5 on page 35. The ν_{66}/ν_{141} -ratio is shown in Fig. 4.8 A, which additionally shows the calculated ν_3/ν_{141} -ratio for the resonant case and the values for the non-resonant excitation. The ν_3 -values of the calculated spectra were obtained by fitting the band in all spectra with a Lorentzian function. This was necessary since in the region of the ν_3 -band several calculated modes with reasonable intensity are located (the modes $\nu_{156} - \nu_{164}$ in Table 4.1). The experimental values are shown in

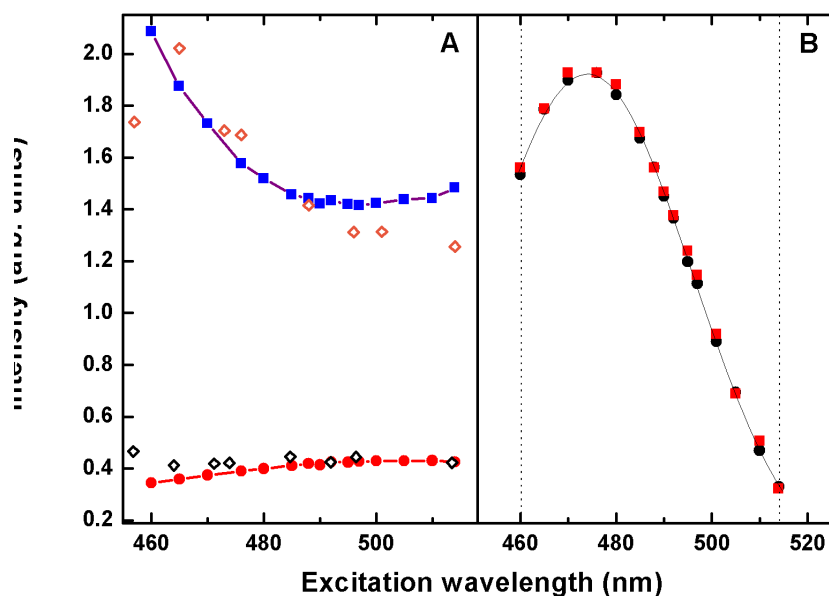


Figure 4.8: (A) Calculated ν_{66}/ν_{141} (blue line and symbol) and ν_3/ν_{141} -intensity ratios (red line and symbol). The diamonds represent the experimental results, albeit adapted in y-position to reflect the similarities of the results. (B) REPs of the calculated modes ν_{66} (red squares) and ν_{67} (black circles). The dotted line represent the range of the calculations.

open orange and black diamonds for the ν_1/ν_2 - and ν_3/ν_2 -ratio, respectively. Please note, that the total values for the experimental data are adapted along the y-axis to adjust the impreciseness of the calculated data. The behavior of both ratios, the strong increase of the ν_1/ν_2 -ratio and the slight decrease of the ν_3/ν_2 -ratio are qualitatively reflected by the calculations.

However, despite this agreement the different REPs for the modes ν_{66} and ν_{67} cannot be understood on the basis of the calculations, as shown in Fig. 4.8 B. Their respective Δ_s values are quite similar leading to identical calculated REPs of the modes ν_{66} and ν_{67} in contradiction to the experiment.

This discrepancy has to be attributed to effects not accounted for in the calculations. Since the theoretical approach only accounts for A-term enhancement, Herzberg-Teller scattering enhancement by vibronic coupling with a second near-by electronic state is a possibility, but there is no electronic transition of appropriate symmetry in sufficiently close energetic proximity that might be vibronically coupled to the $S_0 \rightarrow S_2$ transition.

Another approach considers resonance enhancement of IR-active A_u modes via vibronic coupling with an electronic transition of appropriate symmetry. However, no A_u modes are observed in the IR spectrum[61] that would account for the experimental resonance Raman band at 1519 cm^{-1} (ν_{67}).

Finally, one may consider the Dushinsky rotation, the effect of normal mode changes upon electronic excitation, which cannot be considered by the present calculations. The main contributions ($>10\%$ PED) to the modes ν_{66} and ν_{67} are provided by the C=C stretchings of the polyene chain albeit with an alternating pattern, i.e. C(11)=C(16), C(19)=C(20), and C(23)=C(24) for ν_{66} and C(17)=C(18) and C(21)=C(22) for ν_{67} (see Table 4.1 and Fig. 4.2). Consequently, it may be possible that C-C stretching modes (i.e., ν_{141}) mix with the modes ν_{66} and ν_{67} in the excited state (Dushinsky rotation)[75]. In analogy to a work on the protein transferrin [76, 77], this hypothesis derives further support from the experimental excitation profiles of the C=C stretching modes ν_{66} and ν_{67} . Their maxima are separated by ca. 1300 cm^{-1} , which is a value lying in the range of C-C stretching frequencies, pointing to a mixing of the C=C and C-C stretchings in the excited state.

In the last sections the Raman spectrum of β carotene was introduced by experiment and theory. All appearing vibrational modes were assigned and a wavelength-dependent shift of the ν_1 -band was presented. Since this shift could not be reproduced by time-dependent DFT calculations ruling out A- and B-Term scattering as an origin for the shifting the shifting is attributed to the Dushinsky rotation effect.

4.3 Resonance Raman spectra of β -carotene in photosystems I and II

In this section the properties of dissolved β -carotene is compared with those obtained for β -carotene molecules embedded in a protein environment like in PS I and PS II. To probe the resonance Raman spectra of β -carotene in PS I and PS II, excitation was restricted to the range from 465 to 568 nm due to the increasing interference by chlorophyll fluorescence in the red and near infrared spectral region. Active PS I and II complexes from the cyanobacterium *T. elongatus* were purified as describes elsewhere [78, 79]. For the measurements the proteins were diluted by a buffer containing 20 mM 2-(N-morpholino)ethanesulfonic acid (pH 6.5), 10 mg MgCl_2 , 20 mM CaCl_2 , 0.02 % (w/v) β -DM and glycerol 50% (v/v) to a final protein concentration of 2 μM . The samples were provided by Prof. Dr. Athina Zouni³ Fig. 4.9 shows several Raman spectra for the PS I and II. The spectra in Fig. 4.9 are very similar to those of β -carotene in solution. Comparing the spectra showing β -carotene in solution and in the photosystems reveals that the different environment leaves the Raman spectrum nearly unaffected. For an excitation energy of 442 nm several bands originating from chlorophyll become detectable due to the absorption of photons by the chromophores Soret-band. Figure 4.9 shows that this effect is stronger pronounced for the PS 1, which reflects the higher amount of chlorophyll with respect to β -carotene molecules within this species.

The respective ν_1/ν_2 - and ν_3/ν_2 -intensity ratios for PS I and II are shown in Figure 4.11. Both photosystems exhibit qualitatively the same wavelength dependence like β -carotene (see Fig. 4.11), with a distinct maximum of the ν_1/ν_2 -intensity ratio in the region between 470 nm and 440 nm, a negative slope between 470 to 500 nm and a ratio smaller than 1 around 500 nm. Compared to β -carotene in solution, the values of the intensity ratios of PS I and PS II are, in general, larger.

Also in the protein complexes, the frequency of the ν_1 -envelope varies with the excitation line from 1524 cm^{-1} to 1521 and 1522 cm^{-1} in PSI and PSII, respectively. Band fitting analysis reveals the two components to be located at 1520 and 1526 cm^{-1} . For the creation of the REPs of PS I and II the Raman band of glycerol at 1465 cm^{-1} was chosen as a marker band. Fig. 4.10 shows the respective REPs of β -carotene in PS I and PS II and Table 4.2 summarizes the phonon frequencies of the two submodes as well as their resonance maximum $\lambda_{REP_{max}}$. The overall shape of the REPs is similar to that of β -carotene in solution although the maxima are red-shifted by 5 and 10 nm for the ν_{66} and ν_{67} mode, respectively. It is well known, that the absorption spectrum of β -carotene is effected by its dielectric environment and these shifts are thus likely to be related to a subtle shift of the electronic $S_0 \rightarrow S_2$

³Current affiliation: Institute of Chemistry, TU Berlin

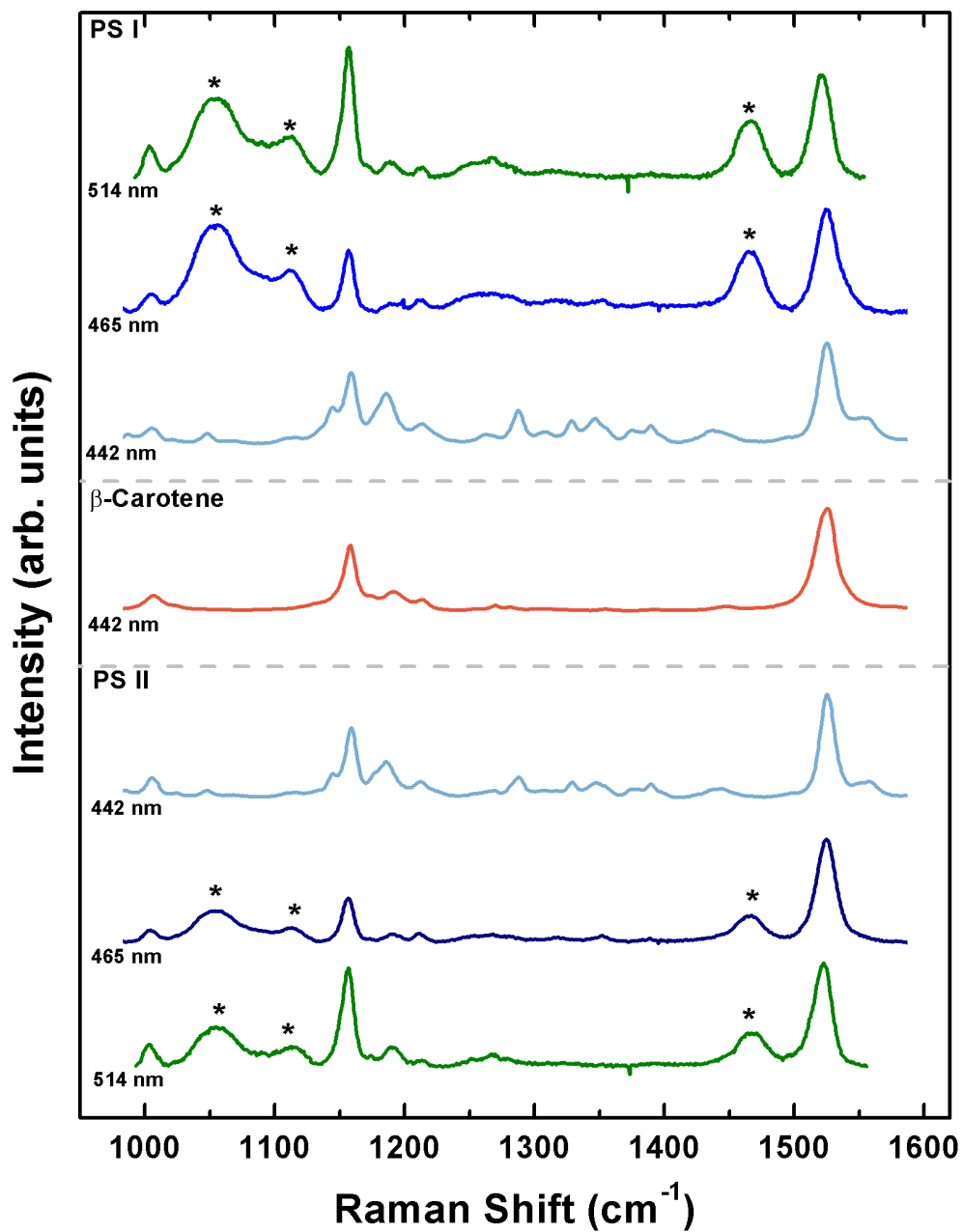


Figure 4.9: Raman spectra from PS I and II excited at 442, 465 and 514 nm. A Raman spectrum for dissolved β -carotene taken at 442 nm is additionally depicted. The asterisks denote bands stemming from the used solvent.

transition in the protein as compared to the organic solvent due to the different dielectrics of the environment[80].

It can be concluded that the excitation-dependent shift of the peak maximum of the 1525-cm^{-1} band has the same origin as for β -carotene in solution, i.e. it is an intrinsic property of this chromophore and does not reflect differences in the electrostatic interactions of the carotenes in the photosystems as suggested previously [62]. On the other hand, the present results do not per se rule out the existence of pools of spectrally distinct carotenes in PS II. Such differences, if they exist, are likely to be small and are not related to the ground state conformation of the polyene skeleton since there are, within the experimental accuracy, no noticeable differences in the frequencies of the resonance Raman modes of carotene in PSII, PSI, and in DCM solution (compare Fig. 4.3 and 4.9) as well as in other organic solvents[80]. However, the electrostatics of the chromophore environment may affect the electronic transitions and thus also the resonance enhancement of the Raman modes. This might be the origin of the differences in the REPs in the protein complexes and in solution as shown in Fig. 4.7 and 4.10. Since the REPs in the protein complexes reflect an average of all carotenes with different environments in the respective sample, the spectral heterogeneity of the carotenes in PSII or PSI cannot be resolved by the measurement of REPs.

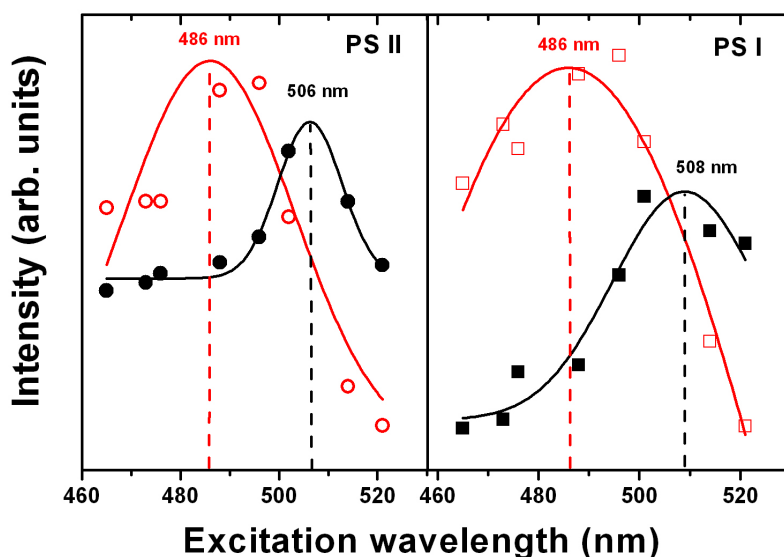


Figure 4.10: Experimental REPs from PS I and II with the black and red data points corresponding to the ν_{67} - and ν_{66} -modes at 1520 cm^{-1} and 1526 cm^{-1} , respectively (see Fig. 4.7).

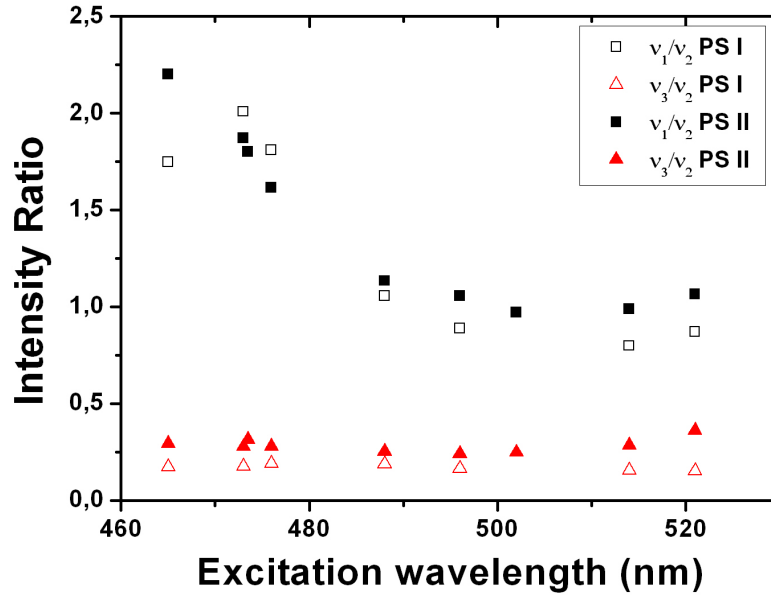


Figure 4.11: Intensity ratios of the ν_1 and ν_3 -bands compared to the ν_2 band in case of PS I and II.

	ν_{67} -mode		ν_{66} -mode	
	Position (cm^{-1})	$\lambda_{REP_{max}}$ (nm)	Position (cm^{-1})	$\lambda_{REP_{max}}$ (nm)
β -carotene	1519	500	1526	475
PS I	1520	508	1526	486
PS II	1520	506	1526	486

Table 4.2: Comparison of the the ν_{66} - and ν_{67} -modes position and $\lambda_{REP_{max}}$ determined for β -carotene in solution and embedded within photosystems I and II. $\lambda_{REP_{max}}$ refers to the maximum of the excitation profile.

Chapter 5

Carotene functionalized carbon nanotubes

Carbon nanotubes are an allotrope of carbon. They exhibit a cylindrical hollowed shape and can be seen as a rolled up graphene layer. Since their discovery in 1991 single wall carbon nanotubes (SWCNTs) have attract great interest because of their extraordinary mechanical and electronic properties [81, 82]. However, nanotube related problems like the selectivity of SWCNTs with specific chiral indices or the precise tuning of certain nanotubes properties have to be mastered [83–85].

This fine-tuning of SWCNTs properties can be achieved by chemical functionalization of SWCNTs with appropriate molecules. The most common way of functionalizing SWCNT is the covalent exohedral functionalization of the sidewall by addition reactions. These types of reactions have been performed successfully with several moieties but need to be done under extreme conditions to overcome the unreactivity of the SWCNTs[86, 87]. Nevertheless, this type of exohedral functionalization strongly affects the chemical structure of the nanotubes due to the induced defects. By quenching the optical absorption and luminescence these defects have an influence on the optical properties of the SWCNT as well.

A more gentle functionalization strategy is the encapsulation of molecules inside SWCNTs (endohedral functionalization), which leaves the chemical structure of the SWCNTs nearly unaltered [88]. Endohedral functionalization of SWCNT is well known, the incorporation of C_{60} fullerenes inside SWCNTs in 1998 was the first observed and this system has been well studied ever since [89–91].

In 2005, Yanagi *et al.* were able to incorporate *all-trans* β -carotene inside SWCNTs (Car@SWCNT) [92]. Transient ultra-fast absorption spectroscopy reveals that the optical response of SWCNTs is increased and accelerated by the encapsulation due to an excitation energy transfer from the β -carotene to the SWCNT [93, 94].

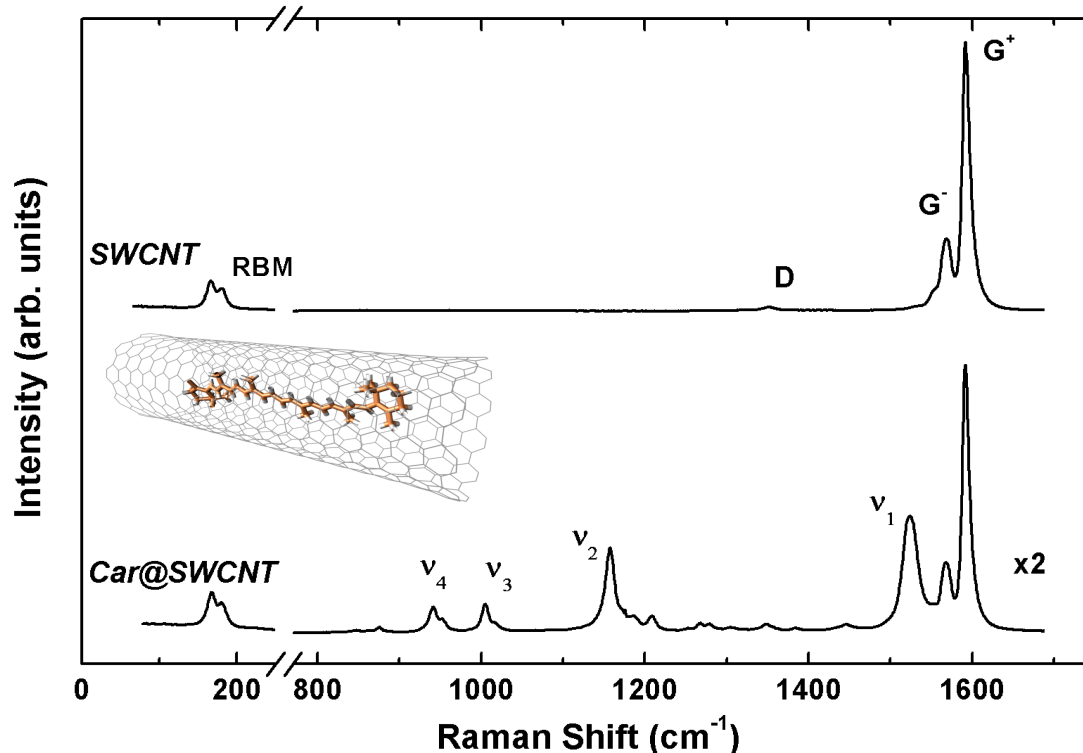


Figure 5.1: Raman spectra of SWCNT and Car@SWCNT excited at 532 nm. In the upper spectrum the modes relating to the SWCNT are indicated. The lower spectrum is 2-times magnified and the most prominent bands of the inserted β -carotene are labeled. The sketch shows a schematic illustration of a β -carotene molecule within a SWCNT.

Moreover, the incorporation of β -carotene inside SWCNTs prevents the degradation of the molecule, which normally occurs by reactions with radical species or isomerization as a result of light stress or intense heat treatment [92, 95].

Figure 5.1 (a) shows the Raman spectra of Car@SWCNT and pristine SWCNTs in the range of 150-1600 cm^{-1} ; the major bands are labeled. Bucky paper of both samples were provided by Kazuhiro Yanagi¹.

For the measurements bucky paper samples with and without incorporated β -carotene were well dispersed in THF and coated on a silicon wafer. Afterwards the solvent was dried on air for 2 hours. The Raman spectra of a SWCNT is characterized by three features: the radial breathing mode (RBM) in the range of 100-400 cm^{-1} , the

¹Present affiliation: Tokyo Metropolitan University

D-mode (defect induced mode) at around 1350 cm^{-1} and the G- or high energy mode at around 1580 cm^{-1} . The latter two can be derived from the vibrational properties of graphite, while the former is a unique feature of SWCNTs. The D-mode arises from a double resonance process and is defect driven [96]. For perfect graphite and SWCNTs, the D-mode is not observable and its intensity increases with an increasing number of defects and impurities. The G-mode originates from shear motions of the graphene honeycomb lattices building the SWCNT. For semi-conducting SWCNTs, the G-mode splits into two components, labeled G^+ and G^- . G^+ and G^- are attributed to the LO and TO phonon, respectively, where LO refers to the axial (longitudinal optical) and TO to the circumferential (transverse optical) displacement of the atoms[97, 98].

The RBM is a vibrational mode with all carbon atoms moving in-phase in the radial direction, performing a motion similar to the chest while breathing. Because the force needed to stretch the carbon atoms is proportional to the number of atoms in the circumference of the tube, the RBM shows a strong dependence on the diameter of the tube and can be used to estimate the chiral indices of the measured SWCNTs.[99]

All three modes are nicely visible in both spectra. The nanotube related Raman modes G^+ , G^- and the D-band show no significant change in terms of shape and position. Due to the unaltered relative D-Mode intensity of the Car@SWCNT it can be assumed, that the process of encapsulation did not induce a large amount of defects to the SWCNT. The Raman spectra of Car@SWCNT in the lower part of Fig. 5.1(a) is 2-times magnified because of an intensity decrease in comparison to the pristine nanotubes. This decrease is due to the incorporation of the carotene molecules which distorts the vibrational motion of the host molecule. This effect is probably increased by the β -carotene inside the SWCNT being not located in the center of the tube, but about 3 \AA aside and thus having a stronger influence on the sidewall of the nanotube[100]. Please note, that the appearance of the ν_4 -peak of β -carotenes is a marker for successful incorporation of the molecule inside the nanotube[92]. The peak originates from an out of plane mode and is forbidden for dissolved β -carotene due to its planar configuration.

To verify the alignment of the β -carotene molecules inside the SWCNT polarization dependent Raman spectroscopy was performed on single Car@SWCNT bundles. To keep the sample intact over the course of the measurements the laser power was adjusted to $50\text{ }\mu\text{W}$ for all measurements. The Raman intensity of SWCNTs shows a strong dependency on the polarization of the incident light. When the polarization vector of the photons is aligned parallel to the tube axis, the tubes exhibit a strong signal while the signal nearly vanishes when the polarization of the excitation source is perpendicular to the tube axis. This phenomenon is called the antenna effect[101]. If the β -carotene molecules are aligned along the tube axis, their behavior should show the same dependency, since the geometry of both molecules are similar.

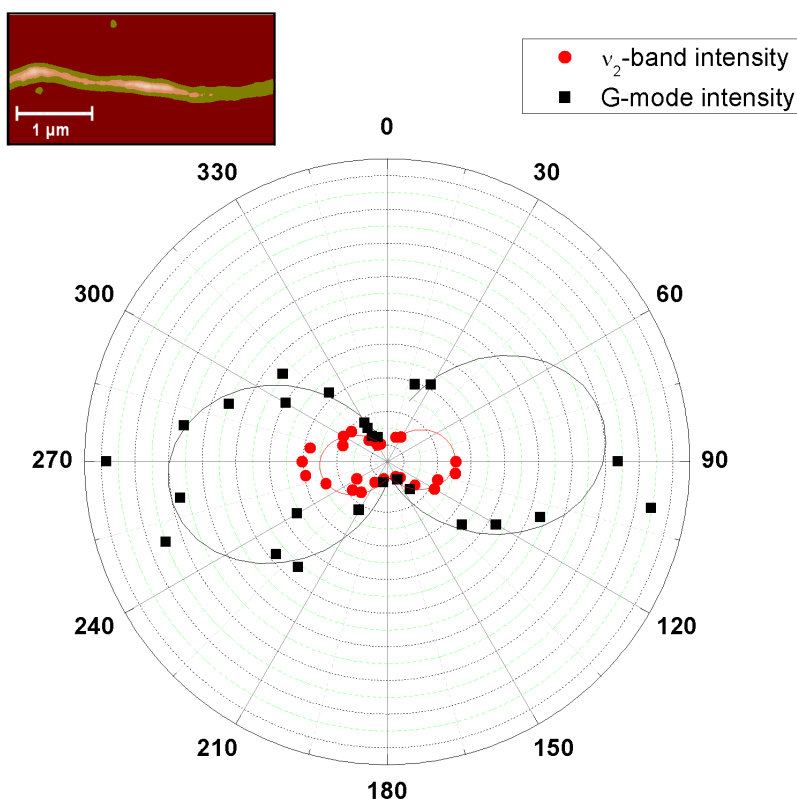


Figure 5.2: Polarization dependence of the ν_2 -band of β -carotene and the G-mode relative to the SWCNTs. The inset AFM picture shows the bundle the spectra were taken from.

The angle dependence of the intensity measured in parallel polarization is shown in Fig 5.2 for the ν_2 -mode (β -carotene) and the G^+ -mode (SWCNT). Both modes exhibit the same angle dependence proving the parallel alignment of the β -carotene molecules with respect to the tube. This result is also in agreement with HRTEM and polarization-resolved optical absorption spectroscopy[100].

To further investigate the vibrational and electronic changes of the functionalized SWCNTs Raman excitation profiles (REPs) were recorded using a bucky paper sample of the functionalized CNT species and a bucky reference sample of CNTs without incorporated β -carotene. The spectra were recorded in the red regime from 2.03 to 2.14 eV excitation energy using undissolved bucky paper sheets fixed on a glass slide. Bulk CaF_2 was used to normalize the intensities of the RBM signal at the different excitation energies. Exemplary data for the RBM region excited at 2.07 eV is shown in Fig. 5.3. Both samples exhibit two distinct RBMs having slightly different frequencies located at 165 cm^{-1} (166 cm^{-1}) and 182 cm^{-1} (183 cm^{-1}) for the pristine nanotubes (Car@SWCNT).

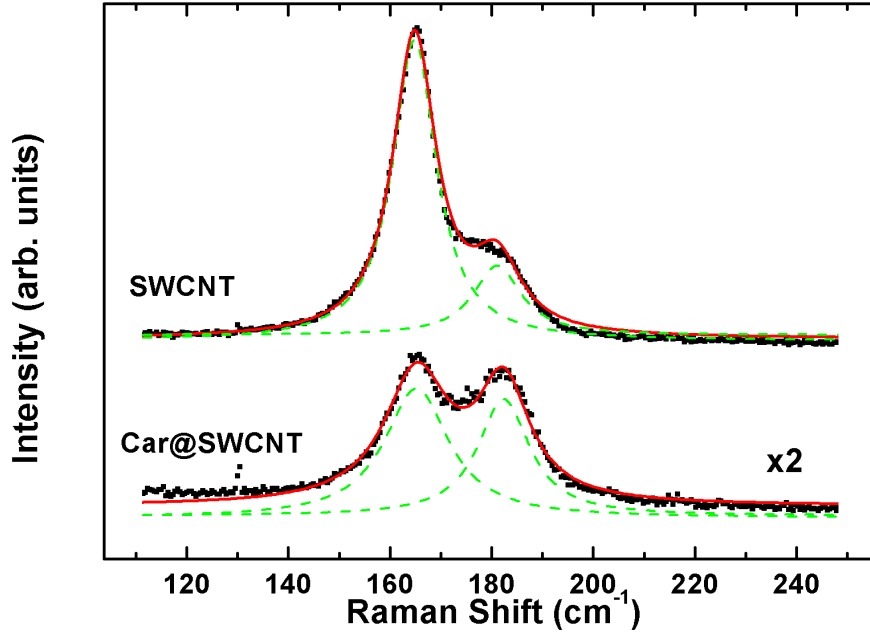


Figure 5.3: Raman spectra excited at 2.07 eV showing functionalized and pristine SWCNTs. The lower spectrum is 2-times magnified.

Former studies of endohedral functionalized nanotubes showed a strong dependence of the radial breathing mode frequency on the diameter of the host SWCNT. In the case of fullerenes, a downshift of the RBM phonon frequency was observed for larger diameter CNTs due to the hybridization of the electronic states of the involved fullerenes and SWCNTs[102]. In contrast, an upshift of the RBM phonon frequency was observed for smaller diameter CNTs due to steric hindrance provided by the fullerenes[90, 91]. This latter mechanism seems to be valid for the observed Car@SWCNT-system since a slight, but measurable and reproducible positional upshift is observed.

Next to the slight shift of the RBM position, Fig. 5.3 reveals a change in the amplitude of the RBMs. This change is not seen for excitation energies above 2.13 eV and mainly affects the RBM located at around 165 cm^{-1} . The RBM at around 182 cm^{-1} bears no significant changes at all and also the REPs for this nanotube species seen in the right part of Fig. 5.4 indicate no significant impact on the encapsulated β -carotene.

The nanotube species responsible for the measured RBM frequency at around 165 cm^{-1} on the other hand show a strong intensity decrease due to the encapsulation (see Fig.

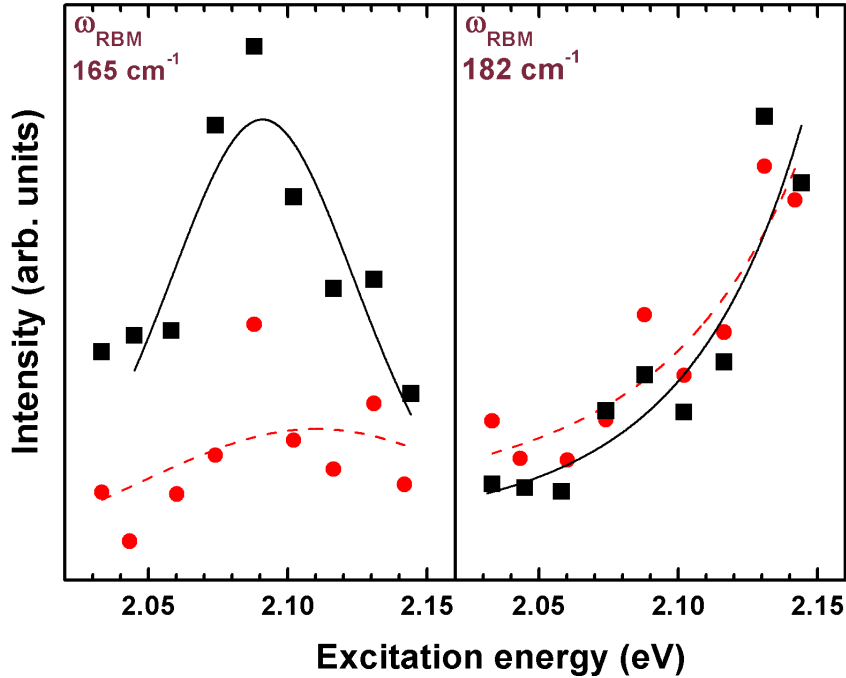


Figure 5.4: Raman excitation profiles (REPs) for the two distinct RBM frequencies at 165 cm^{-1} and 182 cm^{-1} . The red circles correspond to the functionalized Car@SWCNT and the black squares belong to the unfunctionalized species.

5.3 and 5.4). This phenomenon is somewhat unexpected and since both nanotube species are assigned to be semiconducting (as discussed below), metallicity can be ruled out as a reason for the observed behavior. The most reasonable explanation for the strong intensity decrease is a higher filling rate of the involved nanotube species, which would be in agreement with the larger diameter of these specific nanotubes. To estimate the transition energies of the distinct RBM frequency, the RBM intensity profile has to be fitted appropriately. The transition energy is not exactly located at the main position of the RBM profile, but on its low energy side. This is the consequence of the incoming/outgoing resonance phenomenon. By tuning the laser energies two energies fulfill the resonance condition and are called incoming and outgoing resonance. In case of the incoming resonance, the photon energy matches exactly with the band gap energy and the scattered light is lowered in energy by the phonon energy. In case of the outgoing resonance the energy of the incident light minus the energy of the phonon matches the energy band gap of the sample. The

measured RBM dependency on the excitation wavelength reflects both cases but only the incoming resonance corresponds to the exact band gap energy. The REP for semiconducting SWCNTs is described by

$$I(E_l) = \left(\frac{Mc}{\hbar\omega_{RBM}}\right)^2 \left| \frac{1}{E_l - E_{ii} - i\gamma/2} - \frac{1}{E_l - \hbar\omega_{RBM} - E_{ii} - i\gamma/2} \right|^2, \quad (5.1)$$

with E_l being the laser energy, E_{ii} the band gap energy of the optical transition, γ the lifetime broadening of the involved electronic states, M the transition matrix element and c a constant[103, 104].

From fitting the resonance profiles using equation 5.1 we see a slight blueshift for the transition energy being 2.1 eV for the Car@SWCNT and 2.08 eV for the pristine nanotubes. The corresponding data for the other nanotube species are 2.24 eV (SWCNT) and 2.26 eV (Car@SWCNT) but, as it can be seen in Fig. 5.4, these data are not valid due to the limited energy range of our dye laser system.

To assign the chiral indices (n,m) of the investigated nanotube species, the procedure first suggested by Telg and Maultzsch was used[104, 105]. According to them, the information of both, the RBM frequency and the excitation energy is needed for a correct assignment. Having both, the chiral indices of the tubes can be evaluated by comparison of the data with datapoints in a Katauraplot of the investigated regime. The Kataura plot is a graph which relates the energy of the band gaps in a carbon nanotube to its diameter. A nanotube having a certain diameter can be metallic M or semiconducting S and has several band gaps resulting in multiple branches in the Kataura plot [106].

Popov et al.[107] calculated the RBM frequencies and transition energies for more than 300 SWCNTs in the diameter range of 2 - 12 Å. Since his Katauraplot shows the excitation energy as a function of the diameter, the measured RBM frequencies have to be transferred to the diameter of the tube by applying the formula $\omega_0 = 12.5 + 1117.5/R$, with R being the nanotube diameter in Å and ω_0 the RBM in cm^{-1} [107]. This results in diameters of 1.47 nm and 1.32 nm for the corresponding RBM frequencies at 165 cm^{-1} and 182 cm^{-1} , respectively. Knowing the diameter and the transition energies E_{22} from the resonance Raman profiles, the chiral indices (n,m) can be assigned by finding either, the diameter and the transition energy, in the Katauraplot.

Comparing the validity of the estimated RBM frequencies and transition energies with respect to the data calculated by Popov, the uncertainty of the transition energy will be bigger than for the measured diameter. This is because the transition energies are measured for bundled nanotubes, while the calculated values are based on bare samples. The increasing electronic interactions of the π -orbitals of the SWCNTs in

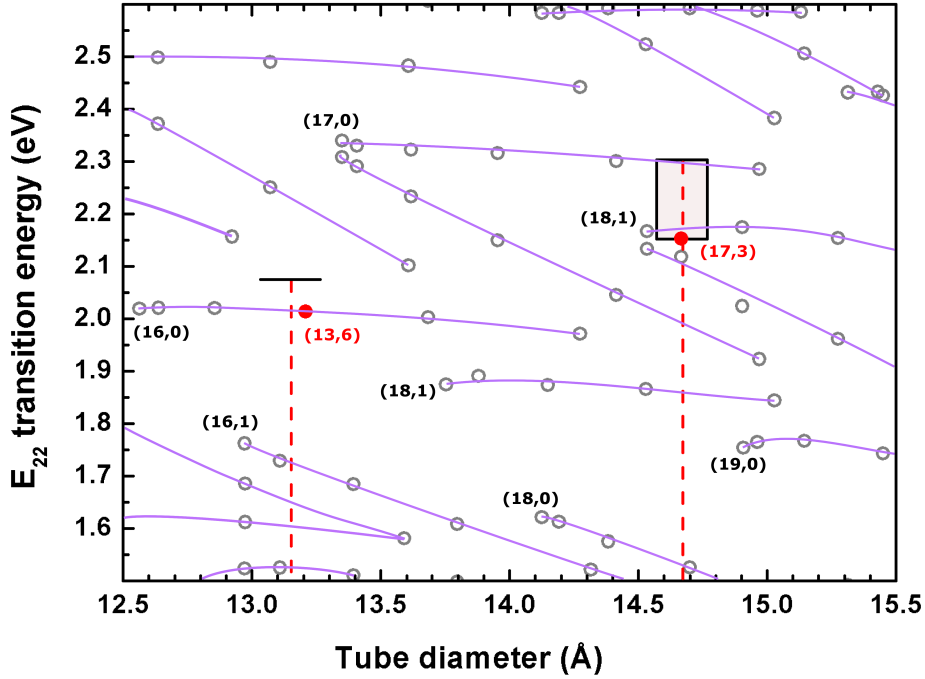


Figure 5.5: Calculated Katauraplot in the region of the estimated transition energies. The individual branches and some SWCNTs are indicated. The red dashed lines correspond to the measured RBM frequencies, while the black line and the gray shaded box correspond to the measured transition energies.

the bundled case lead to a lowering of the excitation energy. The bundling of the tubes has, on the other hand, no effect on the diameter of the SWCNTs. Due to this inaccuracy in the transition energy, at first the measured diameter has to be found in the calculated Katauraplot. In a second step a straight line originating from the estimated position of the diameter is drawn along the transition energy axis. This is done in Fig. 5.5, which shows the relevant region of the Katauraplot calculated by Popov. The red dashed lines correspond to the diameter of the investigated tubes. The black line and the gray shaded box correspond to the measured transition energies for the two measured RBMs, respectively. The transition energy of the nanotube species having its RBM at 182 cm^{-1} could not be obtained unambiguously due to the limits of the used lasersystem. The box therefore reflects the error of the estimated transition energy being centered at 2.24 eV and having a width of 150 meV .

Since a lowering of the transition energies is expected in each of the two cases just one SWCNT comes into consideration. The RBM at 165 cm^{-1} belongs to the $(15,1)$ branch and can be assigned to be a $(17,3)$ tube, the RBM at 182 cm^{-1} is

very probably originating from a (13,6) tube belonging to the (16,0)-branch. In the former case, the transition energy is shifted about 66 meV to lower energies with respect to the pristine samples, for the latter case such a conclusion is not possible due to the unsure value for the transition energy.

In this chapter, Raman measurements on pristine SWCNTs and endohedral functionalized nanotubes were analyzed. The encapsulation has just slight effects on the properties of the SWCNT, only the RBM region shows a response in terms of a frequency shift and change of shape. The corresponding resonance profiles show that these changes are selective and in contrast to exohedral functionalized tubes no redshift of the transition energy is observed. This fact combined with the enhanced optical properties of the Car@SWCNT shows the possible implication this system might have in future devices.

Part II

CdSe nanocrystals

Chapter 6

Colloidal CdSe-based nanocrystals

Colloidal semiconducting nanocrystals (NCs) are inorganic particles with a size in the orders of nanometers. They have attracted great attention for the last decade due to possible applications in nanotechnology and biotechnology. The possibility to grow NCs in high quantity and low costs makes this type of material capable of boosting the development of innovative applications like biological sensors[108, 109], LEDs[110–113], lasers[114, 115], or solar cells[116].

The key for future applications is the high quality of the NCs combined with the ability to tune their diameter very precisely during the growth process. Since the optical properties of NCs are size-dependent the narrow distribution in size will also lead to a narrow distribution in terms of effective band gap energy.

The crucial parameters for every optical material are its quantum yield, stability and lifetime. In case of NCs all these parameters are related to the dangling bonds at the surface and can be improved dramatically by epitaxial coating of the core with a second material. Epitaxial coating passivates the dangling bonds and results in a core-shell structure. The coating has several additional advantages: first of all it protects the core chemically and leads to an overall more robust system. The shell material can also be used as an interface layer allowing a further functionalization of the core-shell system and can make it applicable in many kinds of environments [12, 117]. Recent studies show the suppression of blinking and Auger recombination by a subsequent coating of the NCs[118]. Since these parameters are crucial for the development of optoelectronic devices, these results emphasize the possible importance of NCs in the near future [119].

However, the lattice mismatch between the NC core and the shell introduces strain into the lattice of the NC core and the shell itself. This has a significant impact on the NC structure and can even be used to tune the electronic and optical properties of the NC[120].

In this work solely NCs using CdSe as core material are investigated. This material has attracted a wide attention in the last years, because its emission wavelength can be tuned very precisely over the whole visible spectral range[121]. Several semiconductors have been employed as shell material in the past, *e.g.* CdS[122, 123], ZnS[124, 125] and ZnSe[126]. CdS provides a moderate lattice mismatch with respect to CdSe (3.9 %). Therefore its epitaxial coating leads to only a small number of defects compared to other shell materials. This results in high achievable quantum yields of those systems. Up to 80 % are reported[127]. However, the difference in band gap energy between CdSe and CdS is not large enough to localize both, electron and hole within the CdSe core. While the hole is confined in the core, a size dependent bathochromic shift in the photoluminescence (PL) spectrum indicates the delocalization of the electron over the complete core-shell system[5].

In this chapter the size-dependent confinement effects are introduced and the concept of the growth of colloidal NCs is described. The samples investigated in this work are presented and their structural and optical properties are discussed.

6.1 Quantum and phonon confinement

The optoelectronic properties of semiconducting materials are classically purely dictated by their chemical composition. This changes when the size of the particles is in the same order of magnitude as the wave functions of the electron and hole. In such a case the electrons and holes can no longer be treated as free particles. As a result of this confinement the energy spectrum becomes discrete and the optical absorption and emission spectra accordingly size-dependent. Different types of confinement can be distinguished, whether the confinement occurs in one, two or in all three spatial dimensions. The formed structures are called quantum wells, quantum wires and quantum dots, respectively. This work deals solely with quantum dots having a diameter below 10 nm.

A mathematical model for the quantum confinement for spherical quantum dots was developed by L.E. Brus [6, 128]. He started with the Hamiltonian of an electron hole pair which is given by

$$\hat{H} = -\frac{\hbar^2}{8\pi^2 m_e} \nabla_e^2 - \frac{\hbar^2}{8\pi^2 m_h} \nabla_h^2 + \hat{V}, \quad (6.1)$$

where m_e and m_h denote the effective masses of the electron and hole, respectively. The potential energy \hat{V} of an electron-hole pair can be written as the sum of the Coulomb interaction between the two particles and the polarization energy:

$$\hat{V} = \hat{V}(r_e, r_h) = \hat{V}_{Coul} + \hat{V}_{Polar}. \quad (6.2)$$

The latter arises since a point charge inside a NC polarizes the crystal which can affect the energy of a second charge. Due to the strong overlap of the electron' and holes' wave functions in the case of confinement, the polarization term will be small compared to the Coulomb term and is therefore neglected in the following. The Coulomb energy is expressed as

$$\hat{V}_{Coul} = -\frac{e^2}{4\pi\epsilon_r\epsilon_0|r_e - r_h|}, \quad (6.3)$$

with ϵ_r being the relative permittivity of the material.

To evaluate the Eigenvalues of the Hamiltonian given in eq. 6.1 a wave function $\Phi(r_e, r_h)$ must be determined. $\Phi(r_e, r_h)$ has to be a function of the electron and hole within the NC. In a first-order approximation the uncorrelated wave functions

$$\Phi(r_e, r_h) = \Psi_e(r_e)\Psi_h(r_h) \quad (6.4)$$

of the two charges can be used to evaluate the lowest energy of the electron-hole system. Solving the Schrödinger equation by using this wave function leads to the Brus equation for the band gap of the lowest-energy exciton:

$$E_{bg} = E_{bg,bulk} + \frac{\hbar^2}{8R^2} \left(\frac{1}{m_e} + \frac{1}{m_h} \right) - \frac{1.8e^2}{4\pi\epsilon_r\epsilon_0 R} + \text{smaller terms}, \quad (6.5)$$

with R being the radius of the spherical quantum dot and E_{bg} and $E_{bg,bulk}$ the band gap values for the quantum dot and bulk material, respectively. Albeit the Coulomb term shifts E_{bg} to lower energies, with R^{-1} for small R like in the case of quantum dots, the correlation term, which shifts the energy to higher energies will be the dominant term since it scales with R^{-2} . Calculating the respective band gap energy for CdSe leads to good results for quantum dots larger than 3 Å in diameter[129].

Next to the electronic wave functions also the vibrational wave functions are restricted to the volume of the quantum dot. This phonon confinement leads to the relaxation of the conservation of the momentum of the phonons and as a consequence the whole Brillouin zone becomes detectable in the Raman spectra. A general model applied for silicon-nanostructures was developed by Richter *et al.*[130]. Since the phonon wave function has to be restricted to the core, Richter treated the dimension

of the crystal in form of a Gauss-distribution. The wave function of the phonons with the wavevector \mathbf{q}_0 can then be written as

$$\begin{aligned}\Psi(\mathbf{q}_0, \mathbf{r}) &= W(\mathbf{q}_0, \mathbf{r}) \Phi(\mathbf{q}_0, \mathbf{r}) \\ &= A \cdot \exp\left(-r^2/2 / (L/2)^2\right) \Phi(\mathbf{q}_0), \\ &= \Psi'(\mathbf{q}_0, \mathbf{r}) \cdot u(\mathbf{q}_0, \mathbf{r})\end{aligned}\quad (6.6)$$

with $W(\mathbf{q}_0, \mathbf{r})$ as the weighting function, A its amplitude and L the diameter of the sphere. $\Phi(\mathbf{q}_0, \mathbf{r})$ is the phonon wave function defined as

$$\Phi(\mathbf{q}_0, \mathbf{r}) = u(\mathbf{q}_0, \mathbf{r}) e^{-i\mathbf{q}_0 \cdot \mathbf{r}}, \quad (6.7)$$

where $u(\mathbf{q}_0, \mathbf{r})$ possesses the periodicity of the crystal lattice.

To calculate the effect on the Raman spectrum, Ψ' is expanded in a Fourier series

$$\Psi'(\mathbf{q}_0, \mathbf{r}) = \int d^3q C(\mathbf{q}_0, \mathbf{q}) e^{i\mathbf{q} \cdot \mathbf{r}}, \quad (6.8)$$

where the Fourier coefficients $C(\mathbf{q}_0, \mathbf{q})$ are defined as

$$C(\mathbf{q}_0, \mathbf{q}) = \frac{1}{(2\pi)^3} \int d^3r \Psi'(\mathbf{q}_0, \mathbf{r}) e^{-i\mathbf{q} \cdot \mathbf{r}}. \quad (6.9)$$

When treating a spherical NC and only first order Raman scattering ($\mathbf{q}_0 = 0$) this leads to

$$|C(0, q)|^2 \cong e^{-q^2 L^2 / 4} \quad (6.10)$$

and the first order Raman spectrum can then be calculated from

$$I(\omega) = \int \frac{d^3q |C(0, \mathbf{q})|^2}{(\omega - \omega(\mathbf{q}))^2 + (\Gamma_0/2)^2}, \quad (6.11)$$

where $\omega(\mathbf{q})$ denotes the phonon dispersion and Γ_0 the natural linewidth.

6.2 Colloidal nanocrystal growth

Synthesis techniques for nanomaterials are numerous in literature[4, 131–133]. Bottom-up methods, where NCs are grown by the nucleation of an initial seed, have gained special attention since these approaches yield inexpensive nanomaterial in good quality and quantity. By using wet chemical methods to synthesize NCs, the shape and size of the reaction products are very precisely tunable by tweaking the composition and concentrations of the used chemicals as well as the reaction temperature[4].

For a typical colloidal NC synthesis three components are inevitable: precursors, organic surfactants and a solvent (in some cases the surfactant also serves as solvent). The precursor contains, chemically bound, the inorganic constituents of the intended NCs, while the organic surfactants mediate the growth of the NCs in the solution. The synthesis of colloidal NCs occurs in two steps: firstly the nucleation of a seed of nanocrystals and secondly their subsequent growth.

The nucleation step occurs after passing a critical temperature. For the nucleation step the precursors are dissolved with the help of organic surfactants. Both components are, at a specific temperature, quickly added into the heated solvent as sketched in Fig. 6.1. Within the solvent, the precursors convert into active monomers and after exceeding a level of supersaturation they start to form crystal nuclei. The formation of the nuclei results in a drop of temperature which instantly stops the nucleus formation. The formed nuclei can grow subsequently by incorpo-

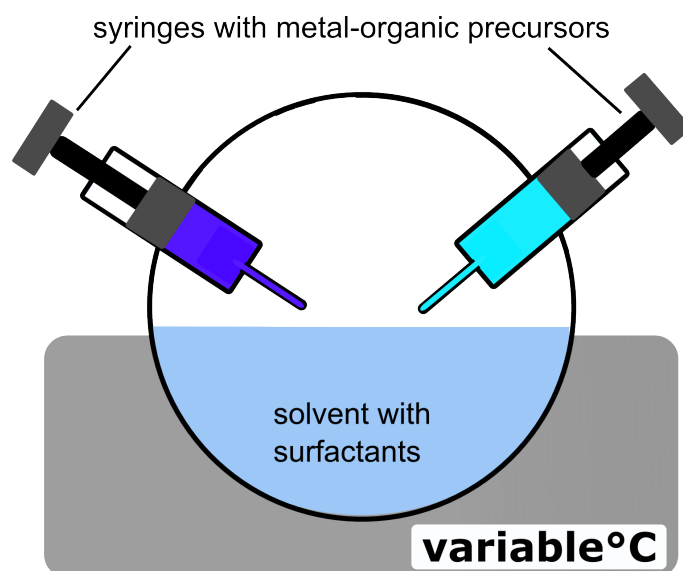


Figure 6.1: Schematic setup for the synthesis of colloidal nanocrystals.

ration of monomers still present in the solution until the desired size of the particles is reached.

The key for controlling colloidal crystal growth is the proper choice of the reaction temperature and specific precursors/surfactants suitable at that temperature. The reaction temperature has to be high enough to allow the rearrangement of atoms during the growth to yield high-quality crystalline products. If chosen too high, the size and shape of the particles are going to be uncontrollable during the synthesis; typical temperatures for colloidal growth are in between 200 and 400°C. A requirement for the precursors is the ability to release their embedded inorganic components rapidly after passing the chosen reaction temperature. The surfactants are chosen according to their affinity to adhere to a growing crystal. The adhesion energy is crucial since it has to allow the surfactant to 'hop' on and off the surface of the forming crystal making specific areas of the crystal accessible for future growth[134]. But the surfactants not only bind to the NC surface. They also mediate the integration of this species into present NCs by forming complexes with dissolved monomers.

The adhesion energy as well as the stability and diffusion rate of the monomer-surfactant complex: all these parameters are temperature-dependent and since there is no straightforward mechanism to determine the adhesion energy experimentally or theoretical, the choice of appropriate surfactants has to be done empirical.

The ability to produce NCs exhibiting a narrow size-distribution is the key for the implementation of NCs in future products. These narrow size distributions can be obtained either by separating fractions of NCs with a narrow size distribution from a solution with a broader size distribution[134, 135] or by synthesizing the NCs in a manner automatically yielding a narrow size distribution.

The latter concept is preferable since it is less time-consuming and it does not produce any rejections; it becomes possible by a procedure called size-distribution focusing. This procedure is based on the fact, that small crystals grow faster than larger ones after passing a threshold size for a high monomer concentration[136]. This behavior is schematically shown in 6.2, which shows the dependence of the growth rate on the size of the particles for a high and a low monomer concentration within the reaction chamber. For any monomer concentration there exists a critical size at which the crystals neither grow nor shrink. For a rising monomer concentration this critical size becomes smaller and only very tiny crystalites are not growing but shrinking. For a high monomer concentration larger NCs grow significantly slower than the smaller ones due to the steep slope of the curve. This is in Fig. 6.2 symbolized by arrows and leads finally to a very narrow size-distribution of the particles (focussing). This is in contrast to the case of a low monomer concentration. In this case, there is no great difference in the growth rate after passing the critical size. Nearly all NCs exhibit the same growth rate, which leaves the present (broad) size distribution nearly unaltered (defocussing).

The conclusion of the just mentioned is that to receive a narrow size distribution, it

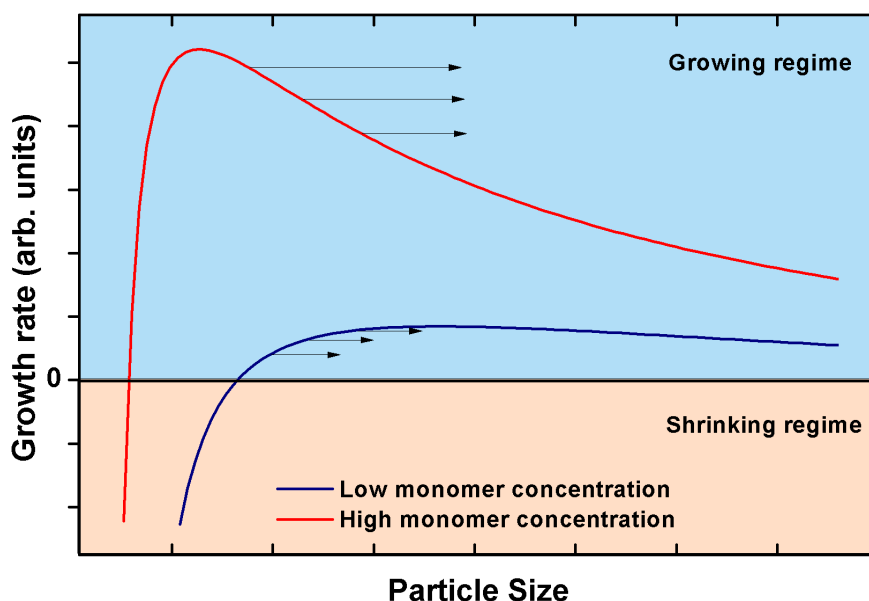


Figure 6.2: Schematic growth rate dependence with respect to the particle size for two different monomer concentrations. The arrows symbolize the growth rate at specific particle sizes. For a high monomer concentration smaller particles grow faster than larger ones resulting in a “focused” size distribution. For a low monomer concentration the growth rates alters only slightly for different particle sizes; the final size distribution is therefore broadened.

is favorable to have a high monomer concentration within the reaction chamber. To achieve this, the monomer concentration can be increased manually at a fixed rate by a second injection of precursors into the solution. If the monomer concentration is tuned correctly, the distribution of NC sizes present in the solution will lie on the falling side of the growth versus radius curve and the size distribution will become narrower (see the arrows in Fig. 6.2).

Plain NCs possess relatively low PL efficiencies and offer a low stability against oxidation. To overcome this, the particle can be coated with an epitaxial shell layer. A well established method to grow the additional shell layers is the successive ionic layer adsorption and reaction (SILAR) procedure. This approach is based on the successively insertion of precursors in low concentration containing either the anionic and cationic part of the inorganic shell material into the reaction solvent. The ionic constituents adhere to the core crystal and react to form the shell. Due to the low precursor concentration inhomogeneous nucleation of the shell material is avoided and the monodispersity of the NCs is preserved during the growth process. Additionally, the ability to grow single shell layers makes it possible to control the

thickness of the layer very precisely.

6.2.1 Sample synthesis

The synthesis of the nanocrystals investigated in this work was performed by Karel Lambert¹; Table 6.1 summarizes the sample compositions and sizes of the synthesized NCs. The synthesis of the bare CdSe NCs followed the protocol described by Jasienak et al.[137]. CdSe NCs were synthesized starting for selenium dissolved in octadecene (ODE-Se) and cadmium oleate ($\text{Cd}(\text{OA})_2$). For a typical CdSe synthesis, the $\text{Cd}(\text{OA})_2$ precursor is liquified at 100 °C, and 1.21 mL of it (0.36 mmol Cd) is added to 12 mL ODE. The mixture is degassed for 1 h at 100 °C under nitrogen, followed by heating to 265 °C, and the ODE-Se (3.6 mL, 0.36 mmol Se) is injected. The temperature of the mixture drops after injection, and the reaction continues at 235 °C until it is stopped by fast cooling. This procedure results in zinc blende (zb) CdSe NCs, stabilized by oleate ligands. The bare CdSe NCs used in this study have a mean diameter of 4.0 nm ('bare core').

For coating the bare CdSe NCs with an additional CdS shell the SILAR approach is used. The Cd and S precursors were prepared separately prior to the coating reaction. For the S precursor the sulfur is dissolved in ODE. For the Cd precursor, CdO is dissolved in a mixture of OA and ODE. For a typical SILAR reaction, *n*-octadecylamine (ODA) and ODE were mixed and degassed for 1 h at 100 °C under nitrogen flow. Then, 10^{-5} mmol CdSe cores dispersed in hexane are added to the mixture, followed by further degassing for 1 h at 100 °C. Next, the temperature is increased to 225 °C. After ten minutes, the first precursor is added; S is added first, then Cd, *etc.*. The amount of added precursors was calculated to obtain a full S or Cd monolayer on the particle surface with every injection, and the mixture was

¹Present affiliation: patent office Ghent, Belgium

Sample composition	CdSe core size (nm)	Total diameter (nm)
CdSe	4.0	4.0
CdSe/2CdS	4.0	5.1
CdSe/3CdS	4.0	5.6
CdSe/5CdS	3.6	6.8
CdSe/3Cds/2ZnS	3.6	6.6
CdSe/2CdS/3CdZnS/2Zns	3.6	8.2

Table 6.1: Composition and diameter of the samples investigated in this work.

allowed ten minutes to react between each addition. For this work, CdSe/ n CdS core shell NCs with $n=2, 3$ and 5 denoting the number of CdS monolayers were prepared starting from different CdSe cores with diameters in the range of 3.6–4.0 nm (see Table 6.1).

For the NCs containing ZnS, the ZnS was either directly grown on top of the CdSe/CdS quantum dots or an intermediate (Cd,Zn)S alloy layer was grown first. For the Zn precursor, ZnO is dissolved in a mixture of OA and ODE at 310 °C. The (Cd,Zn) precursor (0.05 M in Cd and Zn) was made by mixing equal volumes of the Cd and Zn precursors. The ZnS and Cd_{0.5}Zn_{0.5}S alloy layers are grown as described above, yet at a temperature of 185 °C. For this work, CdSe/3CdS/2ZnS and CdSe/2CdS/3CdZnS/2ZnS samples were prepared (see Table 6.1).

6.3 Structural investigation

To obtain information about the crystal structure of the synthesized NCs X-ray diffraction (XRD) and high-resolution transmission electron microscopy (HR-TEM) were performed. While the former provides knowledge about the crystal structure of the NCs the latter can also be used to determine the shapes, the sizes and the size distribution of the produced NCs. All XRD/TEM pictures presented in this work are courtesy of Karel Lambert. XRD samples of colloidal quantum dots were prepared by evaporating the solvent and resuspending the particles in an 80:20 hexane:heptane mixture and subsequent dropcasting on a 1x1 cm glass slide. The

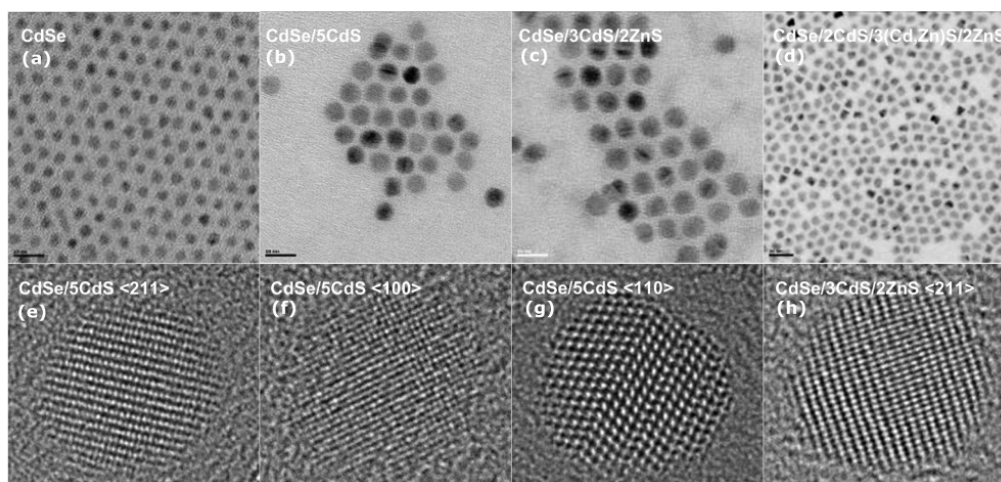


Figure 6.3: HR-TEM images of the samples investigated in this work. Subfigures (a)-(d) show brightfield overview images of four different samples, while (e)-(h) are high-resolution images of single quantum dots. The specific sample composition is indicated.

samples were measured with a Bruker D8 Discover. TEM samples were prepared by dip coating a carbon-coated copper grid in a diluted quantum dot suspension with a particle concentration around 1 mM, and HR-TEM images were recorded with a Cs-corrected JEOL 2200 FS microscope.

Figure 6.3 displays exemplary different TEM micrographs of the quantum dot samples.

An overview TEM picture of the bare CdSe cores is shown in Figure 6.3(a). The picture reveals the monodispersity of the bare cores as well as their spherical shape. The XRD spectrum of this sample is shown in Fig. 6.4 (A) and it is consistent with the zinc blende modification of the CdSe which is in line with the used synthesis route described above. The XRD peaks are broadened with respect to bulk CdSe due to the small crystal size.

For CdSe/5CdS NCs the overview TEM picture (Fig. 6.3 (b)) still exhibits a quasi-spherical shape indicating a coherent and homogeneous shell growth up to this point. HT-TEM pictures from the $\langle 211 \rangle$ and $\langle 100 \rangle$ direction show a well ordered quantum dot (Fig. 6.3 (e) and (f)). For the $\langle 100 \rangle$ direction multiple stacking faults along the $\langle 111 \rangle$ axis are seen in Fig. 6.3, which indicates a zinc blende/wurtzite polytypism. This is common due to the small energy difference between the two modifications (less than 10 meV per atom)[138, 139]. This view is supported by the XRD spectra (see Fig. 6.4 B) which exhibits a shoulder for the (111) reflection which can be assigned to arise from the polytypism. However, the XRD data also show that the character of the samples is still zinc blende-like and only a small fraction of NCs have their phase changed.

Comparing the XRD data of the bare and overcoated NC one can see that the peaks

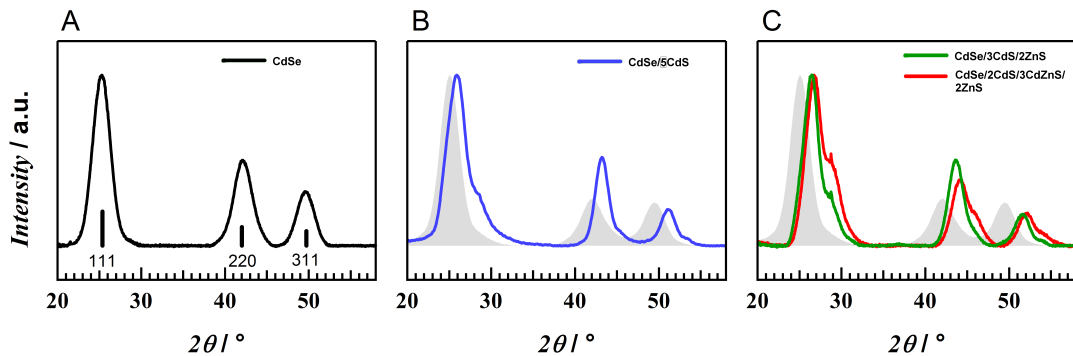


Figure 6.4: XRD-data of the investigated samples. (A) displays the spectrum of the bare NCs, the positions of the zinc blende modification are indicated. (B) XRD data of the CdSe/5CdS sample. (C) XRD spectra of the CdSe/3CdS/2ZnS (green) and the CdSe/2CdS/3CdZnS/2ZnS (red) particles. The gray shaded area in B and C corresponds to the spectrum of the bare NC.

of the (220) and (311) reflections become sharper with the overcoating indicating a homogeneous shell growth. The XRD diffractogram yields reflections that are in between those of zinc blende CdSe and CdS. The mentioned absence of a peak broadening indicates that this results from a combined expansion of the CdS lattice and a compression of the CdSe lattice in the particles, rather than from a convolution of separate CdSe and CdS reflections[140].

The powder XRD pattern of CdSe/3CdS/2ZnS NCs shown in 6.4 C is similar to that of CdSe/5CdS NCs, except an additional shift to larger angles for the latter. This means that, apart from a further compression of the CdSe core and an expansion of the ZnS shell, the two particle types have largely the same structure. The XRD data still is in line with a zinc blende type NC, although the feature exhibited for the CdSe/CdS NCs still indicates a fraction of wurtzite type NCs. According to the TEM images (Figure 6.3 (c)), the particles are still monodisperse, but their shape is affected by non-isotropic growth.

The reflections of the diffractograms shift to larger angles for the sample having the CdSe/2CdS/3Cd_{0.5}Zn_{0.5}S/2ZnS composition, but the broadening of the (220) and (311) reflections indicates a loss of coherence of the crystal lattices of core and shell assuming that the growth is not completely epitaxial anymore. This is also in line with overview TEM images, which clearly show the formation of more irregular NCs. Both ZnS-containing samples show serious lattice warping in the HR-TEM (Fig. (h)) which is evidence of significant lattice strain within the sample.

6.4 Optical properties of colloidal nanocrystals

The optical properties of the studied NCs are investigated *via* absorbance and photoluminescence measurements. Compared to bulk CdSe the transition energy as well as the absorption properties of the crystals are, due to the quantum confinement, strongly affected by its size.

Figure 6.5 (a) and (b) displays absorbance spectra of the samples investigated in this work. The spectra are normalized at the wavelength λ_0 of the first exciton peak. The absorbance spectra of CdSe NCs exhibit a peak for the first excited state between 475 and 600 nm (2.61 - 2.07 eV)[141]. According to [142] the evolution of the band gap energy (in eV) for zb-CdSe-NCs is experimentally given by

$$E_g = 1.74 + \frac{1}{0.89 - 0.36d + 0.22d^2}, \quad (6.12)$$

with d being the diameter of the quantum dot in nm and 1,74 is the band gap energy of bulk CdSe being 1.74 eV. Using equation 6.12 with $d = 4$ nm yields $\lambda_0 = 597$ nm which matches perfectly with the observed absorption maximum.

In line with published results, the CdS shell deposition leads to a dramatic increase of the absorbance below 500 nm, corresponding to the onset of the absorption in bulk CdS around 512 nm[143, 144]. In addition, Fig. 6.5 (b) exhibits a progressive redshift upon CdS shell deposition, especially for the first two layers. These shifts can be attributed to the larger extension of the electronic wave function, which leaks into the CdSe shell.[143–145]. The growth of the final two ZnS shell layers results in a subsequent blueshift of λ_0 . This blueshift is attributed to the large lattice mismatch between CdS and ZnS leading to a significant amount of compressive strain within the quantum dot after the ZnS coating. Since compressive strain does increase the energy bandgap of semiconductors[146] it competes against the redshift due to the electron wave function leakage and has a significant impact on the optical properties of the grown samples.

Figure 6.6 (a) displays the PL spectra of CdSe core and CdSe/ n CdS core/shell NCs with $n=2,3$ and 5. In line with the redshift of λ_0 , the PL spectrum shows a systematic redshift with increasing CdS shell thickness. More importantly, the quantum yield (QY) systematically increases with n , up to a value of 35% after five CdS layers (see Fig. 6.6 B). The increase results from the passivation of dangling bonds at the surface of the CdSe core. This dangling bonds act like trap states leading to radiationless decay channels of the excited electron-hole pair. Unlike the uncoated CdSe

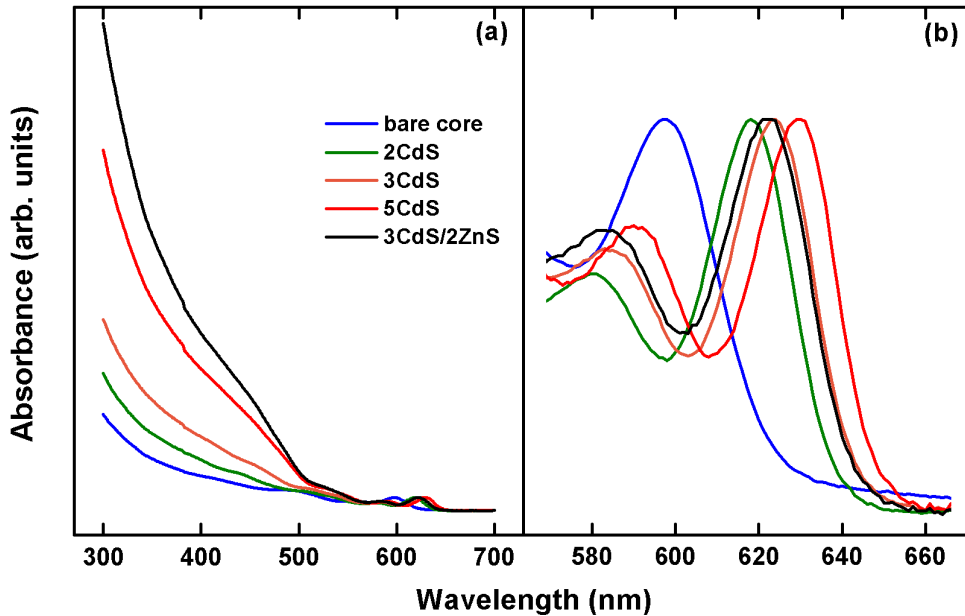


Figure 6.5: Normalized absorbance spectra taken during the coating reactions. (a) is an overview spectrum, while (b) display the same data in the region around the wavelength λ_0 of the first exciton peak.

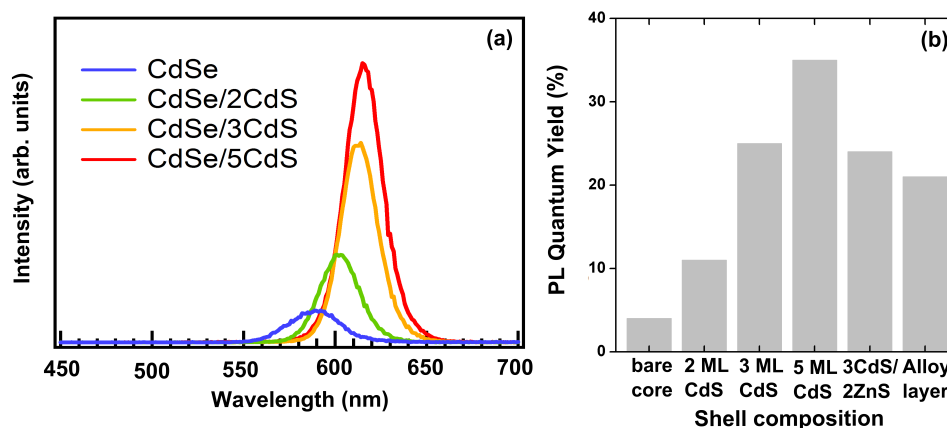


Figure 6.6: Photoluminescence spectra and quantum yields of the samples investigated in this work.

NCs, the CdSe/CdS quantum dots are highly stable against oxidation. CdSe/CdS monolayers stored in air are luminescent for weeks.

Overcoating CdSe/CdS NCs with a single layer of ZnS leads to a further enhancement of the PL-QY, up to 42% for CdSe/3CdS/ZnS (not shown). However, the next S precursor injection leads to a reduction of the PLQY to 20-25%. This decrease originates from the generation of crystalline imperfection such as stacking faults in the quantum dot due to the high compressive strain induced by the ZnS. These imperfections are similar to dangling bonds and diminish the QY. Similar results are obtained also after the introduction of a (Cd,Zn)S buffer layer (see FIG. 6.6 (b)).

Chapter 7

Raman spectroscopy of CdSe based nanocrystals

In this chapter the Raman spectra of the NCs introduced in chapter 6 are presented. All Raman spectra were recorded at liquid helium temperature using an excitation wavelength of 497 nm. The laser power was kept below 5 mW to avoid laser heating. All appearing Raman modes are assigned and their positional dependence on the sample composition is discussed in terms of strain, formation of an alloyed interface layer and exciton-phonon coupling.

7.1 The Raman spectra of CdSe and CdSe/CdS nanocrystals

Fig. 7.1 shows overview Raman spectra of the bare CdSe NCs and CdSe/ n CdS NCs measured in this work; n thereby denotes the number of monolayers grown on top of the bare CdSe core.

The spectrum of bare CdSe nanocrystals is shown in Fig. 7.1 (a) and is dominated by a band at around 210 cm^{-1} . This band can be fitted with the sum of three Lorentzian functions. The most prominent of these three features is located at 207.6 cm^{-1} and corresponds to the 1st order CdSe longitudinal optical phonon (LO). Compared to a bulk value of 218 cm^{-1} at liquid helium temperature[147] the phonon frequency is shifted to lower wavenumbers, which is relatable to the phonon confinement.

Next to the CdSe LO, the band also contains contributions from additional features at either the low-energy and high-energy shoulder of the band.

The asymmetry in the low-frequency part of the LO-phonon Raman peak is caused by surface-optical (SO) phonon modes[148, 149]. The mechanism which probably accounts for the shoulder at the high-frequency side of the LO peak are combination modes due to sequential scattering on optical and acoustical phonons, i.e. LO+LA, LO+TA, as discussed by Dzhagan *et al*[150, 151].

Besides the 2nd and 3rd order of the modes of the LO region at around 400 and 600 cm⁻¹, respectively, no other modes are visible in the Raman spectrum of the bare NCs. The peak at 520 cm⁻¹ is related to the silicon substrate.

After introducing CdS as shell material, the Raman spectra of the NCs show additional features as shown in Fig. 7.1 (b-d). The most intense new Raman feature is a band around 300 cm⁻¹ composed of two underlying modes. Since the high-energy component becomes more distinct for increasing shell thicknesses this component is attributed to be the CdS LO, whose bulk value is located at 305 cm⁻¹. The feature at the low-energy shoulder will be discussed in detail in section 7.3. Briefly, the mode is relatable to an interface layer between the CdSe and CdS and might also contain contributions from a CdS SO mode.

But also the CdSe LO region shows a change in terms of shape after the CdS coating. The low energy shoulder does no longer contain contributions solely from the CdSe SO but also from a second mode. This new mode has also a huge impact on the shape of the second order of the CdSe LO, which exhibits a very unsymmetric shape for the core/shell (CS)-systems (see Fig. 7.1 (b-d)). Since the first order consists of three modes, the second order can stem from up to 6 submodes. Fitting the band with 6 Lorentzians yields in an appropriate fit of the band. Next to the smoothing of the 2nd order also its intensity diminishes after coating. The 3rd order, which is nicely visible in the case of the bare cores, vanishes nearly completely after coating. Overtones of the shell material as well as mixed overtones of core and shell are also present in the Raman spectra. The overtones are indicated in Fig. 7.1 in blue and black for the CdS- and CdSe-related Raman bands, respectively. Mixed overtones, formed by combinations of the fundamental modes of both composites, are indicated in wine. The spectral position and the assignment of all observed Raman bands are summarized in Table 7.1.

Next to the appearance of new Raman modes with the CdS shell deposition the position of all present modes shows a dependency on the shell thickness. A general trend is a shift to higher frequencies with increasing CdS shell thickness, e.g. the CdSe LO phonon frequency is upshifted 3.2 cm⁻¹, 5.2 cm⁻¹, and 6.6 cm⁻¹ with respect to the bare CdSe NCs for the deposition of 2, 3 and 5 ML of CdS, respectively. In section 7.2, these observed LO shifts are directly related to strain.

With respect to bulk material the presented CdSe and CdS LO values are shifted to lower wavenumbers, albeit this difference becomes smaller for the CS nanocrystals. As just mentioned the strain present in the sample is responsible for the latter while the former effect is based on phonon confinement. The phonon confinement weakens

7.1 The Raman spectra of CdSe and CdSe/CdS nanocrystals

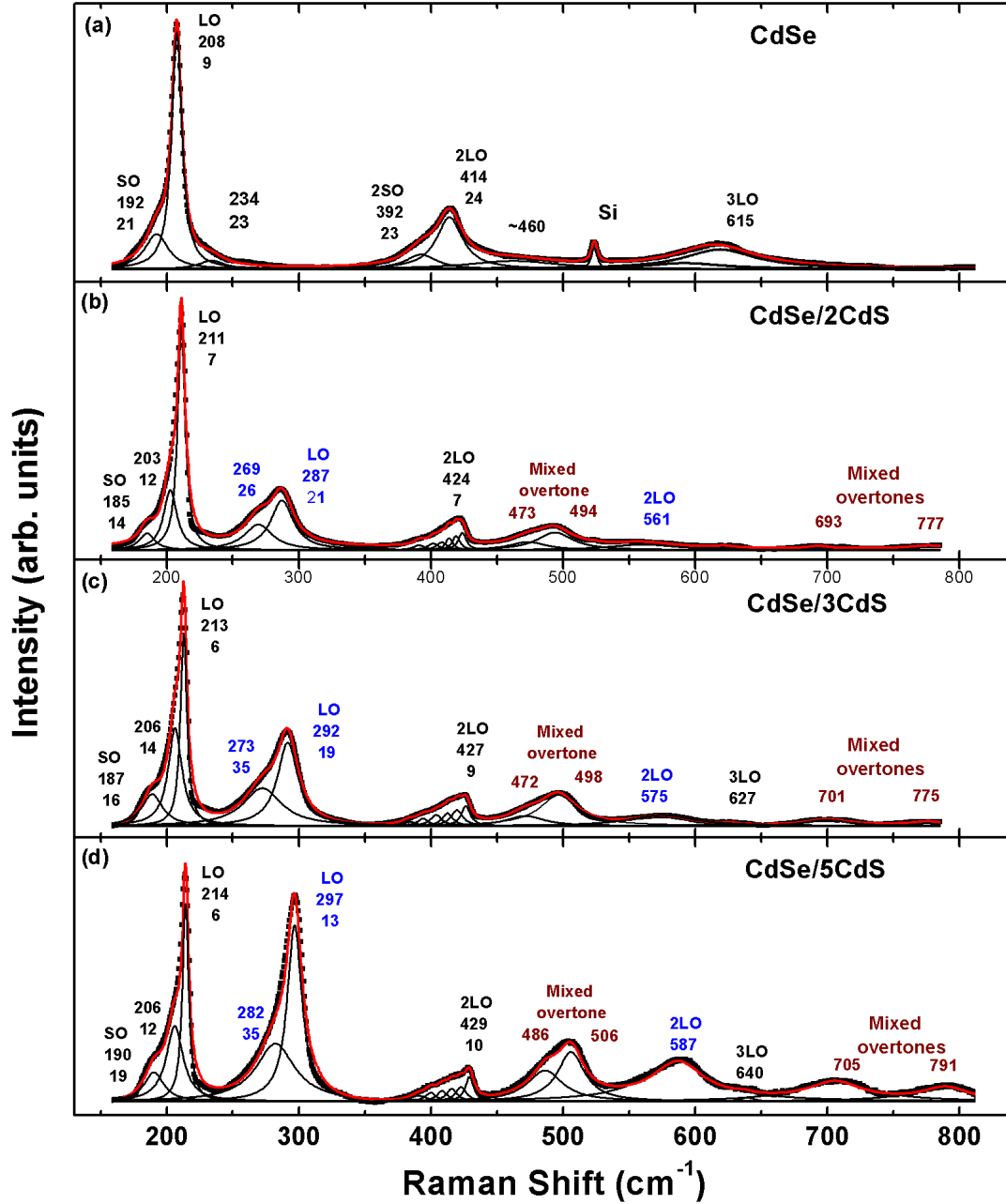


Figure 7.1: Raman spectra of (a) bare CdSe nanocrystals and with (b) a 2 ML, (c) a 3 ML and (d) 5 ML CdS shell. The numbers correspond to the frequency and the width of the modes. The blue labeling corresponds to CdS-related Raman bands, while the black labeling corresponds to CdSe-related Raman bands. Mixed overtones are indicated in wine.

bare CdSe NCs		CdSe/ <i>n</i> CdS NCs			
Phonon freq. (cm ⁻¹)	Band Composition	Phonon freq. (cm ⁻¹)			Band Composition
		<i>n</i> =2	<i>n</i> =3	<i>n</i> =5	
192.3	SO _{bc}	185.2	187.3	190.4	SO _{cs}
-	-	202.7	205.8	206.4	IP
207.6	LO _{bc}	211.1	212.8	214.2	LO _{cs}
234.1	LO _{bc} +LA/TA	-	-	-	-
-	-	269.4	273.3	282.2	IP/SO _{cs}
-	-	287.2	291.6	296.7	LO _{cs}
-	-	380-430	380-430	380-430	mult. comp.
-	-	423.6	426.5	429.1	2LO _{cs}
391.9	2SO _{bc}	-	-	-	-
413.9	2LO _{bc}	-	-	-	-
-	-	473.4	471.6	486.4	2LO
-	-	494	497.7	506.1	LO _{bc} +LO _{cs}
-	-	560.7	574.9	586.7	2LO _{cs}
591.2	3SO _{bc} /2SO _{bc} +LO _{bc}	-	-	-	-
618.7	3LO _{bc}	-	626.9	639.7	3LO _{cs}
-	-	693	700.8	705	2LO _{bc} +LO _{cs}
-	-	777.1	775.1	790.6	LO _{bc} +2LO _{cs}

Table 7.1: Experimentally obtained phonon frequencies and their corresponding assignment, *n* denotes the number of CdS shell layers. The subscripts bc and cs refer to the bare core sample and the core/shell-samples, respectively.

the $\mathbf{p} = 0$ rule and allows contributions besides from the Γ -point. Since the branches in the dispersion relations responsible for the LOs of CdSe and CdS do peak at the Γ -point, their position have to shift to lower wavenumber in the case of the NCs. Using the confinement model as discussed in chapter 6 leads to a theoretical downshift of the CdSe LO of about 7 cm⁻¹ for bare NCs according to ref. [152], which is in reasonable agreement with the data presented here. The effect is partly compensated for the core/shell NCs due to the rising influence of strain inside the NCs.

7.1.1 CdSe/CdS/ZnS core-shell-shell heterostructures

The growth of a further layer of ZnS grown on top of CdSe/CdS NCs results in a graded shell system. ZnS has a lattice parameter of 5.41 Å, which is smaller than the corresponding values for CdSe (6.08 Å) and CdS (5.82 Å). For the investigation of the impact of ZnS, two samples containing this material were investigated. The first is a pure graded shell NC with separated CdS and ZnS shells layers while the

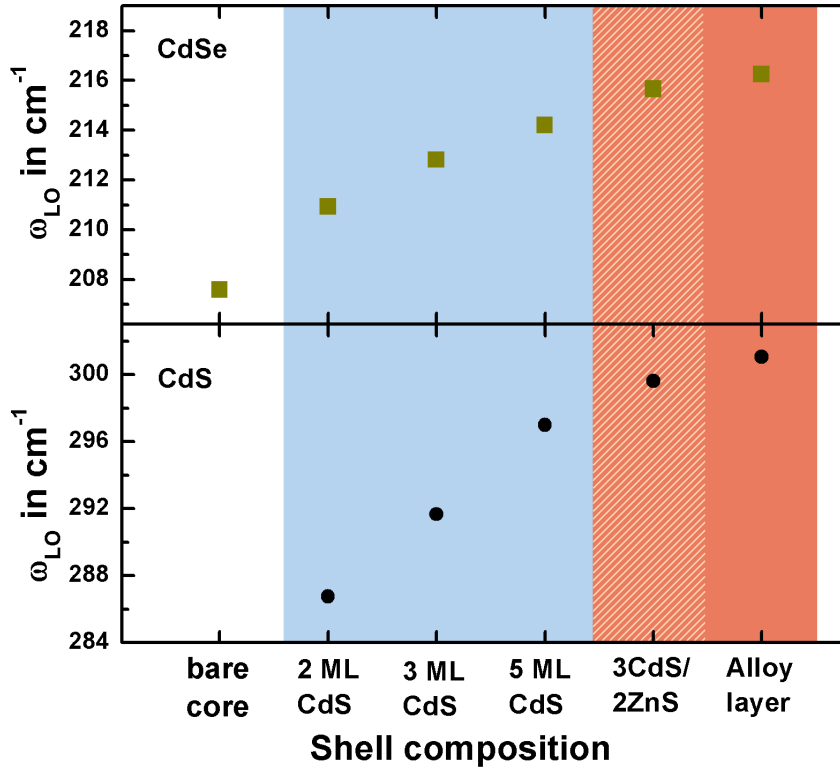


Figure 7.2: Dependency of the CdSe and CdS LO on the sample composition. The blue region corresponds to CdSe/ x CdS samples, the red to the samples containing ZnS.

second involves a buffer layer between the CdS and ZnS shells consisting of CdZnS (see chapter 6 for a description of the samples).

The Raman spectra of these NCs show no additional feature directly related to ZnS. This is caused by the high band-gap energy of ZnS (bulk value 3.6 eV [153]) accompanied by the used wavelength being in near resonance with the CdS and CdSe. The influence of the ZnS can therefore only be derived indirectly from the Raman data.

Figure 7.2 displays the LO phonon frequencies for both observable LOs for all measured NCs. The introduction of ZnS has an impact on both LOs, although the influence on the CdSe LO is only indirect because damped by the CdS. However, since CdS and ZnS both exhibit smaller lattice parameters with respect to CdSe their influence on the CdSe LO is qualitatively similar: the deposition of either materials leads to a compressive strain of the core. Since the lattice mismatch of ZnS with respect to CdSe is larger (11%) as compared to CdS (4.3%) it has a significant impact on the estimated strain values. This is best seen by comparing the sample with a 5 ML CdS shell and the graded shell NC having a 3 ML CdS shell and an

additional 2 ML ZnS capping. While both samples exhibit a 5 ML thick shell and nearly the same diameter ($d_{5CdS}/d_{3CdS/2ZnS} = 97\%$), the induced strain differs significantly (84.4%). This difference can unambiguously be attributed to the impact of the ZnS.

The sample containing the CdZnS alloy layer shows an even stronger increase of the CdSe LO frequency with respect to the bare core. This result is not surprising, since this sample also exhibits the largest amount of shell layers (overall seven layers) investigated in this study. On the other hand, the small absolute positional shift of the CdSe LO with respect to the NC with a 5CdS/2ZnS shell also indicates a level of saturation.

Due to the larger lattice parameter of CdS with respect to ZnS, the coating of the latter will introduce compressive strain to the CdS shell. The CdSe/3CdS and CdSe/3CdS/2ZnS NCs possess the same amount of CdS but their corresponding CdS LO positions differ by 7.9 cm^{-1} (291.7 cm^{-1} and 299.6 cm^{-1} respectively). Al-

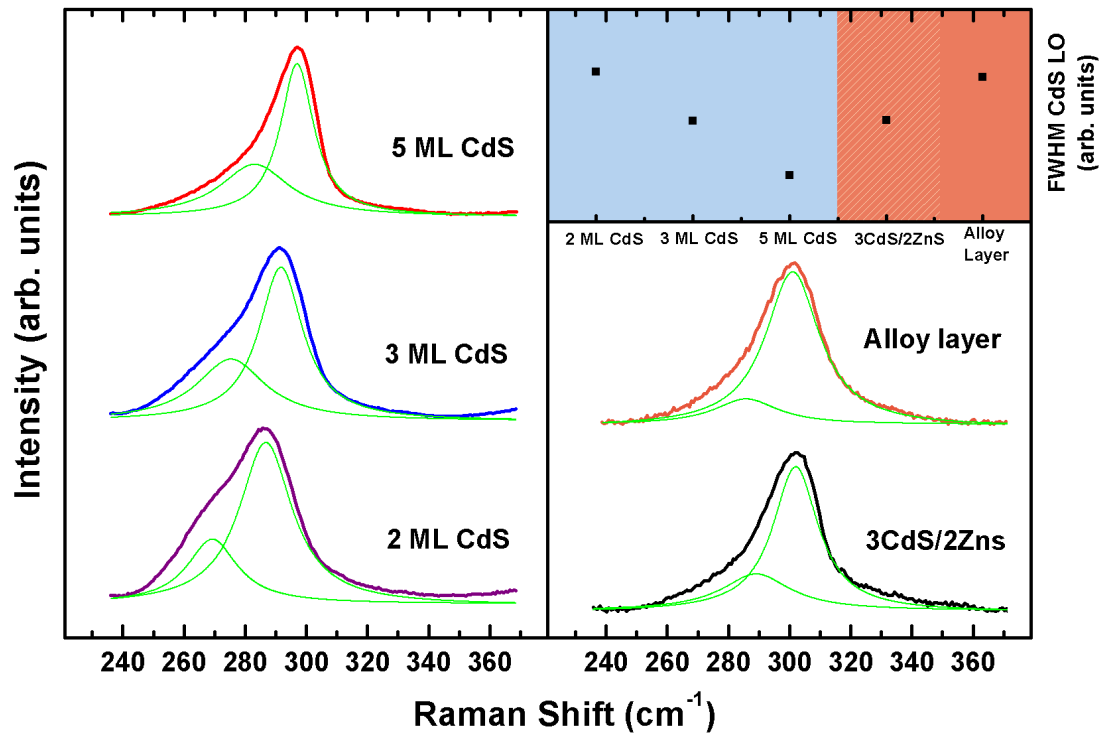


Figure 7.3: Raman spectra of the CdS LO region for all investigated NCs and corresponding Lorentzian fits. The high-energy component corresponds to the CdS LO. The graph in the upper right panel shows the corresponding full width at half maximum (FWHM) of this component.

though the core diameter of the former sample is 4 Å larger and one would thus expect a stronger tensile strain for the CdSe/3CdS NC (as observed), the difference of $\sim 8 \text{ cm}^{-1}$ cannot stem solely from the different core radii but also has to contain compressive strain contributions from the ZnS coating. This is clarified by comparing the samples with either 5 ML CdS and 3ML CdS + 2ML ZnS shell layer composition, since these two possess the same core diameter. Even though the former has to possess a more bulk-like CdS shell the latter exposes the higher LO position as a consequence of strain inside the CdS shell.

In the case of the alloy layer the analysis of the CdS LO position is not conclusive because the measured CdS LO frequency cannot be attributed solely to the CdS shell. Since the alloy layer embeds cadmium and sulfur it is also able to vibrate in a CdS-manner which contributes to the observed signal. Due to the relatively high zinc content and the respective strain in the alloy layer, its corresponding CdS signal is expected to be shifted to higher wavenumbers with respect to the signal stemming from the pure CdS shell. This is confirmed by the analysis of the full width at half maximum (FWHM), since the introduction of ZnS has not only an influence on the position of the CdS shell but also on its FWHM.

The evolution of the CdS FWHM is displayed in Figure 7.3 which also displays the CdS region for all samples, normalized to the CdS LO to emphasize the differences in terms of shape of the different samples. For the CS systems containing only CdS the FWHM decreases linearly with increasing shell thickness. This trend is understood in terms of the formation of a homogeneous shell, becoming more and more similar to bulk CdS. By the addition of ZnS, the CdS layer is constrained between the two materials. Due to the specific lattice mismatches ($a_{CdSe} > a_{CdS} > a_{ZnS}$) the CdS is compressively and tensile strained at the CdSe and ZnS interface regions, respectively. This high gradient of strain inside the CdS shell layer leads to a more heterogeneous shell exhibiting a variety of allowed vibrational frequencies which is responsible for the observed broadening of the CdS LO seen in Fig. 7.3. This enhanced strain will also account for the drop in the PLQY mentioned in chapter 6. The large lattice mismatch of the ZnS leads to stacking faults within the NC. These defects act as trap states leading to non-radiative decay channels for excitons.

7.2 Strain within the CdSe-based nanocrystals

As already shown in chapter 6 by XRD and TEM, strain is present in the observed samples. The amount of strain, however, is not quantitatively recordable using one of these methods, but using the Raman data presented in the last sections gives the opportunity to estimate the amount of strain present in the sample. Since the positions of the CdSe and the CdS LO are sensitive to strain and are,

moreover, clearly visible in the Raman spectra, it is possible to obtain strain values for both, core and shell. As mentioned before, the strain is due to the respective lattice mismatch of the two materials having lattice parameters a of 0.608 and 0.582 nm for the zb-CdSe core and the zb-CdS shell, respectively. This difference leads to changed bond lengths in the CdSe and CdS lattices and results in a compressive strain in the CdSe core and a tensile strain in the CdS shell.

Fig 7.4 and Table 7.1 show the Raman spectra and the LO positions of both materials, CdSe and CdS. Both LOs show an increase of the LO position for thicker shell thicknesses. Qualitatively this increase is explainable in both cases: for the CdSe LO the shift represents the deviation from the relaxed (confined) core. A hydrostatic compression of a lattice leads to a hardening of the phonon frequencies, as observed. Compared to the bulk value of CdS (305 cm^{-1}) the measured LO position shows a softening, which is caused by the tensile character of the strain. Further shell growth leads to the formation of a more homogeneous shell layer which reduces the strain in the shell and finally yields in the shift of the mode towards its bulk value.

The effect of strain on the crystal vibration was first discussed theoretically by Eduard Grüneisen in 1912 within a purely classical approach [154]. Treating vibrations of crystal atoms as undamped harmonic oscillations and evaluating the influence of this motion on neighboring atoms by considering attracting and repelling forces as well as increasing pressures he derived the equation $\gamma = -\frac{\partial(\ln\omega)}{\partial(\ln V)}$ with ω the frequency of the crystal vibration and V the crystal volume. The Grüneisen parameter γ re-

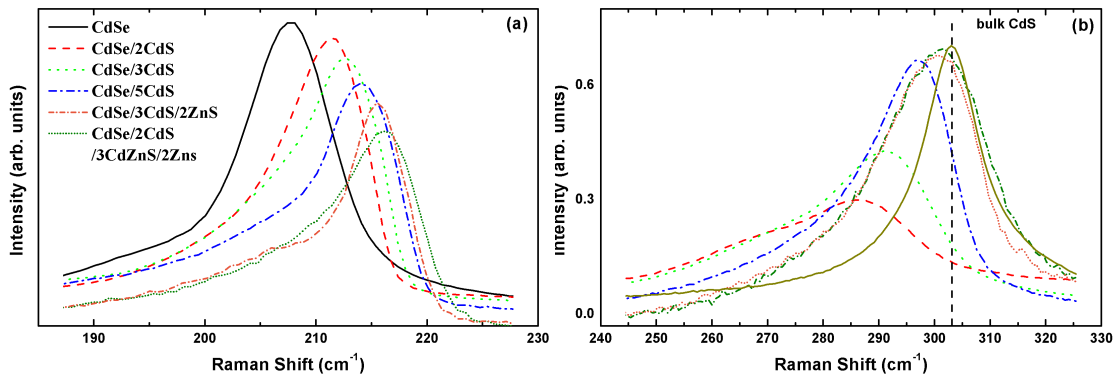


Figure 7.4: (a) Raman spectra of core-shell NCs with different CdS shell thicknesses in the frequency regime of the CdSe LO. The intensities of the spectra are adjusted to emphasize the dependence of the shape on the shell thickness.

(b) Raman spectra of core-shell NCs with different CdS shell thicknesses in the frequency regime of the CdS LO. The spectra are normalized to the CdSe LO and the labeling is as in (a).

lates the effect of the hydrostatic component of the strain to changes of the phonon frequency ω . For the LO phonon of CdSe the Grüneisen parameter is 1.1[155]. The LO frequency shifts and strain are related by

$$\frac{\Delta\omega}{\omega} = \left(1 + 3\frac{\Delta a}{a}\right)^{-\gamma} - 1, \quad (7.1)$$

with a being the lattice parameter and ω the Raman frequency [155, 156]. Measuring the difference of the CdSe LO frequency relative to its frequency in the case of bare nanocrystals (LO position 207.6 cm^{-1}) allows a direct calculation of the strain within the core-shell systems. Evaluating Eq. 7.1 leads to the strain values displayed in Table 7.2. The findings are qualitatively in line with the XRD data. A higher amount of deposited material (either CdS or ZnS) leads to stronger strain within the core which finally results in an increased LO shift.

Figure 7.4(b) displays the CdS LO region for all measured samples and a bulk reference. All spectra are normalized to the CdSe LO to emphasize the differences in intensity. The relative increase in intensity for increasing shell sizes reflects the more pronounced formation of a homogeneous CdS shell layer due to the increased CdS disposal. Using equation (7.1) with a Grüneisen parameter of 1.37[157] and an estimated phonon frequency of 305 cm^{-1} (bulk value) yields strain values as displayed in Table 7.2. The CdS layers are tensily strained in all cases with respect to the bulk value of CdS. For the pure CdSe/CdS NCs the strain of the CdS is markedly reduced with an increasing shell thickness. This result is also in line with the reduction of the FWHM of the band which is explained by the formation of a more and more homogeneous shell. The strain present at the interface is relaxed throughout the enlarged CdS volume and the shell is less strained in total for increasing CdS thicknesses. The strain values for the NCs containing ZnS are even smaller but the CdS band is broadened with respect to the NCs having no ZnS incorporated. As dis-

Shell composition	CdSe LO $\frac{\Delta a}{a}$ in %	CdS LO $\frac{\Delta a}{a}$ in %
2CdS	-0.5	1.4
3CdS	-0.7	0.9
5CdS	-1	0.5
3CdS/2ZnS	-1.1	0.3
2CdS/3CdZnS/2Zns	-1.2	0.2

Table 7.2: Experimental strain values for the CdSe LO and CdS LO. The strain values were estimated using Eq 7.1. The numbers in the shell composition column are the number of monolayers grown on-top of the bare core.

cussed in the last section this broadening reflects a strong strain heterogeneity and since the estimated strain values only reflect an average strain conclusive evidence about the amounts of strain in the CdS shell is not precisely accessible but more a rough estimation for the two Zns-containing samples. This is of course especially true for the sample with the intrinsic grown alloy layer because the observed Raman signal stems from either, the CdS and the CdZnS shell.

7.2.1 Strain calculations

To strengthen the experimental obtained strain values concomitant calculations for the CdSe/CdS NCs were performed by Andrei Schliwa¹ Stress σ_{ij} and strain ϵ_{ij} are generally symmetric second-rank tensors describing the force applied to an elementary solid and the resulting deformation induced by the applied force in the crystal, respectively. The deformation of the crystal can be described by a displacement vector $\vec{u}(\vec{r}) = \vec{r}' - \vec{r}$, with \vec{r} and \vec{r}' being the position of the atoms in the unstrained and strained body, respectively.

The basic assumption to characterize strain within materials is that the present strain depends linearly on the obtained stress for small forces. This linear elasticity prediction has shown good agreement with experimental obtained stress-strain curves for a variety of materials[158]. Therefore, the applied stress is relatable to the strain in the medium as

$$\sigma_{ij} = \sum_{k,l} C_{ijkl} \epsilon_{kl}, \quad (7.2)$$

where C_{ijkl} is the fourth-order stiffness tensor whose components include all material parameters necessary to characterize the material. In general, the stiffness tensor has $9 \times 9 = 81$ components, but using symmetry considerations of the stress and strain tensors as well as the symmetry of cubic crystals equation 7.2 can be written in a matrix format[159] as:

$$\begin{pmatrix} \sigma_x \\ \sigma_y \\ \sigma_z \\ \tau_{xy} \\ \tau_{yz} \\ \tau_{zx} \end{pmatrix} = \begin{pmatrix} C_{11} & C_{12} & C_{12} & 0 & 0 & 0 \\ C_{12} & C_{11} & C_{12} & 0 & 0 & 0 \\ C_{12} & C_{12} & C_{11} & 0 & 0 & 0 \\ 0 & 0 & 0 & \frac{1}{4}C_{44} & 0 & 0 \\ 0 & 0 & 0 & 0 & \frac{1}{4}C_{44} & 0 \\ 0 & 0 & 0 & 0 & 0 & \frac{1}{4}C_{44} \end{pmatrix} \begin{pmatrix} \epsilon_x \\ \epsilon_y \\ \epsilon_z \\ 2\epsilon_{xy} \\ 2\epsilon_{yz} \\ 2\epsilon_{zx} \end{pmatrix}, \quad (7.3)$$

¹Present affiliation: TU Berlin, Germany

with ϵ_i being strain components (the factor 2 arises because of the symmetry of the strain) and σ_i and τ_i denoting the normal and shear stresses, respectively.

To study the evolution of strain inside the CdSe/CdS core-shell system calculations using a 3D continuum mechanical approach were performed. This approach deals with the minimization of the total strain energy present in the observed material. The work done by body forces on or inside an elastic solid is stored in form of strain energy inside the body. The total strain energy U_{TS} does not have to be a linear function of the stresses and strains and it is not possible to apply the principle of superposition to gain the strain energy for a given multidimensional stress[158]. However, since the work does only depend on the final magnitudes of stress and strain and not on the order of loading, the normal and shear stresses can be applied one at a time and produce an additive strain energy U_S for a general state of stress and strain as

$$U_S = \frac{1}{2}(\sigma_x \epsilon_x + \sigma_y \epsilon_y + \sigma_z \epsilon_z + 2\sigma_{xy} \epsilon_{xy} + 2\sigma_{yz} \epsilon_{yz} + 2\sigma_{zx} \epsilon_{zx}) = \frac{1}{2} \sigma_{ij} \epsilon_{ij}, \quad (7.4)$$

The total strain energy U_{TS} stored in an elastic solid occupying a region V is then given by the integration of eq. 7.4 over the region. Using eq. 7.2 this leads to

$$U_{TS} = \frac{1}{2} \int_V \sum_{i,j,k,l} C_{ijkl}(\mathbf{r}) \epsilon_{ij}(\mathbf{r}) \epsilon_{kl}(\mathbf{r}) dV \quad . \quad (7.5)$$

For the obtained calculations eq. 7.5 is minimized for a given three dimensional structure, using finite differences for the strains $\epsilon_{ij} = \partial u_i / \partial x_j$, where \vec{u} is the displacement vector field. This model neglects nonlinear effects as well as plastic deformations, but the reliability of this model even in the nm-scale has been confirmed earlier by Stier and coworker[160]. The compliances C_{ijkl} , represented by the parameters C_{11} , C_{12} and C_{44} for cubic crystals as shown in eq. 7.3, are taken from [161] for CdSe and CdS in the zinc blende phase.

The total diameter of the nanoparticles is fixed at 6.5 nm, with an increasingly thicker CdS shell. The ratio of full diameter - including the shell - by core diameter is thus varied between 1.0 (no shell) and 2.2. This approach is validated although it does not reflect the nearly constant core diameters of the investigated samples[162]. Figure 7.5 shows a scan of the strain components ϵ_{xx} , ϵ_{zz} , and the hydrostatic strain $\epsilon_{\text{hydro}} = \epsilon_{xx} + \epsilon_{yy} + \epsilon_{zz}$ along [100] for three different NCs: Inside the core all components of the strain tensor are below zero meaning they are compressively strained. The situation for the shell is more complex as schematically shown in the sketch of Fig. 7.5. The dotted squares correspond to the unstrained unit cell of CdSe and CdS, respectively. After being coherently strained, the component tangential to the

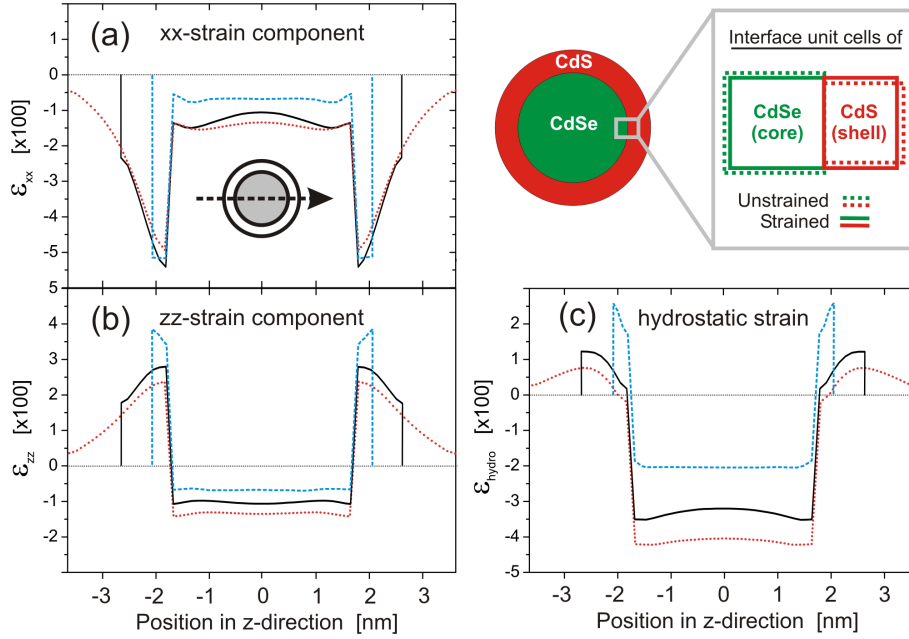


Figure 7.5: Scan of the strain components ϵ_{xx} (a), ϵ_{zz} (b), and the hydrostatic strain $\epsilon_{hydro} = \epsilon_{xx} + \epsilon_{yy} + \epsilon_{zz}$ (c) along [100] for three different shell thicknesses.

The sketch at the upper right side shows the schematics of the strain situation at the core-shell interface. The unstrained unit cells of CdSe and CdS are depicted by dotted squares. After getting coherently strained, the unit cell of CdSe is compressively strained in all three directions, whereas the one of CdS is tensile strained tangential to the interface and compressively in normal direction.

interface, here ϵ_{zz} , increases inside the shell, whereas the normal component, ϵ_{xx} , decreases. In other words the shell is strained compressively in radial direction and tensile tangential to the interface. The overall character of the strain in the shell, however, is given by the hydrostatic component which shows a tensile character for the CdS shell in all cases.

In Figure 7.6 the strain situations inside core and shell are compared to the experimentally derived values for different ratios of total diameter to core diameter of the nanoparticles. Inside the core the compressive nature of the strain is well reproduced by the theory, albeit the experimental values are slightly smaller than the calculated data. This trend increases for thicker CdS-shells. This larger deviation for NC with thicker shells can be caused by an increasing number of stacking faults in those samples which were not considered in the calculations. The number of stacking faults increases for thicker shells and such imperfections lead to a relaxation of the strain in the sample, as observed. On the other hand, a rising number of stacking faults diminish the QY of the NCs which was e.g. shown for CdSe/ZnSe NCs[146]. As shown on page 69 this is not the case for the samples considered in this work, more-

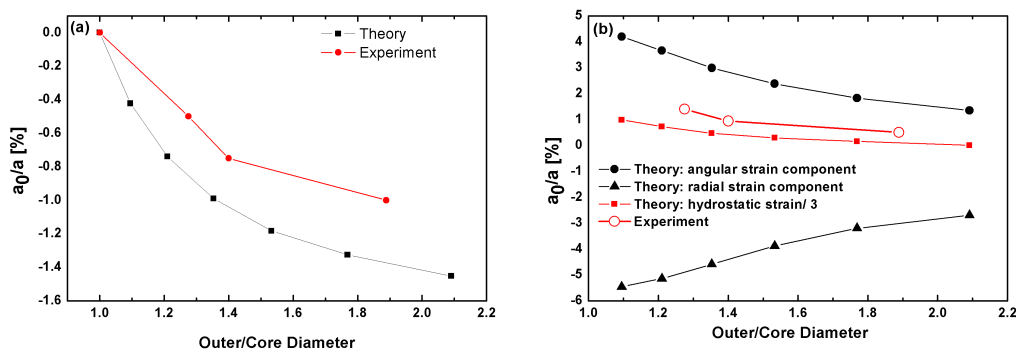


Figure 7.6: (a) Calculated strain, averaged over the core region and the three diagonal components of the strain tensor, compared to the experimentally derived values of the lattice constant change. (b) Angular strain components (tangential to the interface), radial strain components (normal to the interface), hydrostatic strain component and experimental values of the lattice constant change.

over, the QY is still rising for a 5 ML CdS shell. However, this improvement of the QY does not per se rule out the rising amount of dislocations in the system. Since the electron wave function only partly leaks into the shell, the QY improvement can also be attributed to the larger distance of the wave function to the (surface trap states at the) shell boundary. Summarizing, the observed deviation cannot unambiguously be assigned to the number of stacking faults, but since there will be stacking faults present in the sample they will contribute to the observed relaxation of the strain. Other mechanisms explaining the smaller experimental values are the presence of an alloyed interface layer, which would relax the strain inside the core, and/or the fact that the related Raman mode is not completely confined inside the core but spreads partly to the shell region.

The CdS shell features compressive and tensile components within one unit cell. Hence, both components and the hydrostatic component of the strain are plotted in Figure 7.6 (b) compared to the experimentally derived values for the change of the lattice constant. One would expect that the strain, reflected by the measured LO position, is given by the hydrostatic component and albeit an overestimation this view is confirmed as shown in Fig. 7.6 (b). A smaller value than 305 cm^{-1} for ω in eq. 7.1 would result in a better fit of measured and calculated data and such smaller value is reasonable to assume due to the phonon confinement which does reduce the LO frequency in nanosystems[163]. Since no unstrained pure CdS NC sample is considered in this work no realistic value for ω can be derived and the strain values obtained out of the experimental Raman data can only be regarded to be qualitatively.

7.3 Interface composition

The question, whether the interface between two constituents in NCs has a more abrupt or graded character has been raised in literature recently[118, 164]. This question is of special interest since the existence of such an interface alloy layer was linked to observed strong decreases of the Auger recombination rates in CdSe/CdS and CdZnSe/ZnSe NCs. This parameter is crucial since the Auger recombination is a radiationless process derogatory for prospective applications of NCs . Fluorescence line narrowing (FLN) experiments presented by Garcia *et al.*[118] showed the presence of phonon replica interpreted in terms of an alloy layer at the core shell interface. However, the assignment of the CdSe-CdS mixed mode in the PL spectra to an alloy layer is not unambiguous, since 2nd order processes involving phonons of either materials would yield similar energies without the necessity of an alloy layer. This implies that the proposed link between the phonon spectrum and the composition of interfaces in heteronanocrystals remains to be validated.

The complete Raman spectrum of the heteronanocrystals presented in section 7.1 can not be understood by just two materials with a clean and abrupt interface between them. For such a composition one would expect the Raman spectrum to be composed of the prominent fundamental LOs of both materials, their overtones and mixed overtones. Due to the finite size of the QDs the appearance of surface modes is also likely.

All these features are observed in the present Raman spectra, however, besides them two more features, which are not explainable within the above framework, are observed.

The first feature is the low-energy shoulder (LES) of the CdS LO (see Figures 7.1 and 7.3). Such a feature was first observed by Liu et al. in 2007[165]. The authors attributed the feature to be a surface phonon of the shell material, but comparing their spectra with the one presented in this work reveals that the LES is in this case

Shell composition	IP/LO _{CdSe}	SO/LO _{CdSe}	LES/LO _{CdS}
bc	-	0.4	-
2CdS	0.5	0.3	0.5
3CdS	0.9	0.3	0.4
5CdS	0.9	0.5	0.3
3Cds/2ZnS	0.9	0.5	0.2
2CdS/3CdZnS/2Zns	0.8	0.5	0.2

Table 7.3: Intensity ratio of the CdSe SO and the IP mode with respect to the LO. The numbers in the shell composition column are the number of monolayers grown on-top of the bare core (bc).

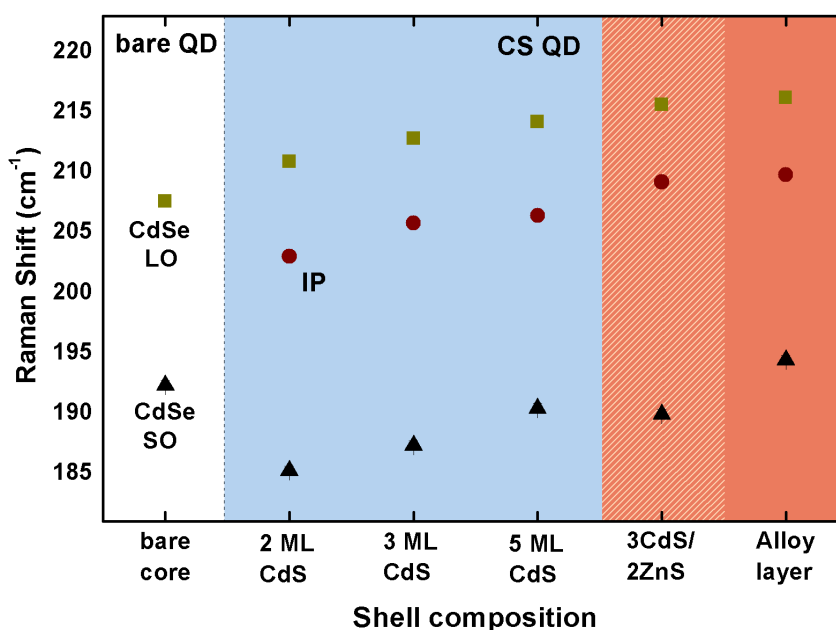


Figure 7.7: Influence of the sample composition on the phonon frequencies of the three components of the CdSe LO band region.

much more pronounced. This is especially true for the sample with the lowest CdS coverage (see Fig. 7.3). The intensity ratio of the LES with respect to the CdS LO (LES/LO-ratio) is given in Table 7.3 and shows that the LES already possesses a high Raman intensity for only modest shell material deposition. The additional deposition of CdS leads to a more pronounced shell layer exhibiting a stronger LO which leads to a decrease of the ratio.

Thus, even if one considers this feature as partly originating from a SO, contributions from other modes are reasonable. Dzhagan *et al.* studied CdSe/ZnS QDs and observed a similar feature around 280 cm^{-1} [166]. Since the observed sample did not contain CdS, the authors related this feature to be CdS-like. In a more recent study, they assigned it to an intermixed layer formed by interdiffusion of sulfur from the shell into the core [166]. The finding of a well-resolved two-mode structure of the band around 300 cm^{-1} clearly support this latter view.

But not only the CdS-related Raman band contains features that can be related to the formation of an alloy layer. With the addition of the CdS shell the shape of the CdSe-related band also undergoes changes. After the coating, only a minimum number of three Lorentzians yield an appropriate fit for the CdSe LO band as shown in Figure 7.1. The three modes correspond to the LO and SO mode of CdSe and an additional third component which is in the following labeled IP (see Table 7.1 for the estimated positions). Previous Raman measurements on CdSe/ZnS nanorods

showed, that the SO shifts to lower wavenumbers after coating as a result of the changed dielectric continuum. This softening is accompanied by an increased distance of the LO and SO position[167]. The same mechanisms will also account for the NCs observed in this study and since only the lowest-energy component exhibits the two mentioned characteristics, it is assigned to be the CdSe SO.

The assignment of the IP is not straightforward. It is only present after the shell growth and can therefore be no intrinsic mode of CdSe. One could assign this mode to be an intrinsic mode of CdS. The only Raman-active mode of CdS in the energetic vicinity of the CdSe LO band is a multiphonon mode located at 207 cm^{-1} [168]. However, this assignment is not likely since this mode is suppressed in nanomaterials[163, 169, 170].

The frequency dependence of the IP on the shell thickness is shown in Figure 7.7 together with the dependencies of the LO and SO. The IP mode behaves similar to the CdSe LO, showing a systematic increase for thicker shell coverages.

The intensity evolution of the mode is best expressed in terms of its intensity ratio with respect to the CdSe LO, since the intensity of the latter can be considered to remain constant with the shell growth. The ratio is listed in Table 7.3 together with the intensity ratio of the CdSe SO/LO. Within the limit of error, a saturation for CdS coverages of 3 ML and above is seen and only for a moderate coverage of 2 ML CdS a significantly smaller value is obtained. The SO/LO ratio on the other hand shows no considerable changes.

As shown in section 7.2 the hardening of the LO phonon reflects the increasing strain within the CdSe core. Accordingly, the IP can be related to a CdSe-containing region within the NCs exhibiting a different, smaller, amount of strain. Within an hypothetical $\text{CdSe}_{1-x}\text{S}_x$ alloy layer located at the CdSe/CdS interface, the sulfur fraction would lead to a relaxation of the compressed CdSe lattice. This relaxation would result in a softening of the LO stemming from this region with respect to the LO of the CdSe core and would itself manifest in a mode at the low-energy side of the CdSe LO, like seen for the IP. Furthermore, since the growth rate of such a layer is limited by the area of the interface and less by the amount of deposited shell material, the intensity stemming from such a layer is not expected to increase continuously, but to saturate at a specific stage. This is exactly what is observed for a coverage around 3 ML.

If one addresses such an interface layer being present in the observed samples one would also expect a signal relating to the CdS fraction within the interface layer as observed in the past for pure $\text{CdSe}_{1-x}\text{S}_x$ crystals[171]. With respect to the pure CdS-shell signal this signal has to be softened due to the stronger tensile strain within the alloy layer. The observed LES is exactly located where one would expect such signal.

The appearance of the IP band as well as the strong signal of the LES cannot be explained within the framework of a pure core-shell structure. Therefore the for-

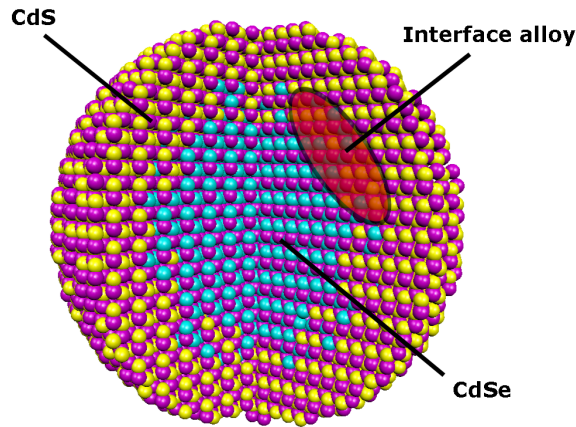


Figure 7.8: Schematic sketch of a CdSe/CdS QD without considering any strain. The CdSe core, CdS shell as well as the $\text{CdSe}_{1-x}\text{S}_x$ -interface alloy layer are indicated.

mation of a core-alloyed interface-shell structure like sketched in Fig. 7.8 is highly likely. Both, the IP and the LES are in this picture phonon modes relatable to this interface region.

7.4 Exciton-phonon coupling

One of the important characteristics of bulk and nano-sized systems is the interaction strength between excitons and phonons, the exciton-phonon coupling. For optical applications a low coupling of the excited electrons and holes to the phonons is favorable to sustain as much oscillator strength of a given electronic transition in the NC as possible. The interaction *via* exciton-phonon coupling leads to a spectral broadening and has a negative influence on properties like the transport and energy relaxation rate of excited carriers.

In bulk cubic and hexagonal II-VI semiconductors, the excited electron is due to the polar nature of the material most strongly coupled to the LO phonons *via* the Fröhlich interaction[172]. A vibrational excitation of the crystal leads in polar materials to the formation of intrinsic electric fields. The electrons and holes of the crystal atoms will interact with this electric fields and mathematically, this exciton-phonon-coupling is described by the Fröhlich interaction [173]. According to Fröhlich, the exciton-phonon coupling is a dipole-dipole interaction with a range of up to 10 nm. It depends exclusively on the strength of the induced electric field and the ion displacement.

The strength of this coupling reflects itself in the relative intensities of the overtones to the fundamental Raman bands, the 2LO/LO-ratio [174]. The exciton-phonon

coupling strength is characterized by the Huang-Rhys parameter S , which is defined as

$$S = (1/2)\Delta_s^2. \quad (7.6)$$

Δ_s is the displacement of the excited-state equilibrium position relative to the ground state and reflects the overlap of the harmonic wave functions as depicted in Fig. 2.1 in chapter 2 on page 10. It is an important parameter to calculate the Frank-Condon integrals which can be described in the framework of Albrecht[17] involving harmonic oscillator wave functions and standard algebra as

$$\langle n|m \rangle = \left(\frac{n!}{m!}\right)^{1/2} \exp\left(-\frac{\Delta_s^2}{2}\right) \Delta_s^{n-m} L_m^{n-m}(\Delta_s^2), \quad (7.7)$$

with L being the Laguerre polynomial. As mentioned, the overlap integrals are according to Albrecht and Merlin[175] needed to calculate the Raman scattering cross section which can be written for an n -phonon process in the form

$$|R^n(\omega)|^2 = \mu^4 \sum_{m=0}^{\infty} \frac{\langle n|m \rangle \langle m|0 \rangle}{|E_{ij} + n\hbar\omega_{LO} - \hbar\omega + i\hbar\Gamma|^2}. \quad (7.8)$$

E_{ij} is hereby the excited state energy, n and m are the involved intermediate vibrational levels, $\hbar\omega$ is the incident photon energy, Γ is the linewidth and μ the electronic transition dipole moment.

The cross sections can be obtained from fitting the Raman spectra and are represented by the area of the corresponding Lorentzian functions. By measuring the fundamental Raman band ($n = 1$), an overtone ($n = 2$) and using the equations 7.8 and 7.7 it is possible to numerically estimate values for Δ_s and S . Figure 7.9 displays the dependency of the Huang-Rhys parameter on the ratio of the first overtone to the fundamental Raman band I_{2LO}/I_{LO} .

The Huang-Rhys parameter of the bare NCs is obtained to be 0.04. The value of the Huang-Rhys parameter of bulk CdSe varies in literature. Alivisatos et al.[155] calculated S using

$$\Delta_s = 1.97 \frac{e^2}{a_0 \hbar \omega_{LO}} \left(\frac{1}{\epsilon_\infty} \frac{1}{\epsilon_0} \right) \frac{1}{\omega} \times \int_0^\omega x^4 (2+x^2)^2 (1+x^2)^{-4} dx, \quad (7.9)$$

with a_0 being the lattice parameter and ϵ_∞ and ϵ_0 the low and high frequency dielectric constants. ω is defined as $(3\pi^2)^{(1/3)} a_0/a_b$, with a_b denoting the exciton Bohr radius. They evaluated a value of $S \approx 4.5$.

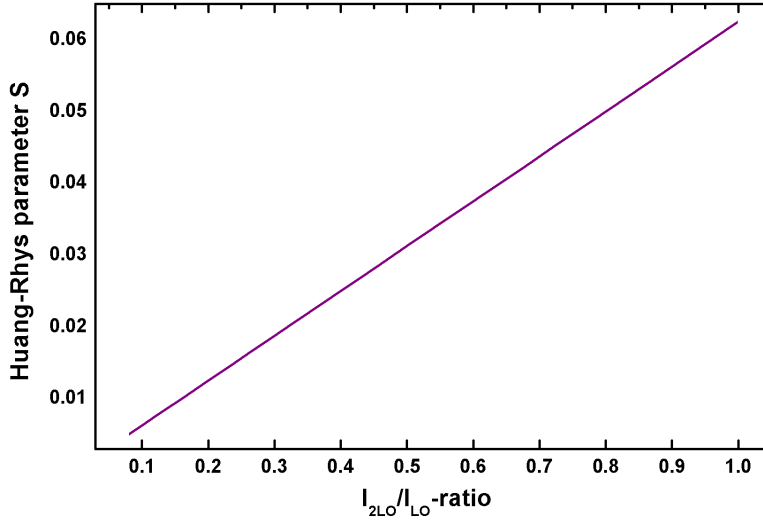


Figure 7.9: Huang-Rhys parameter versus ratio of the integrated intensities of second order and fundamental Raman band.

Nomura et al.[176] on the other hand calculated values the coupling strength using a hydrogen-like wave function for a Wannier-exciton in bulk semiconductors. This leads to the expression

$$S = \frac{f_0^2}{32\pi^2 a_b (\hbar\omega_{LO})^2} \times \frac{(m_1^* - m_2^*)^2 (5m_1^{*2} + 14m_1^*m_2^* + 5m_2^{*2})}{m_1^*m_2^* (m_1^* + m_2^*)^2}. \quad (7.10)$$

f_0 hereby is the Fröhlich interaction coupling constant and m_1^* and m_2^* are the effective masses of an electron and a hole. Assuming different effective masses the authors calculated values for S ranging from 0.38 to 1.4.

Despite this impreciseness, the measured value of 0.04 for the bare NCs is still one to two orders of magnitudes smaller and in line with recent experimental works in literature [166, 177, 178].

The coupling strength depends on the difference of the wave functions of electron and hole. For bulk material, electron and hole posses different effective masses resulting in different extents of the wave functions within the crystal. These extents couple to the wave function of the LO phonons resulting in a net-coupling. The difference of the measured values with respect to the bulk material stems from the confinement of the wave functions within the NCs. For NCs, the difference of the effective masses becomes smaller due to the confinement and the overlap of the wave

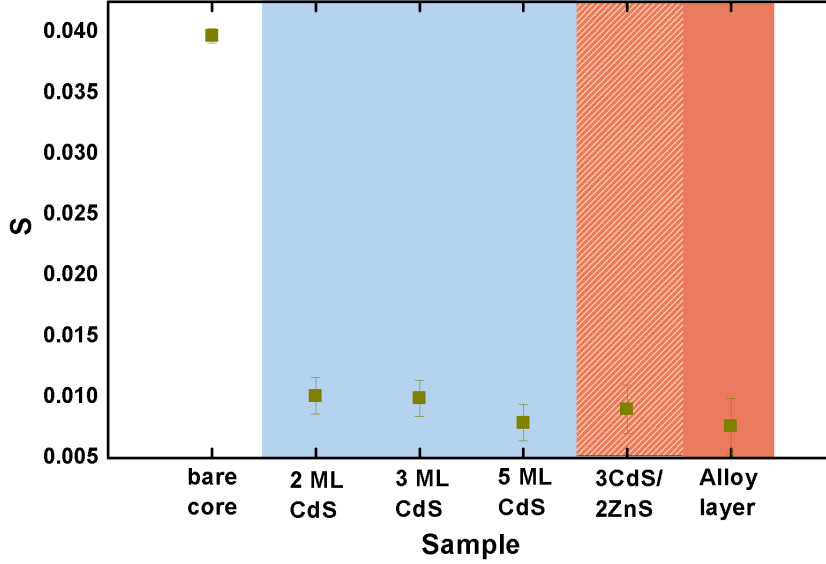


Figure 7.10: Experimentally estimated Huang-Rhys factors of the investigated samples.

functions becomes larger, which finally leads to the observed decrease of the Huang-Rhys parameter[176, 179].

The dependency of the Huang-Rhys factor S on the shell composition is shown in Fig. 7.10 and the estimated values are displayed in Table 7.4. S shows a strong sensitivity on the pure existence of a shell, even a minor coverage leads to a strong decrease of the Huang-Rhys parameter. S is reduced by at least 75 % and changes from a value of 0.04 for bare CdSe NCs to values between 0.008 and 0.01 for coated ones. This quenching of the exciton-phonon-coupling for coated NCs can be attributed to the leakage of the exciton wave function into the shell. The exciton wave function does partly expand into the shell due to the expansion of the wave function

Shell composition	LO area (arb. u.)	2LO area (arb. u.)	I_{2LO}/I_{LO}	S
bare core	13.98	8.88	0.635	0.04
2CdS	9.85	1.6	0.162	0.010
3CdS	7.67	1.16	0.151	0.009
5CdS	8.95	1.14	0.127	0.008
3CdS/2ZnS	8.59	1.32	0.154	0.009
2CdS/3CdZnS/2ZnS	13.15	1.61	0.122	0.008

Table 7.4: Experimental obtained intensity values for the fundamental and first overtone of the CdSe LO and their related Huang-Rhys parameter S .

of the electron[180]. Since the CdSe LO phonon wave function is mainly localized in the core, the reduced overlap of the wave functions of the exciton and the CdSe LO phonon leads to the weaker coupling strength seen in Fig. 7.10[166].

For pure CdSe/ZnS this effect should be less pronounced since the leakage of the electron wave function in those type of systems is less pronounced due to the larger bandgap of ZnS[5, 181]. Experimental estimated values for Huang-Rhys parameter, however, are rare for CdSe/ZnS NCs. Baranov *et al.*[182] measured a Huang-Rhys factor of 0.2 for a CdSe core having a shell of 3.4 ML of ZnS. Lange *et al.*[177] worked on nanorods and estimated S factors between 0.036 and 0.053. Although the authors worked on nanorods they showed their results are in general comparable to spherical systems since the exciton wave function is highly sensitive on the diameter and not on the length of the rods. All values are one order of magnitude larger than the values presented here, encouraging the assumption that the leakage of the electron wave function is responsible for the decreasing S values in case of CdSe/CdS systems.

A subsequent mechanism in decreasing S is the increasing coupling between the exciton and shell-related phonons. This coupling becomes more likely for thicker shells[183] and is also reflected by the values given in Fig. 7.10 being in general smaller for a larger amount of deposited shell material.

In this chapter the vibrational spectrum of CdSe-based core-shell NCs was investigated. All Raman modes were assigned and the strain present in core-shell systems was evaluated by the analysis of the shifting of the LO bands of the involved materials. An interfacial layer consisting out of $\text{CdSe}_{1-x}\text{S}_x$ is highly likely in those systems which could be shown by relating two features in the Raman spectra to this alloy layer. The exciton-phonon coupling is much lower in the NCs than in bulk material due to the spatial confinement of the electron and hole wave functions in the NC. This effect is further increased by coating the NCs with additional CdS and ZnS shells.

Chapter 8

Summary

In this work Raman spectroscopy was utilized to determine the origin of the wavelength-dependent shift of the ν_1 -envelope of β -carotene in different environments as well as the influence of incorporated β -carotene on the properties of carbon nanotubes. Furthermore, the evolution of strain inside CdSe-based nanocrystals was investigated. The existence of an interface alloy layer was proposed and the exciton-phonon coupling strength in those systems was determined.

The Raman spectrum of β -carotene is dominated by three strong Raman bands. The position of the most intense of those bands (the ν_1 -band) exhibits an uncommon dependency on the excitation wavelength. The ν_1 -band is a composition of two submodes, which was revealed experimentally and theoretically in this work. Thus, the origin of the mentioned shift has to be attributed to the different resonance behavior of the two submodes. Measurements on photosystem I and II proofed the existence of the effect in the proteins too. This result is in particular relevant since it contradicts former studies in which the shift of the band was proposed to be a fingerprint for the existence of different carotene pools within the two photosystems. Due to the performed DFT calculations different Frank-Condon or Herzberg-Teller-enhancement of the two submodes can be ruled out as the origin of the shift. The most probable origin of the observed shifting is an involvement of the Dushinsky rotation, which was neglected in the performed calculations.

Also the influence of incorporated β -carotene inside carbon nanotubes was investigated. PLE and absorbance studies by Yanagi *et al* indicate that encapsulated β -carotene transfers photoexcitation energy to the SWCNT[100]. This observation could open the door for the fine-tuning of the optical properties of SWCNTs *via* encapsulation of various molecules. Especially, the complete integrity of the CNTs and the β -carotene after the incorporation makes this approach interesting for fur-

ther industrial implementations. The endohedral functionalization has only slight impact on the changes on the vibrational properties of either materials which could be shown in this work. The vibronic properties of the host molecule show a decrease in intensity due to the incorporated β -carotene, the resonance energy of the E_{22} transition of the nanotube shows a slight blueshifted by at most 20 meV. The Raman spectra indicate a twisted conformation of the embedded carotene molecules within the nanotubes. More important, the presented results also suggest a selective degree of functionalization depending on the diameter of the tubes. The facts, that optical properties of the nanotubes can be tuned by functionalization and that the influence of the incorporation on the physical properties is rather low eases the industrial implementation of that material system.

In the 2nd part of this work the strain present in CdSe-based core-shell nanocrystals was investigated experimentally and theoretically. As shell constituents CdS and ZnS were used. An initial shell of two monolayers of CdS strains the CdSe core significantly and further layers gradually increase the compressive strain. The shell is tensile strained. Increasing the shell thickness leads to a relaxation and net reduction of the tensile strain within the shell.

The introduction of ZnS as a second shell material leads to a further compression of the core while the FWHM of the CdS LO shows a broadening suggesting a strong gradient of strain within the CdS shell: at the CdSe/CdS-interface the CdS is strained tensile while it is strained compressive at the CdS/ZnS-interface. The synthesis of a buffer layer consisting of CdZnS between the CdS and ZnS shells shows no relaxation of the strain within the core.

A detailed analysis of the Raman spectra of CdSe/CdS nanocrystals having different shell thicknesses reveals two features that are best explained by the formation of an alloyed interface between core and shell. These findings are also in line with strain values obtained by Raman spectroscopy and those from 3D continuum mechanical calculations. Thus a drift of anions and the formation of an alloyed interface layer is highly probable. Since the alloyed interface has a distinct Raman fingerprint, this work provides the basis for an extended study of interfacial alloying in CdSe/CdS or similar core/shell systems like CdZnSe/ZnSe[164]. In particular, the combination of *ab-initio* density functional theory calculations of the vibrational properties of Cd(Se,S) alloys with (non-destructive) Raman measurements could allow a detailed understanding of these nanoscale interfaces, which is out of reach of other methods like, *e.g.*, TEM.

In agreement with recent literature it could be shown, that the electron-phonon coupling, which can be obtained from Raman spectra, is strongly diminished in nanocrystals. The obtained values for all nanocrystals investigated in this work are more than one order of magnitude smaller in comparison with bulk material. This

effect is relatable to the decreasing influence of the Coulomb interaction due to the phonon confinement. This trend increases for the core-shell nanocrystals showing an even more decreasing electron-phonon coupling due to the extension of the electron wavefunction into the shell reducing the coupling to the CdSe LO which is mainly located in the core region.

In conclusion, Raman spectroscopy is a versatile, non-destructive method to obtain information on colloidal nanocrystals and it will help in the characterization and concomitant optimization of novel nanocrystal heterostructures in the future.

Bibliography

- [1] F. Muh and A. Zouni, *Frontiers in Bioscience* **16**, 3072 (2011).
- [2] P. Jensen, R. Bassi, E. Boekema, J. Dekker, S. Jansson, D. Leister, C. Robinson, and H. Scheller, *Biochimica et Biophysica Acta* **1767**, 335 (2007).
- [3] A. Telfer, *Phil. Trans. R. Soc. Lond. B* **356**, 1431 (2002).
- [4] Y. Yin and P. Alivisatos, *Nature* **437**, 664 (2005).
- [5] P. Reiss, M. Protiere, L. Li, P. Reiss, M. Protiere, and L. Li, *SMALL* **2009**, 154 (5).
- [6] L. Brus, *J. Phys. Chem.* **80**, 4403 (1984).
- [7] Z. Hens, D. Vanmaekelbergh, E. Stoffels, and H. van Kempen, *PRL* **88**, 236803 (2002).
- [8] P. Anikeeva, J. Halpert, M. Bawendi, and V. Bulovic, *Nano Letters* **9**, 2532 (2009).
- [9] P. Kamat, K. Tvrdy, D. Baker, and J. Radich, *Chem. Rev.* **110**, 6664 (2010).
- [10] Y.-L. Lee and Y. Lo, *Adv. Funct. Mater.* **19**, 604 (2009).
- [11] K. Riehemann, S. Schneider, T. Luger, B. Godin, M. Ferrari, and H. Fuchs, *Angew. Chem. Int. Ed.* **48**, 872 (2009).
- [12] X. Gao, Y. Cui, R. Levenson, L. Chung, and S. Nie, *Nature Biotechnology* **22**, 969 (2004).
- [13] J. Barreto, W. O'Malley, M. Kubeil, B. Graham, H. Stephan, and L. Spiccia, *Adv. Mater.* **23** (2011).
- [14] C. Raman, *Nature* **619**, 502 (1928).
- [15] C. Raman, *Nature* **619**, 121 (1928).

BIBLIOGRAPHY

- [16] G. Placzek, *Rayleigh-Streuung und Raman Effekt* (Akademische Verlagsgesellschaft, Leipzig, 1934).
- [17] A. Albrecht, *Jour. Chem. Phys.* **34**, 1476 (1961).
- [18] E. I. Solomon and A. Lever, *Inorganic Electronic Structure and Spectroscopy, Vol. 1: Methodology* (John Wiley & Sons: New York, 1999), chap. 3.2, pp. 383 – 389.
- [19] H. Telg, Ph.D. thesis, TU Berlin (2009).
- [20] P. Kusch, H. Lange, M. Artemyev, and C. Thomsen, *Solid State Communications* **151**, 67 (2011).
- [21] P. Karrer, A. Helfenstein, H. Wehrli, and A. Wettstein, *Helvetica Chimica Acta* **13**, 1084 (1930).
- [22] G. Wittig and H. Pommer, *Chem. Abstr.* **53** (1959).
- [23] L. Taiz and E. Zeiger, *Plant Physiology, Palgrave Macmillan; 4th rev. ed.* (2006).
- [24] B. Ke, *Photosynthesis-photobiochemistry and photobiophysics, Kluwer Academic Publishers, Dordrecht, 2001, vol. 10.* (2006).
- [25] J. H. Golbeck and D. A. Bryant, in: *Photosystem I: Current Topics in Bioenergetics*, edited by C. P. Lee (Academic Press, New York), p. 83. (1991).
- [26] H. Dau and K. Sauer, *Biochim. Biophys. Acta* **1273**, 175 (1996).
- [27] J. McEvoy and G. Brudvig, *Chem. Reviews* **106**, 4455 (2006).
- [28] P. Colman, H. Freeman, J. Guss, M. Murata, V. Norris, J. Ramshaw, and M. Venkatappa, *Nature* **272**, 319 (1978).
- [29] E. Albarran-Zavala and F. Angulo-Brown, *entropy* **9** (2007).
- [30] P. Jordan, P. Fromme, H. Witt, O. Klukas, W. Saenger, and N. Krauss, *Nature* **411**, 909 (2001).
- [31] A. Guskov, J. Kern, A. Gabdulkhakov, M. Broser, A. Zouni, and W. Saenger, *Nature Structural Molecular Biology* **16**, 334 (2009).
- [32] A. Ben-Shem, F. Frolow, and N. Nelson, *Nature* **426**, 630 (2003).
- [33] M. Hippler, J. Reichert, M. Sutter, E. Zak, L. Altschmied, U. Schröer, R. G. Hermann, and W. Haehnel, *EMBO Journal* **15**, 6374 (1996).

- [34] N. Nelson and C. Yocum, *Annu. Rev. Plant Biol.* **57**, 521 (2006).
- [35] L. Krabben, E. Schlodder, R. Jordan, D. Carbonera, G. Giacometti, H. Lee, A. Webber, and W. Lubitz, *Biochemistry* **39**, 13012 (2000).
- [36] B. Loll, J. Kern, W. Saenger, A. Zouni, and J. Biesiadka, *Nature* **438**, 1040 (2005).
- [37] H. Frank and G. Brudvig, *Biochemistry* **43**, 8607 (2004).
- [38] B. Hillmann and E. Schlodder, *Biochimica et Biophysica Acta* **1231**, 76 (1995).
- [39] C. C. Moser and P. L. Dutton, *Biochimica et Biophysica Acta* **1101**, 171 (1992).
- [40] B. Kok, B. Forbush, and M. McGloin, *Photochemistry and Photobiology* **11**, 457 (1970).
- [41] K. Ferreira, T. Iverson, K. Maghlaoui, J. Barber, and S. Iwata, *Science* **303**, 1831 (2004).
- [42] J. Barber, *Chem. Soc. Rev.* **39**, 185 (2009).
- [43] N. Nelson and A. Ben-Shem, *Nat. Rev. Mol. Cell Biol.* **5**, 971 (2004).
- [44] F. Inagaki, M. Tasumi, and T. Miyazawa, *J. Raman Spectrosc.* **3**, 335 (1975).
- [45] M. Sugisaki, K. Yanagi, R. Cogdell, and H. Hashimoto, *J. Raman Spectrosc.* **3**, 325 (1975).
- [46] H. Studier, Ph.D. thesis, Freie Universität Berlin (2007).
- [47] P. Horton and A. Ruban, *J. Exp. Bot.* **56**, 365 (2005).
- [48] G. N. Johnson, *J. Exp. Bot.* **56**, 407 (2004).
- [49] C. A. Tracewell, J. S. Vrettos, J. A. Bautista, H. A. Frank, and G. W. Brudvig, *Arch. Biochem. Biophys.* **385**, 61 (2001).
- [50] A. Telfer, *Photochem. Photobiol. Sci.* **4**, 950 (2005).
- [51] R. J. Cogdell and H. A. Frank, *Biochim. Biophys. Acta* **895**, 63 (1987).
- [52] H. T. Witt, *Quarterly Reviews of Biophysics* **4**, 365 (1971).

BIBLIOGRAPHY

- [53] T. Tomo, M. Mimuro, M. Iwaki, M. Kobayashi, S. Itoh, and K. Satoh, *Biochimica et Biophysica Acta* **1321**, 21 (1997).
- [54] Y. Takahashi, O. Hansson, P. Mathis, and K. Satoh, *Biochimica et Biophysica Acta* **893**, 49 (1987).
- [55] A. Teller, J. D. L. Rivas, and J. Barber, *Biochim. Biophys. Acta* **1060**, 106 (1991).
- [56] A. Telfer, S. Dhimi, S. M. Bishop, D. Phillips, and J. Barber, *Biochemistry* **33**, 14469 (1994).
- [57] F. Rappaport, M. Guergova-Kuras, P. J. Nixon, B. A. Diner, and J. Lavergne, *Biochemistry* **41**, 8518 (2002).
- [58] F. Inagaki, M. Tasumi, and T. Miyazawa, *J. Mol. Spectrosc.* **50**, 286 (1974).
- [59] S. Saito, M. Tasumi, and C. Eugster, *Journal of Raman spectroscopy* **14**, 299 (1983).
- [60] Y. Koyama, I. Takatsuka, M. Nakata, and M. Tasumi, *Journal of Raman spectroscopy* **19**, 37 (1988).
- [61] S. Schlücker, A. Szeghalmi, M. Schmitt, J. Popp, and W. Kiefer, *J. Raman Spectrosc.* **34**, 413 (2003).
- [62] A. Telfer, D. Frolov, J. Barber, B. Robert, and A. Pascal, *Biochemistry* **42**, 1008 (2003).
- [63] R. van Dorssen, J. Breton, J. Plijter, K. Satoh, H. van Gorkom, and J. Amersz, *Biochimica et Biophysica Acta* **893**, 267 (1987).
- [64] M. J. Frisch, G. W. Trucks, H. B. Schlegel, G. E. Scuseria, M. A. Robb, J. R. Cheeseman, J. A. Montgomery, Jr., T. Vreven, K. N. Kudin, et al., Inc., Wallingford, CT **19** (2004).
- [65] R. Ahlrichs, M. Bär, M. Haser, H. Horn, and C. Kölmel, *Chem. Phys. Lett.* **162**, 165 (1989).
- [66] P. Hariharan and J. Pole, *Theoret. chim. Acta* **28**, 213 (1973).
- [67] P. H. Stephens, F. J. Devlin, C. F. Chabalowski, and M. J. Frisch, *J. Phys. Chem.* **98**, 11623 (1994).
- [68] I. Magdo, K. Nemeth, F. Mark, P. Hildebrandt, and K. Schaffner, *J. Phys. Chem.* **103**, 289 (1999).

- [69] M. A. Mroginski, D. H. Murgida, and P. Hildebrandt, *J. Phys. Chem. A* **110**, 10564 (2006).
- [70] M. O. Senge, H. Hope, and K. M. Smith, *Z. Naturforsch. C* **47**, 474 (1992).
- [71] A. Requena, J. P. Ceron-Carrasco, A. Bastida, J. Zuniga, and B. Miguel, *J. Phys. Chem. A* **112**, 4815 (2008).
- [72] W. Peticolas and T. Rush, *Journal of Computational Chemistry* **18**, 1261 (1995).
- [73] T. Rush and W. Peticolas, *J. Phys. Chem.* **99**, 14647 (1995).
- [74] I. Tehver, H. Kaasik, and V. Hizhnyakov, *J. Raman Spectrosc.* **33**, 639 (2002).
- [75] P. M. Champion and A. C. Albrecht, *Annu. Rev. Phys. Chem.* **33**, 353 (1982).
- [76] T. G. Spiro and P. Stein, *Annu. Rev. Phys. Chem.* **28**, 501 (1977).
- [77] B. P. Gaber, V. Miskowski, and T. G. Spiro, *J. Am. Chem. Soc.* **96**, 6868 (1974).
- [78] J. Kern, B. Loll, C. Lueneberg, D. DiFore, J. Biesiadka, K. Irrgang, and A. Zouni, *Biochim. Biophys. Acta, Bioenerg.* **1706** (2005).
- [79] P. Fromme and H. Witt, *Biochim. Biophys. Acta, Bioenerg.* **1365** (1998).
- [80] T. Noguchi, H. Hayashi, M. Tasumi, and G. H. Atkinson, *J. Phys. Chem.* **95**, 3167 (1991).
- [81] S. Ijima, *Nature* **354**, 56 (1991).
- [82] S. Reich, C. Thomsen, and J. Maultzsch, *Carbon Nanotubes - Basic Concepts and Physical Properties* (Wiley-VCH, Berlin, 2004).
- [83] R. Krupke, F. Hennrich, and H.v.Löhneysen, *Science* **301**, 344 (2003).
- [84] A. A. Green, M. C. Duch, and M. C. Hersam, *Nano Res* **2**, 69 (2009).
- [85] T. Durkop, B. M. Kim, and M. S. Fuhrer, *J. Phys.: Condens. Matter* **16**, R553 (2004).
- [86] M. Holzinger, O. Vostrowsky, A. Hirsch, F. Hennrich, M. Kappes, R. Weiss, and F. Jellen, *Angew. Chem. Int. Ed.* **40**, 4002 (2001).
- [87] R. Graupner, J. Abraham, D. Wunderlich, A. Vencelova, P. Lauffer, J. Rohrl, M. Hundhausen, L. Ley, and A. Hirsch, *J. Am. Chem. Soc.* **128**, 6683 (2006).

BIBLIOGRAPHY

- [88] T. Takenobu, T. Takano, M. Shiraishi, Y. Murakami, M. Ata, H. Kataura, Y. Achiba, and Y. Iwasa, *Nature Mater.* **2**, 683 (2003).
- [89] B. Smith, M. Monthieux, and D. Luzzi, *Nature* **396**, 323 (1998).
- [90] S.-K. Joung, T. Okazaki, N. Kishi, S. Okada, S. Bandow, and S. Iijima, *Phys. Rev. Lett.* **103**, 027403 (2009).
- [91] S. Bandow, M. Takizawa, H. Kato, T. Okazaki, Shinohara, and S. Iijima, *Chem. Phys. Lett.* **347**, 23 (2001).
- [92] K. Yanagi, Y. Miyata, and H. Kataura, *Adv. Mater.* **18**, 437 (2006).
- [93] K. Abe, D. Kosumi, K. Yanagi, Y. Miyata, H. Kataura, and M. Yoshizawa, *Phys. Rev. B* **77**, 165436 (2008).
- [94] K. Yanagi, K. Iakoubovskii, S. Kazaoui, N. Minami, Y. Maniwa, Y. Miyata, and H. Kataura, *Phys. Rev. B* **74**, 155420 (2006).
- [95] Y. Saito, K. Yanagi, N. Hayazawa, H. Ishitobi, A. u. Ono, H. Kataura, and S. Kawata, *Japanese J. Appl. Phys.* **45**, 9286 (2006).
- [96] C. Thomsen and S. Reich, *Phys. Rev. Lett.* **85**, 5214 (2000).
- [97] A. Jorio, C. Fantini, M. S. S. Dantas, M. A. Pimenta, A. G. S. Filho, G. G. Samsonidze, V. W. Brar, G. Dresselhaus, M. S. Dresselhaus, A. K. Swan, et al., *Phys. Rev.* **66**, 115411 (2002).
- [98] O. Dubay, G. Kresse, and H. Kuzmany, *Phys. Rev. Lett.* **88**, 235506 (2002).
- [99] H. Telg, J. Maultzsch, S. Reich, F. Hennrich, and C. Thomsen, *Phys. Rev. Lett.* **93**, 177401 (2004).
- [100] K. Yanagi, K. Iakoubovskii, S. Kazaoui, N. Minami, Y. Maniwa, Y. Miyata, and H. Kataura, *Phys Rev. B.* **74**, 155420 (2006).
- [101] Y. Wang, K. Kempa, B. Kimball, J. B. Carlson, G. Benham, W. Z. Li, T. Kempa, J. Rybczynski, A. Herczynski, and Z. F. Ren, *Appl. Phys. Lett.* **85**, 2607 (2004).
- [102] S.-K. Joung, T. Okazaki, S. Okada, and S. Iijima, *Phys. Chem. Chem. Phys.* **12**, 8118 (2010).
- [103] M. Cardona, in *Light Scattering in Solids II, Topics in Applied Physics*, edited by M. Cardona and G. Güntherodt Springer, Berlin (1982).

- [104] J. Maultzsch, H. Telg, S. Reich, and C. Thomsen, *Phys Rev. B* **72**, 205438 (2005).
- [105] H. Telg, J. Maultzsch, S. Reich, F. Hennrich, and C. Thomsen, *Phys Rev. Lett.* **93**, 177401 (2004).
- [106] H. Kataura, Y. Kumazawa, Y. Maniwa, I. Umez, S. Suzuki, Y. Ohtsuka, and Y. Achiba, *Synthetic Metals* **103**, 2555 (1999).
- [107] V. Popov, L. Henrad, and P. Lambin, *Phys Rev. B* **72**, 035436 (2005).
- [108] M. Dahanv, S. Levi, C. Luccardini, P. Rostaing, B. Riveau, and A. Triller, *Science* **302**, 442 (2003).
- [109] W. Chan and S. Nie, *Science* **281**, 2016 (1998).
- [110] J. Zhao, J. Zhang, C. Jiang, J. Bohnenberger, T. Basché, and A. Mews, *J. Appl. Phys.* **96**, 3206 (2004).
- [111] S. Coe, W.-K. Woo, M. Bawendi, and V. Bulovic, *Nature* **420**, 800 (2002).
- [112] A. Mews and J. Zhao, *Nature Photonics* **1**, 683 (2007).
- [113] Anonymous, A quantum leap for lighting, *The Economist* **394**, 18 (2010).
- [114] C. Wang, B. L. Wehrenberg, C. Y. Woo, and P. Guyot-Sionnest, *J. Phys. Chem. B* **108**, 9027 (2004).
- [115] R. D. Schaller, M. A. Petruska, and V. I. Klimov, *J. Phys. Chem. B* **107**, 13765 (2003).
- [116] R. D. Schaller and V. I. Klimov, *Phys. Rev. Lett.* **92**, 186601 (2004).
- [117] S. Nie, Y. Xing, K. G.J, and J. Simons, *Annu. Rev. Biomed. Eng.* **9**, 257 (2007).
- [118] F. Garcia-Santamaria, S. Brovelli, R. Viswanatha, J. Hollingsworth, H. Htoon, S. Crooker, and V. Klimov, *NanoLetters* **11**, 687 (2011).
- [119] B. Mahler, P. Spinicelli, S. Buil, X. Quelin, J.-P. Hermier, and B. Dubertret, *Nature* **7**, 659 (2008).
- [120] A. Smith, A. Mohs, and S. Nie, *Nature Nanotechnology* **4**, 56 (2009).
- [121] S. Tavenner-Kruger, Y. Park, M. Lonergan, U. Woggon, , and H. Wang, *Nano Lett.* **6**, 2154 (2006).

BIBLIOGRAPHY

- [122] X. Peng, M. C. Schlamp, A. V. Kadavanich, and A. P. Alivisatos, *J. Am. Chem. Soc.* **119**, 7019 (1997).
- [123] J. J. Li, Y. A. Wang, W. Guo, J. C. Keay, T. D. Mishima, M. B. Johnson, and X. Peng, *J. Am. Chem. Soc.* **125**, 12567 (2003).
- [124] B. O. Dabbousi, J. Rodriguez-Viejo, F. V. Mikulec, J. R. Heine, H. Mattoussi, R. Ober, K. F. Jensen, and M. G. Bawendi, *J. Phys. Chem. B* **101**, 9463 (1997).
- [125] M. A. Hines and P. Guyot-Sionnest, *J. Phys. Chem.* **100**, 468 (1996).
- [126] P. Reiss, J. Bleuse, and A. Pron, *Nano Lett.* **2**, 781 (2002).
- [127] L. Qu and X. Peng, *J. Am. Chem. Soc.* **124**, 2049 (2002).
- [128] L. Brus, *J. Phys. Chem.* **90**, 2555 (1986).
- [129] T. Kippeny, L. Swafford, and S. Rosenthal, *J. Chem. Ed.* **79**, 1094 (2002).
- [130] H. Richter, Z. P. Wang, and L. Ley, *Solid State Commun.* **39**, 625 (1981).
- [131] X. Peng, L. Manna, W. Yang, J. Wickham, E. Scher, A. Kadavanich, and A. Alivisatos, *Nature* **404**, 59, (2000).
- [132] L. Manna, E. Scher, and A. Alivisatos, *J. Am. Chem. Soc.* **122**, 12700, (2000).
- [133] S. Kumar and T. Nann, *Small* **2**, 316, (2006).
- [134] C. Murray, D. Norris, and M. Bawendi, *J. Am. Chem. Soc.* **115**, 8706 (1993).
- [135] T. Vossmeier, L. Katsikas, M. Gienig, I. G. Popovic, K. Diesner, A. Chemseddine, A. Eychmiiller, and H. Weller, *J. Phys. Chem. C* **98**, 7665 (1994).
- [136] H. Reiss, *J. Chem. Phys.* **19**, 482 (1951).
- [137] J. Jasieniak, C. Bullen, J. van Embden, and P. Mulvaney, *J. Phys. Chem. B* **109**, 20665 (2005).
- [138] C. Y. Yeh, Z. W. Lu, S. Froyen, and A. Zunger, *Phys. Rev. B* **46**, 10086 (1992).
- [139] A. M. Smith, A. M. Mohs, and S. Nie, *Nature Nanotech* **4**, 56 (2009).
- [140] D. V. Talapin, I. Mekis, S. Gotzinger, A. Kornowski, O. Benson, and H. Weller, *J. Phys. Chem. B* **108**, 18826 (2004).
- [141] K. Lambert, Ph.D. thesis, University Ghent (2011).

- [142] R. K. Capek, I. Moreels, K. Lambert, D. D. Muynck, Q. Zhao, A. Vantomme, F. Vanhaecke, and Z. Hens, *J. Phys. Chem. C* **114**, 6371 (2010).
- [143] J. J. Li, Y. A. Wang, W. Z. Guo, J. C. Keay, T. D. Mishima, M. B. Johnson, and X. G. Peng, *J. Am. Chem. Soc.* **125**, 12567 (2003).
- [144] J. van Embden, J. Jasieniak, and P. Mulvaney, *J. Am. Chem. Soc.* **131**, 14299 (2009).
- [145] R. G. Xie, U. Kolb, J. X. Li, T. Basche, and A. Mews, *J. Am. Chem. Soc.* **127**, 7480 (2005).
- [146] Y.-J. Lee, T.-G. Kim, and Y.-M. Sung, *Nanotechnology* **17**, 3539 (2006).
- [147] M. Balkanski, R. Beserman, and J. Besson, *Proc. Int. Conf. Lum., Budapest Hungary* (1966).
- [148] F. Comas, N. Studarta, and G. E. Marquesa, *Solid State Commun.* **130**, 477 (2004).
- [149] H. Lange, M. Artemyev, U. Woggon, and C. Thomsen, *Nanotechnology* **20**, 045705 (2009).
- [150] P. Yu, *Solid State Commun.* **19**, 1087, (1976).
- [151] V. M. Dzhagan, I. Lokteva, M. Y. Valakh, O. E. Raevska, J. Kolny-Olesiak, and D. R. T. Zahn, *J. Appl. Phys.* **106**, 084318 (2009).
- [152] H. Lange, Ph.D. thesis, Technische Universitaet Berlin (2009).
- [153] S. Ves, U. Schwarz, N. Christensen, K. Syassen, and M. Cardona, *Phys. Rev. B* **42**, 9113 (1990).
- [154] E. Grueneisen, *Ann. d. Physik* **39** (1912).
- [155] A. P. Alivisatos, T. D. Harris, L. E. Brus, and A. Jayaraman, *Phase Transitions* **89**, 5979 (1988).
- [156] G. Scamarcio, M. Lugara, and D. Manno, **45**, 13792 (1992).
- [157] J. H. Wasilik and F. S. Hickernell, *Applied Phvsics letters.* **24**, 153 (1974).
- [158] M. Sadd, *Elasticity - Theory, Applications, and Numerics* (Elsevier Butterworth-Heinemann, 2005).
- [159] A. Saada, *Elasticity - Theory and Applications* (Pergamon Press Inc., 1974).

BIBLIOGRAPHY

- [160] O. Stier, M. Grundmann, and D. Bimberg, *Phys. Rev. B* **59**, 5688 (1999).
- [161] S.-H. Wei and A. Zunger, *Phys. Rev. B* **60**, 5404 (1999).
- [162] A. Schliwa, private communication (2011).
- [163] K.-Y. Lee, J.-R. Lim, H. Rho, Y.-J. Choi, K. Choi, and J.-G. Park, *APPLIED PHYSICS LETTERS* **91**, 201901 (2007).
- [164] X. Wang, X. Ren, K. Kahen, M. Hahn, M. Rajeswaran, S. Maccagnano-Zacher, J. Silcox, G. Cragg, A. Efros, and T. Krauss, *Nature* **459**, 686 (2009).
- [165] L. Lu, X.-L. Xu, W.-T. Liang, and H.-F. Lu, *J. Phys. Condens. Matter* **19**, 406221 (2007).
- [166] V. M. Dzhagan, M. Y. Valakh, O. E. Raevska, O. L. Stroyuk, S. Y. Kuchmiy, and D. R. T. Zahn, *Nanotechnology* **20**, 365704 (2009).
- [167] H. Lange, M. Machon, M. Artemyev, U. Woggon, and C. Thomsen, *phys. stat. sol. (RRL)* **1**, 274 (2007).
- [168] B. Tell, T. Damen, and S. Porto, *Physical Review* **144**, 771 (1966).
- [169] H. Fan, X. Fan, Z. Ni, Z. Shen, Y. Feng, and B. Zou, *J. Phys. Chem. C* **112**, 1865 (2008).
- [170] R. Rossetti, S. Nakahara, and L. Brus, *J. Chem. Phys.* **79**, 1086 (1983).
- [171] R. Beserman, *Solid State Communication* **23**, 323 (1977).
- [172] A. Alivisatos, T. Harris, P. Carrol, M. Steigerwald, and L. Brus, *J. Chem. Phys.* **90**, 3463 (1989).
- [173] H. Frohlich, *Adv. Phys.* **3**, 325 (1954).
- [174] M. Klein, F. Hache, D. Richard, and C. Flytzanis, *Phys. Rev. B* **42**, 11123 (1990).
- [175] R. Merlin, G. Guentherodt, R. H. and M. Cardona, R. Suryanarayanan, and F. Holtzbergh, *Phys. Rev. B* **17**, 4951 (1978).
- [176] S. Nomura and T. Kobayashi, *Phys. Rev. B* **45**, 1305 (1992).
- [177] H. Lange, M. Artemyev, U. Woggon, T. Niermann, and C. Thomsen, *Phys. Rev.* **77**, 193303 (2008).
- [178] A. M. Kelley, *J. Phys. Chem. Lett.* **1**, 1296 (2010).

- [179] H. Lange, M. Mohr, M. Artemyev, U. Woggon, T. Niermann, and C. Thomsen, *Phys Status solidi A* pp. 1–10 (2010).
- [180] B. Dabbousi, J. Rodriguez-Viejo, F. Mikulec, J. Heine, H. Mattoussi, R. Ober, K. Jensen, and M. Bawendi, *J. Phys. Chem. B* **101**, 9463 (1997).
- [181] A. Pandey and P. Guyot-Sion, *Science* **322**, 929 (2008).
- [182] A. Baranov, Y. Rakovich, J. Donegan, T. Perova, R. Moorge, D. Talapin, A. Rogach, Y. Masumoto, and I. Nabiev, *Phys. Rev. B* **68** (2003).
- [183] A. M. Yaremko, V. O. Yukhymchuk, V. M. Dzhagan, M. Y. Valakh, Y. M. Azhniuk, J. Baran, H. Ratajczak, and M. Drozd, *Semiconductor Physics, Quantum Electronics & Optoelectronics* **10**, 1 (2007).

Acknowledgments

This work would not have been possible without the help of others. Especially, I want to thank

Christian Thomsen, who gave me the opportunity to work in his group, for his general support and continuous guidance.

Alexander Mews for reviewing this thesis.

Prof. Michael Lehmann for being the chairman of my defense.

Prof. Zeger Hens and Dr. Karel Lambert for providing the nanocrystals and for the always entertaining phonecalls.

Dr. Holger Lange, whose consistent eagerness has always motivated me and for being my sparringpartner. Actually, our roles have changed for several weeks now, probably a turn of the tides. Congratulation :)

Dr. Matthias Schenderlein, who showed me how to treat biological tissue and whose sense of humor always delighted my day.

Dr. Dirk Heinrich for the ongoing fun we had supervising the F12 project of the Fortgeschrittenenpraktikum.

all othe members of the Thomsen and Hoffmann groups for the really great working atmosphere.

Dr. Ioanna "Nina" Mantouvalou for proofreading and her enduring persistence in being my fellow back in those years we both were students.

all former and present members of the Smashing Peaches. We are really a quite nerdy bunch, but i learnt a lot within the last four years. I truely hope we will stay in touch and continue our quiz tradition in the upcoming years.

Jana Eisenblätter for her love and proofreading.

my mother.

